Superplastic-like forming of lightweight alloys
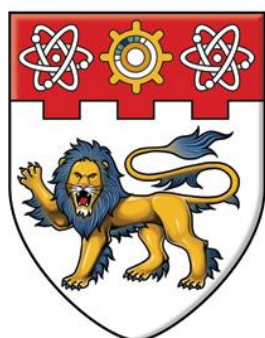
Liu, Jun

2013

https://hdl.handle.net/10356/53503

https://doi.org/10.32657/10356/53503

SUPERPLASTIC-LIKE FORMING OF LIGHTWEIGHT ALLOYS

LIU JUN

SCHOOL OF MECHANICAL AND AEROSPACE ENGINEERING

2013

Superplastic-Like Forming of Lightweight Alloys

Liu Jun

School of Mechanical and Aerospace Engineering

A thesis submitted to the Nanyang Technological University
in partial fulfillment of the requirement for the degree of
Doctor of Philosophy

2013

ABSTRACT

Conventional superplastic forming (SPF) is attractive for the current industrial fabrication of precision, large and complex-shaped sheet-metal components. This process requires a fine-grained material and is carried out at high temperatures (typically above 500 ℃ for aluminum alloys and 900 ℃ for titanium alloys) and slow forming rates (mostly strain rate slower than 10^{-3} s^{-1}).

To address these limitations, an advanced sheet-forming process has been designed by combining hot drawing and superplastic forming (namely gas forming) in a one-step operation to establish a fast forming technology. The process together with a non-isothermal heating system is referred to as superplastic-like forming. The aim of this work is to investigate (i) the relationship between process parameters, material draw-in and thickness distribution and (ii) the microstructural evolution, deformation mechanism and post-forming properties during forming. Target materials are commercial grade AA5083 and Ti-6Al-4V alloys.

Tensile tests were performed for both materials to determine the optimal deformation conditions, i.e. temperature and strain rate. The flow stress data of AA5083 were used in the calibration of a material model for finite element modeling (FEM). The results showed that AA5083 can deform with reasonable flow stress and tensile elongation at 400 ℃ and a strain rate of 2×10^{-3} s^{-1} and that Ti-6Al-4V alloy possesses good forming capability at 800 ℃ and a strain rate of 10^{-3} s^{-1}.

A rectangular die cavity with multiple steps was used to demonstrate different amounts of material draw-in and surface expansion of the formed part in superplastic-like forming. The punch geometry was designed and validated through a parametric study during hot drawing. The measured drawing limits were used to determine the sheet

ABSTRACT

size for hot drawing. The optimal dimensions of AA5083 and Ti-6Al-4V sheets are 200×200 and 210×210 mm^2, respectively.

The non-isothermal heating system is expected to maintain the sheet at a lower global (furnace) temperature. Meanwhile, a higher local temperature in specific zones, i.e. die radii, ensures that the material there has more ductility to flow. For AA5083, the entire forming was conducted at a global temperature of 400 ℃, but the material close to the die radii was selectively heated to 420 ℃. During superplastic-like forming of Ti-6Al-4V alloy, the global and local temperatures were 800 and 820 ℃, respectively.

After completion of forming AA5083 in 8 min, a final part with maximum percentage thinning of 40% at the outward corners and 137% surface expansion was achieved. The forming of Ti-6Al-4V alloy was completed in 16 min, exhibiting a maximum percentage thinning of 54% at the outward corners and the surface expansion of 130%. Stress gradients and the corresponding strain rate differences at the outward corners in the forming sheet led to thinning gradient and plastic straining as a result of geometric inhomogeneity as demonstrated through finite element simulations of hot drawing and gas forming. Cracks and oxidation on the Ti-6Al-4V sheet surface are the other reasons accounting for the thickness reduction at the outward corners.

Fairly uniform microstructure was achieved with the process. The main deformation mechanisms for AA5083 during hot drawing are subgrain boundary migration and subgrain rotation, and they change into subgrain boundary migration and grain growth during gas forming. The hot-drawing phase involves purely dislocation-based deformation, while the gas-forming phase involves dislocation creep with hardening and recovery contributions. A physical model based on the concept of dislocation density is constructed to describe the deformation behavior of AA5083. Simulations of the superplastic-like forming are promising and match the experimental measurements with reasonable agreement, illustrating that critical attention should be paid to the die radii during the process and die design.

ACKNOWLEDGMENTS

CONTENTS

LIST OF FIGURES

LIST OF TABLES

LIST OF TABLES

XVIII

LIST OF SYMBOLS

A	Cross-sectional area of a tensile specimen
b	Burger's vector
c_j	Concentration of jogs
c_V	Vacancy concentration
c_V^{eq}	Equilibrium vacancy concentration
c_γ	Parameter related to recovery by dislocation climb
d, g	Grain size
d_0	Punch diameter for deep drawing
D_0	Blank diameter for deep drawing
D_i	Diffusivity (*eff* = effective diffusion, *gb* = grain boundary, *IPB* = interphase boundary, *L* = lattice, *P* = pipe diffusion, *V* = self-diffusion, *Vm* = vacancy diffusion)
e	Engineering strain
E	Young's modulus
Δf_0	Active energy to overcome lattice resistance
G	Shear modulus
h	Die cavity depth
H_V	Vickers hardness
k	Boltzmann's constant
$K, K_1 - K_8$	Material constants
K_c	Short-range parameter related to dislocation sub-cell diameter
L	Gauge length of a tensile specimen
L_D	Material draw-in length
m	Taylor orientation factor
m value	Strain rate sensitivity index
n	Strain hardening exponent
p	Grain growth exponent
P	Tensile force
p, q	Calibration parameters for modeling
Q_{fj}	Formation energy of thermal jogs

LIST OF SYMBOLS

Q_v	Activation energy for self-diffusion
Q_{vf}	Activation energy for forming a vacancy
Q_{vm}	Energy barrier for vacancy migration
s	Engineering stress
ΔS_{vf}	Change in entropy for vacancy creation
t	Measured sheet thickness
t_0	Initial sheet thickness
T	Absolute temperature
T_m	Melting temperature
W_o	Initial sheet width
W_f	Minimum required sheet flange width
α	Proportionality factor
β_{max}	Limiting drawing ratio
γ_{SFE}	Stacking fault energy
ε	True strain
$\dot{\varepsilon}$	Strain rate
$\dot{\varepsilon}^p$	Plastic strain rate
$\dot{\bar{\varepsilon}}_{ref}$	Reference strain rate
ρ_{eq}	Equilibrium density of dislocation
ρ_{i0}	Initial immobile dislocation density
ρ_i	Immobile dislocation density
σ	True tress
σ_G	Athermal stress
σ_0	Yield strength for a single crystal
σ^*	Friction stress
σ_y	Yield stress (flow stress)
τ_0	Athermal strength
χ	Friction of mechanical work for vacancy generation
ς	Neutralization effect by vacancy emitting and absorbing jogs
Λ	Mean free path
ν	Poisson's ratio
Ω_0	Atomic volume
Ω	Parameter related to recovery by dislocation glide and annihilation

LIST OF ABBREVIATIONS

AA5083	Aluminum alloy 5083
BCC	Body-centered cubic
CCD	Charge coupled device
CHS	Crosshead speed
DRX	Dynamic recrystallization
EBSD	Electron backscatter diffraction
ECAP	Equal channel angular pressing
FAST	Ford advanced superplastic-forming technology
FCC	Face-centered cubic
FEM	Finite element modeling
FE-SEM	Field emission-scanning electron microscope
FSP	Friction stir processing
GBS	Grain boundary sliding
GF	Gas forming
HAGB	High angle grain boundary
HD	Hot drawing
IPF	Inverse pole figure
LAGB	Low angle grain boundary
LDR	Limiting drawing ratio
ND	Normal direction
ODF	Orientation distribution function
OIM	Orientation imaging microscopy

LIST OF ABBREVIATIONS

PD	Plane direction
RT	Room temperature
SD	Solute drag
SEM	Scanning electron microscope
SPF	Superplastic forming
SPF/DB	Superplastic forming combined with diffusion bonding
TD	Transverse direction
TMP	Thermo-mechanical processing
UTS	Ultimate tensile strength/stress
XRD	X-ray diffraction
YS	Yield strength/stress
YTZ	Yttria-stabilized tetragonal zirconia

CHAPTER 1   INTRODUCTION

1.1   BACKGROUND

Conventional superplastic forming (SPF) is a process by which a sheet metal is formed at elevated temperature by using gas pressure introduced into a single-side die cavity. The benefits of superplastic forming are its high formability, complex (and intricate) shape possibilities, lower tooling cost, labor and material saving through elimination of parts, joining and secondary machining [1-10]. The disadvantages are mainly the slow forming rates, poor thickness control and expensive base material.

Superplastic materials largely comply with the SPF requirements, which include specific range of forming temperatures (typically above $0.5T_m$, where T_m is the melting temperature in Kelvins) and high microstructure stability during deformation. Aluminum alloy 5083 (AA5083) [11] and Ti-6Al-4V [12] alloys possessing fine grains and stable structures can exhibit remarkable superplasticity suitable for SPF at strain rates lower than 10^{-3} s^{-1} and temperature above 500 ℃ and 900 ℃, respectively.

The slow forming rates and high forming temperatures lead to many problems, such as reduced tool life and high heating demands. In particular, mechanical properties of the formed products are poor due to the microstructural defects and large amounts of cavitation induced [13-17]. Moreover, the high-temperature requirement limits the application in forming of the alloys that are sensitive to oxidation, especially for titanium alloys at elevated temperature.

This research seeks to increase forming rate and reduce forming temperature through alternative processing and better process control in order to accelerate productivity and make the cost-effective technology viable by producing lightweight components with better mechanical properties.

Deep drawing is a fast forming process that competes with SPF. During hot drawing, the penalizing factors are mainly due to the friction and springback effects. Multiple drawing phases are also often required to achieve the final shape. Those effects can be reduced or avoided using superplastic techniques. However, thickness variation has been found to be more prominent for superplastic (non-contact) processes compared to hot drawing [18]. The thinning of the sheet material is also more important during SPF.

In order to take the advantages of both techniques, a hybrid method which combines hot drawing and superplastic forming (namely gas forming) is proposed. The hybrid forming process together with a non-isothermal heating system is defined as superplastic-like forming.

The novelty of this research in development of the superplastic-like forming process is outlined as follows:

It is anticipated that by performing a drawing step before gas forming, the combined process will be faster. There will be less thinning as sheet material is drawn inside the mould before the gas forming step and the springback effect will be reduced compared to conventional deep drawing.

The variation of the temperature at different sheet locations through selective heating will help to improve material formability. This can also increase forming speed with

the aid of deep drawing. Therefore, with a reduced process temperature, the problems

mentioned earlier linked to oxidation or microstructural defects will be limited.

Moreover, lower cost materials or non-superplastic materials can be used with this

process. The deformation behavior of AA5083 and Ti-6Al-4V during superplastic-like

forming differs from that of conventional superplastic materials during SPF [19].

Based on the deformation mechanisms, finite element modeling (FEM) is performed to

account for the plastic flow of AA5083 in multi-scale computations.

1.2 OBJECTIVE

The main objective of this research is to design a hybrid forming process that

combines hot drawing and blow forming together with a non-isothermal heating

system to improve the strain rate and thickness control during the sheet forming of

aluminum and titanium alloys. Finite element modeling will provide a fundamental

scientific understanding of the deformation behavior in a physical-based modeling

framework.

The scope of the research consists of five parts as follows:

    (1) To investigate the deformation behavior of the non-superplastic grade

        AA5083 during high-temperature tensile testing. The sensitivity of

        formability as a function of temperature and strain rate is used to determine

        the optimal deformation conditions. Experimental data in the form of stress

        – strain curves are used to calibrate a physical-based material model for

        finite element simulations.

(2) To install the equipment for superplastic-like forming and investigate the forming capability of the hybrid process. Gas pressure cycle is predicted based on the material model to maintain the blow forming at a target strain rate. Experimental data, i.e. process parameters, material draw-in, bulge height and sheet thinning, are measured to evaluate the formed part.

(3) To characterize the evolution of microstructure and texture during superplastic-like forming through electron backscatter diffraction (EBSD). The deformation mechanisms of AA5083 and Ti-6Al-4V during superplastic-like forming are investigated based on the EBSD results.

(4) To implement the dislocation density model into finite element simulations to model the macroscopic forming process. The simulation results are used to analyze the sheet thinning characteristics.

(5) To expand the advantages of the hybrid process to the forming of Ti-6Al-4V alloy sheets at the lowest temperature. The microstructure evolution and oxidation behavior are also examined to evaluate its post-forming properties.

CHAPTER 2   LITERATURE REVIEW

2.1   MATERIAL CHARACTERISTICS

2.1.1   Introduction

In recent decades, aluminum alloys have attracted attentions of many researchers, engineers and designers as promising structural materials for automotive industry or aerospace applications. The aluminum alloys of (non-)heat-treatable with high strength are commonly used materials, such as 2024, 5083, 6061, 7055, 7075 and 7475 [20-29]. As a commercial alloy with excellent corrosion resistance and high strength, AA5083 is suitable for the structural sheet-metal fabrication [11, 14, 30, 31].

Titanium alloys are good candidates that maintain the distinguish characteristics, such as high temperature capabilities, high strength-to-weight ratios and good superplastic behavior [32]. Ti-6Al-4V is a well-known lightweight alloy for its potential as a superplastic material for applications in different areas, including aerospace, chemical, transportation and biomedical fields [33-40].

2.1.2   Aluminum Alloys

2.1.2.1   Characteristics of aluminum alloys with superplasticity

(a) Superplasticity

Superplastic materials are polycrystalline solids which have the capability to undergo

large plastic strains, often in excess of 200% prior to failure [41]. AA5083 with superplasticity is usually attained in the temperature range from 500ºC to 565ºC and the strain rate range $< 10^{-3}$ s^{-1} [11].

Figure 2-1 shows photographs of AA5083 specimens tensile tested at different crosshead speeds (CHSs) at 525ºC. The tensile elongation-to-failure increased with decreasing test speed (strain rate), which demonstrates the strain rate sensitivity of this alloy. The grain growth rate [11] and the amount of cavitation [14] increase with decreasing strain rate. The influence of microstructure on cavitation development has been investigated by Chang *et al* [15] extensively.

Untested   % Elongation

223%

CHS = 8 mm/min

364%

CHS = 0.5 mm/min

Figure 2-1 Tensile elongation of AA5083 tested at different crosshead speeds at 525 ºC [11].

(b) Strain rate sensitivity

Strain rate sensitivity represents the capacity of the materials to resist necking and influences the overall deformation and stability during superplastic flow [41]. To

capture the deformation characteristics of a superplastic material, it is essential to determine the strain rate sensitivity index (*m* value). Strain rate sensitivity varies with strain rate, strain and temperature. Tensile elongation increases with the decrease in strain rate, and the highest *m* values are situated at the middle strain rate range [42]. Moreover, the superplastic materials are the high sensitivity of flow stress to deformation rate. The *m* value should be greater than or equal to 0.3, while mostly lies between 0.4 − 0.8 [43-46].

(c) Flow stress

The flow stress of a superplastic material is a sensitive function of strain rate, temperature and grain size [19]. The flow stress as a function of the strain rate is represented in Figure 2-2. The deformation behavior of superplastic materials is quite different from that of the conventional materials. It appears that the logarithmic stress − strain rate curve shows a typical sigmoidal profile. The flow stress increases with increasing strain rate. The slop of the curve is the strain rate sensitivity index of the material defined as

$$m = (d \, \log \sigma)/(d \, \log \dot{\varepsilon}) \qquad\qquad \text{Eq. (2-1)}$$

It can be divided into three regions, i.e. Region I, II and III. Region I and III represent the deformation at low strain rates ($< 10^{-3}$ s^{-1}) and high strain rates ($> 10^{-2}$ s^{-1}), respectively. Here the corresponding *m* values are low ($m < 0.3$) indicating the non-superplastic regions. Region II is the region where the materials can achieve superplasticity when loading is carried out within the specific strain rate region. The *m* values are high ($m > 0.3$) and the mechanism that dominates deformation is well known as grain boundary sliding (GBS) [19].
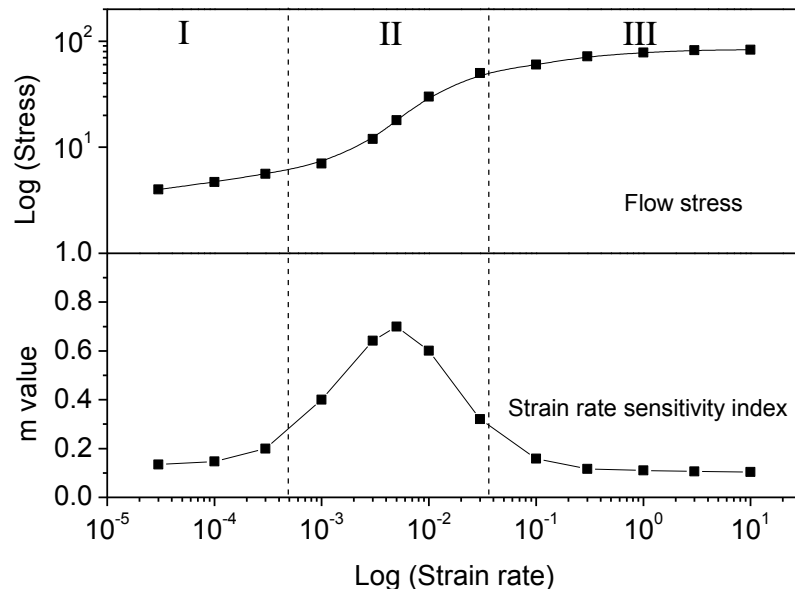
Figure 2-2 Strain rate dependence of flow stress and strain rate sensitivity index (*m* value) [19].

(c) Deformation mechanisms

Creep is a time-dependent plastic deformation process that occurs in materials at a temperature $T > (0.3 - 0.5)T_m$ [42]. The high-temperature plasticity for a metal is ascribable to various deformation mechanisms [15, 47-50], i.e. dislocation glide, dislocation creep and diffusional flow. Conventional superplastic materials usually exhibits superplasticity based on grain boundary sliding with diffusional accommodation [51]. In this case, grains can remain equiaxed throughout the superplastic deformation [50].

Figure 2-3 shows a deformation mechanism map for aluminum at 400ºC represented by grain size versus σ/E, where E is the Young's modulus of pure aluminum. This map shows that the deformation of grain boundary sliding (D_{gb}) is situated at low σ/E and grain size values, with strain rates ranging from 10^{-5} to 10^{-3} s^{-1}.

The figure shows a deformation mechanism map with axes Grain size (μm) on the vertical (from 10^{-1} to 10^4) and Normalized stress σ/E on the horizontal (from 10^{-6} to 10^{-1}). Regions labeled: Harper-Dorn creep; Dislocation glide, D_L; Dislocation climb-plus-glide, D_L; Dislocation glide; Diffusional flow; Dislocation climb-plus-clide, D_{gb}; Power-law breakdown.
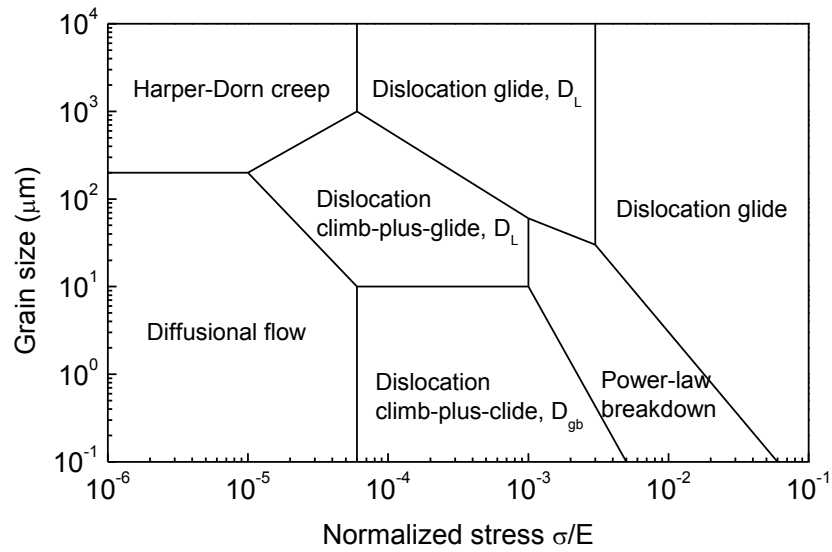
Figure 2-3 Deformation mechanism map for aluminum at 400 °C after Frost and Ashby [52].

2.1.2.2   Mechanical processing of aluminum alloys for superplasticity

Microstructures suitable for superplastic flow of AA5083 can be obtained through various thermo-mechanical processing (TMP) methods. Rolling, forging, extrusion, equal channel angular pressing (ECAP) and friction stir processing (FSP) have been used to produce fine-grained structures and the observation of superplasticity [53-58].

(a) Superplastic behavior processed by rolling

Cold rolling process with different reduction ratios and heat treatments are able to obtain homogeneous, equiaxed and fine-grained microstructures that meet the requirements of superplastic deformation [56, 59]. Hot rolling process is also used to produce excellent ductility for aluminum sheets [30]. Significant differences in grain size and the extent of superplasticity were observed between the hot-rolled and the

cold-rolled alloys, with tensile elongations exceeding 600% for the cold-rolled alloy as compared to 160% for the hot-rolled [11, 30]. The fine-grained structure has been found to benefit the superplastic elongation [11].

(b) Superplastic behavior processed by ECAP

Equal channel angular pressing (ECAP) is another powerful method based on a heavy strain mechanism of recrystallizing the material into a fine-grained structure [60]. The best superplasticity obtained after ECAP was 350% [61], which was not superior to the commercially available rolling-type AA5083 [11]. Grain refinement of AA5083 by ECAP has been reported to reduce the grain size from 200 to 0.2 μm [62]. Sub-micron-grained structure is also beneficial to low-temperature superplastic behavior of AA5083. The largest elongation of 315% was achieved from the as-ECAP samples tested at 275ºC and 5×10^{-4} s^{-1} [58].

(c) Superplastic behavior processed by other techniques

Friction stir processing (FSP) has been used to produce fine and equiaxed grains [63]. For the FSPed material, the tensile elongations are all above 300% at the test temperatures ranging from 490 to 530ºC. For the material without FSP, all the corresponding tensile elongations are below 200% [26, 64, 65].

Severe plastic deformation has been used to develop nano-crystalline structures for aluminum alloys [66, 67]. The Al-Mg alloy reported by Avtokratova *et al* [68] exhibits excellent superplastic behavior with elongations from 3000 to 4100% in temperature range of 400 to 475ºC and at strain rates of 10^{-2} to 10^{-1} s^{-1}.

2.1.3 Titanium Alloys

2.1.3.1 Characteristics of titanium alloys with superplasticity

Many research papers have reported the superplastic characteristics of titanium alloys. Superplasticity in titanium alloys was attained by using various TMP methods as well as used for aluminum alloys, as summarized in Table 2-1.

Table 2-1 Summary of Ti alloys properties using various processing methods.

Material	Temperature (℃)	Elongation (%)	Strain rate (s^{-1})	Processing method	Reference
Pure Ti	600	243	10^{-3}	Two-step deformation	[69]
Ti-6Al-4V	650	530	10^{-4}	High pressure torsion	[33]
	725	400	10^{-2}		
Ti-6Al-4V	600	> 1000	10^{-3}	$0.3 - 0.5$ μm gains by protium treatment	[70]
	800	> 6000			
	850	> 9000			
Ti-6Al-4V	900	> 500	10^{-3}	TMP	[12]
Ti-6Al-4V	650	568	10^{-3}	$0.1 - 0.2$ μm grains by high pressure torsion	[38]
	725	676			
Ti-6Al-4V	850	523	1.3×10^{-3}	Maximum m value deformation	[40]
	900	642			
Ti-33Al based	850	408	2×10^{-4}	Forging to a total strain of 80%	[36]
	1000	467	2×10^{-4}		
	1075	517	8×10^{-5}		
Ti-47Al based	1075	281.3	4×10^{-5}	Grain size of 95 μm	[71]
	1100	287.5	4×10^{-5}		
Ti-6.4Al based	600	35.6	---	Roll forming	[72]

In developing superplastic material or in making the existing material superplastic, a lot of information and investigations have been reported [5, 73, 74]. Diphasic titanium alloys enable serial superplastic forming from industrial sheets without any special preparation of the structure. Therefore, they are named "naturally" superplastic [74]. By combining superplastic forming and pressure welding of a nano-structured Ti-6Al-4V alloy, it made possible to apply the "low-temperature superplasticity" for fabricating hollow components at 600ºC [35].

2.1.3.2   Mechanical processing of titanium alloys for superplasticity

Superplastic flow of titanium alloys is achieved at high temperatures (typically above 900ºC) and at low strain rates (usually lower than 10^{-3} s^{-1}) [42]. Some alloys can exhibit superplasticity at lower temperatures when they possess ultra-fine-grained (sub-micron- or nano-) microstructures [41]. There are various techniques to refine the grains through the severe plastic deformation, such as high pressure torsion straining, ECAP and multi-directional forging [33, 37, 69, 70, 75].

The enhanced superplasticity in Ti-6Al-4V alloy is associated with formation of the ultrafine-grained structures [33]. This alloy sheet with a sub-micrometer crystalline structure (grain size of 0.3 μm) was produced by forging together with rolling at temperatures below 650ºC [37]. The low-temperature superplasticity was observed in an ultrafine-grained Ti-6Al-4V alloy with a grain size of 0.1 − 0.2 μm produced by high pressure torsion [38]. Protium treatment has attracted a lot of attentions due to its ability to produce the ultrafine-grained structures for titanium alloys [76]. Ti-6Al-4V alloy with a grain size of 0.3 − 0.5 μm obtained through this treatment can exhibit the maximum elongation over 9000% at 850ºC [70].

2.2 SHEET METAL FORMING

2.2.1 Deep Drawing

2.2.1.1 Fundamentals

Deep drawing is the base for the mass production of sheet-metal components. Figure 2-4 illustrates the procedures of deep drawing. It is a process in which a blank or workpiece, usually controlled by a pressure plate, is forced into and/or through a die by means of a punch to form a hollow component.

Deep drawing depends on strain hardening of the material to achieve the required formability and prevent thinning and rupture during forming. It is a fast forming process, during which strain hardening is associated with dislocation cell formation in the classical manner. The strains achievable in deep drawing are limited by the maximum tensile stress which must not exceed the tensile strength of the material. The thickness is substantially the same as that of the original sheet [77].
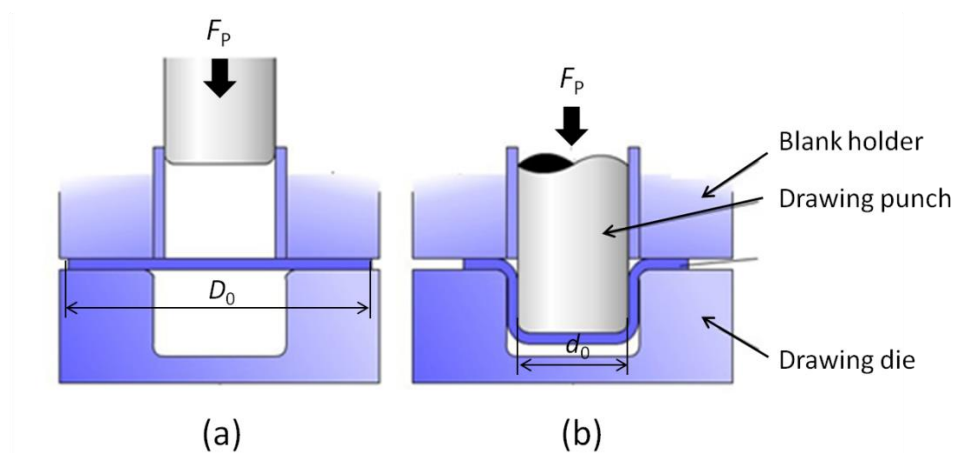
Figure 2-4 Schematic of deep drawing: (a) before drawing and (b) after drawing.

The part can be circular, rectangular or just about any cross-section [78]. Drawing can be either shallow or deep depending on the amount of deformation. Shallow drawing is used to describe the process where the depth of drawing is less than the smallest dimension of the opening; otherwise, it is considered deep drawing [79].

2.2.1.2   Drawability and drawing ratio

The metal used in deep drawing must be malleable as well as resistant to stress and tension (stretching) damage [78]. Success of drawing depends on the ability of material to flow in the flange region ability to resist thinning in the sidewall. This requires low flow strength in the plane of the material in all directions and high flow strength in the through-thickness direction [77, 78].

Drawing ratio is defined as a measurement of determining the stretching drawability of the material in the given sheet thickness and lubrication, as shown in Eq. (2-2).

$$\beta = D_0 / d_0$$ Eq. (2-2)

D_0: Starting diameter of blank sheet

d_0: Punch diameter

The larger the chosen drawing ratio, the larger will be the maximum drawing load under otherwise constant conditions. This load must be transmitted by the wall of the drawn component. Therefore the drawing ratio must not exceed a maximum value, the limiting drawing ratio (LDR) β_{max}, in order to keep materials drawn without tearing to the punch diameter in cup drawing. Approximate values of β_{max} for aluminum and titanium sheets drawn at room temperature are 2.1 and 1.9 [77], respectively.

2.2.1.3   Development of deep drawing

In order to increase production efficiency and obtain a good tool design and manufacturing control, many techniques have been adopted to extensively investigate the function of limiting drawing ratio. Experimental measurements [80] and numerical simulations [81-84] for LDR make it possible to better understand and control the drawing limits of sheet metals in industry.

As an improved drawing process, hydro-mechanical deep drawing has gained increased interest in the sheet metal forming [85]. Recently, a pressurized hydro-mechanical deep drawing process was designed to efficiently deep draw 08Al steel [86]. A friction aided deep drawing process has been newly applied to overcome the defects of localized wrinkling and intensive shear deformation to obtain successful deep cups [87].

A differential temperature technique was demonstrated to be able to increase the LDR during deep drawing of a superplastic Zn-Al alloy from less than 2.4 for isothermal conditions to more than 3.75 for the non-isothermal condition [79]. The deep drawing process equipped with a localized heating and cooling technique has proved to effectively improve the sheet forming of magnesium alloys [88].

For some sheet materials, such as titanium alloys with low ductility at ambient temperature, deep drawing at elevated temperature is an operational way to improve the material ductility and consequently produce a strong drawn component. With this method, the maximum drawing ratios for the warm drawing of Al-Mg alloys can reach up to 3.0 [77].

2.2.2 Superplastic Forming

2.2.2.1 Fundamentals

Superplastic Forming or SPF is a high-temperature process by which sheet metals are deformed by gas pressure in a single-side die chamber to produce parts of complex shape by taking advantage of the superplastic flow behavior of the material. Superplasticity is required during SPF due to grain boundary sliding (GBS) in the specific range of temperature ($> 0.5T_m$), grains (mostly < 10 μm), high microstructure stability with respect to grain growth, and high purity of the structure. Thickness variation has been found to be more prominent for superplastic processes compared to deep drawing.

Figure 2-5 illustrates the schematic diagrams of the SPF process. Initially, a sheet is clamped and sealed on the die. The gas within the lower die chamber is simply vented to atmosphere. Argon gas is normally imposed over the sheet for high pressure forming. Once the sheet is in contact with the corner of the die, the material in this region is locked by friction and further deformation is therefore prevented. The remaining free regions will continue to expand until the part is net-shape formed [41].
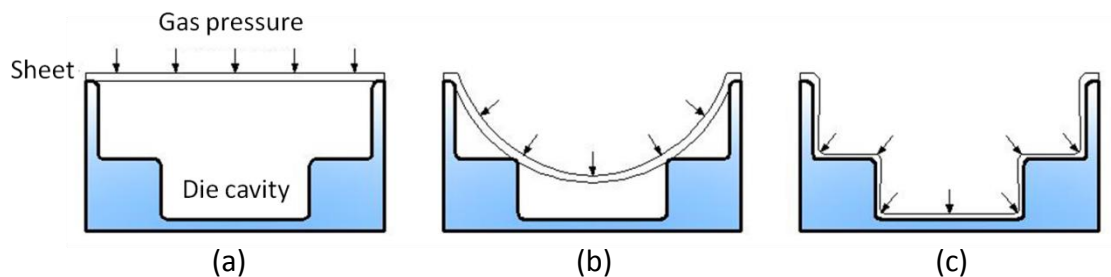
Figure 2-5 Schematic of superplastic forming: (a) clamping and sealing, (b) blow forming and (c) fully formed part [89].

2.2.2.2   Superplastic forming of aluminum alloys

The major drive on SPF has emphasized on the development of superplastic materials rather than improving the process. So far, many research papers have indicated the superplastic properties in aluminum [50, 66, 90-92], titanium [33, 35-38, 40, 93, 94], and magnesium [95-99], duplex stainless steels [7] and ceramics [100-104], which can be introduced for SPF applications.

A variety of materials applied in superplastic forming is summarized in Table 2-2. In order to obtain the best superplasticity during SPF, the load curve is regulated so that the strain rate induced in the material is maintained within the optimum superplastic range (strain rates from 10^{-4} to 10^{-2} s^{-1}) [105].

As commercial alloys with excellent corrosion resistance and moderate to high strength, commercially pure aluminum (AA1100), AA7475 and AA5083 were commonly used materials for superplastic forming. For superplastic AA5083 [106, 107], the SPF are mostly conducted above 500ºC, and the forming process usually last longer than 30 min depending on the parts. Verma *et al* [14] have investigated the characteristics of a fine-grained AA5083 by means of superplastic forming a rectangular pan at 545ºC. A final part with the maximum percentage thinning of 50% was obtained from their studies.

2.2.2.3   Superplastic forming of titanium alloys

Superplastic forming of titanium alloys has been widely utilized in processing aircraft components with good mechanical properties [108], since it is an attractive way to manufacture large and intricate parts in one operation. Practical applications of this

technology can also be combined with a joining operation involving diffusion bonding (SPF/DB) between several sheets of material. SPF/DB is an efficient process used for fabrication of hollow fan blades [8], honeycomb structures [109], bellows expansion joints [73] and large engine components [110].

Table 2-2 Summary of SPF investigations for various materials.

Material	Processing method	SPF time (min)	SPF temperature (℃)	Reference
AA1100	Rolling	37	500	[6]
AA7475	Rolling	46	500	[6]
AA5083	Equiaxed grain size of 6.5 μm	30	545	[14]
AA5083	Grain sizes of 6.6 and 7.8 μm	---	475 − 525	[106]
AA5083	Superplastic grade	16	520	[107]
Al-3%Mg-0.2%Sc	ECAP to grain size of 0.2 μm	1	400	[62]
AZ31	Equiaxed grain size of 6.6 μm	20	400	[98]
AZ61	Rolling to grain size of 9.2 μm	4 − 53	400	[97]
Duplex stainless steel	Superplastic grade	---	950	[7]
Ti-6Al-4V	Superplastic grade	30	927	[73]
Ti-6Al-4V	FSP	50	900 (big grains) 785 (fine grains)	[110]
Ti-6Al-4V	SPF/DB	40	920	[8]
Ti-6Al-4V	SPF/DB	30	930	[109]
YTZ with Al$_2$O$_3$	Ceramic sheet, SPF	125	1475	[100]

A complex hollow structure with net-shape was fabricated from fine-grained sheet by superplastic forming, and the refined structure with a grain size of about 0.4 μm led to

a substantial mechanical properties improvement [39]. In addition, SPF/DB was applied to develop friction stir processing for Ti-6Al-4V alloy in order to allow the joining of multiple pieces to produce much larger components [110].

2.2.2.4   SPF advantages and disadvantages

One of the advantages of SPF is that complex parts such as window frames, vehicle body panels, aircraft doors or piping components can be produced in one single piece without the need of further parts assembly (see Figure 2-6). Compared to conventional technologies, SPF offers cost saving in the range of 20 − 30% [111] as well as weight reduction (~ 40%) and lower part count; these benefits increasing with the complexity of the parts to be made. Moreover, there is no springback effect after SPF and therefore the final shape of the part is identical to the shape of the mould that was used to produce it which simplifies mould design and improves dimensions accuracy.
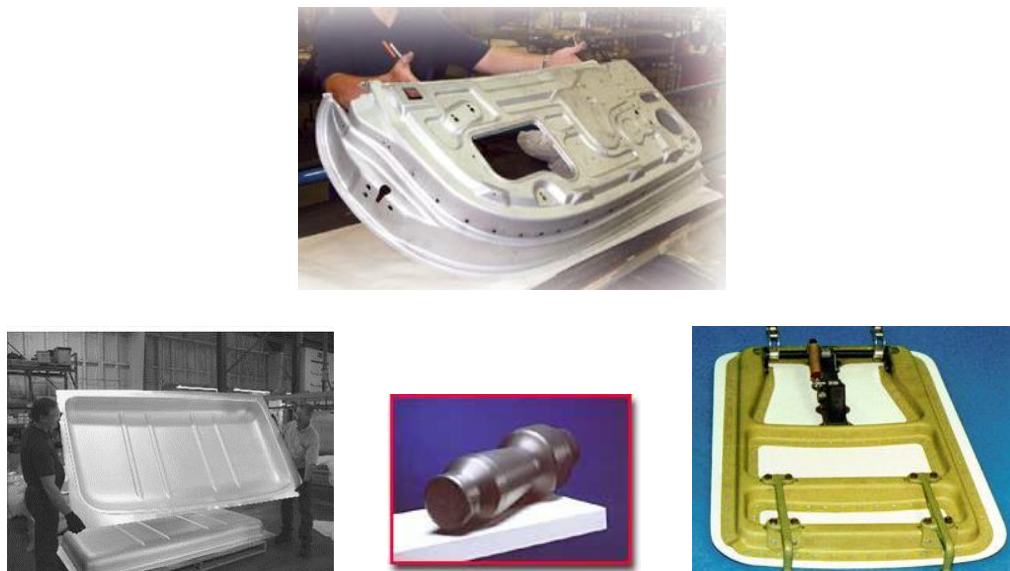
Figure 2-6 Example of parts formed by SPF: car door assembly [112] (top), one piece truck cab roof [10] (left), sensor housing [111] (center), aircraft door assembly [108] (right).

The main drawbacks of SPF are the higher cost of the materials to be used, the speed of the forming process which is relatively low and the high temperature required. Cycle times vary from thirty minutes to two hours depending on the parts in conventional SPF. The limitations for SPF lie within the material and the actual mechanisms for the superplastic behavior. The initial wall thickness of the sheet needs to compensate the maximum thinning that will happen after forming [14].

To fully benefit from the advantages of the superplasticity effect it is necessary to expand the limits of superplastic forming to higher strain rates and to lower temperature. Multi-rate SPF is one way to improve the process by enabling the parts to be formed in a much shorter time [113]. The technique consists in starting with a high strain rate and then progressively updating the strain rate to avoid premature failure using the results of finite element calculations.

2.2.2.5   SPF cost structure

SPF is today a niche activity with high value add [10]. For industrial applications, the superplastic material largely complies with the SPF process conditions, such as fine grain size, high structure stability and high purity of the structure. Superplastic AA5083 products have been implemented on various Boeing commercial airplanes [108]. Superplastic materials are specially prepared to meet the requirements for SPF. However, for some alloys such as AA6xxx series [114], processing is complicated and difficult, and they are not yet suited for commercial application for SPF. Therefore, simplifying the preparation of raw material and minimizing variable cost through alternative materials is critical. Compared to superplastic materials, the lightweight and commercial alloys offer cost saving in the range of $20 - 70\%$ [9].

The technical cost is another burden in the development of sheet forming process [115]. As compared to conventional stamping, SPF of aluminum alloys is a cost-effective method with increase of production volume [9]. However, conventional SPF can require cycle times of 30 min or more, which limits production efficiency and results in more cost penalty. Therefore, an alternative manufacturing process that contributes to economize the production cost is of great importance. A technical cost model [116] proposed by Ford Motor have shown that an one-third reduction of cycle time can significantly reduce the production cost of an aluminum hood up to 40%.

Titanium-based alloys can possess superplasticity as a natural consequence of commercial processing methods. However, most of the prior SPF of titanium alloys has been carried out above 900ºC [8, 93]. This can limit the forming of the alloys that are sensitive to oxidation. It has been reported that the oxidation [117] and the "alpha case" effect [118] would significantly influence the mechanical behavior when titanium alloys are exposed to elevated temperature (especially above 850ºC) in open atmosphere. The oxide film formed during forming is deleterious to material properties, and causes damage easily to the parent material. Applications of protective coating [118] and gas atmosphere [119] on Ti-6Al-4V sheets are possible ways of overcoming oxidation during superplastic deformation. Moreover, the high-temperature process requires high-heating demands and long tooling life. These requirements can consequently complicate the forming process and raise the production cost as well.

2.2.3   Development of Sheet Metal Forming

The first patent application closely related to SPF was filed in 1967 by D.S. Fields for

his work at IBM on the application of thermoforming techniques, such as those utilized for polymers and glass, to metals and in particular to the superplastic Zn-Al eutectoid alloy [120]. During the past years, interest in SPF has been mostly growing, to achieve more than 300 patents filed today. Those patents relate either to the development of the process itself (SPF and SPF/DB) or to the production of materials suitable for SPF. Table 2-3 summarizes the SPF patents that are originating from General Motors, Ford and Boeing Company in the recent decade.

Friction stir processing (FSP) for superplasticity has the potential to expand the domain of superplastic forming to several new enabling concepts, such as selective superplasticity, thick sheet superplasticity and superplastic forging [26, 64]. FSP has been introduced to produce wide sheets of reasonably homogenous materials with high-strain-rate superplasticity, which was suitable for punch forming. A deep cup of AA7075 part with the depth of 52 mm could be produced at a slower strain rate of 10^{-3} s^{-1} at 450ºC [27]. Superplasticity in AA7475 sheet induced by FSP has been applied in the superplastic forming process [121].

For higher production efficiency, General Motors has developed a new technique called quick plastic forming (QPF) which is a variation of SPF with increased forming rates and lower forming temperatures [18, 122]. QPF takes advantage of the solute-drag creep deformation mechanism that dominates grain boundary sliding at fast strain rates and low temperatures in superplastic grade AA5083 [50]. A Ford advanced superplastic-forming technology (FAST) which is based on a suite of new technologies [9] that decrease the overall cycle time and cost of SPF enables sheet forming to be cost-effective for significantly higher-volume applications [123]. Finite element analysis and experimental investigation of high strain rate superplastic forming have

also been reported in Al-Ti [124] and Al-Mg alloys [125].

Table 2-3 Summary of SPF patents in recent decade.

Title	Year	Description	Patent
Quick plastic forming of aluminum alloy sheet metal	2001	A method for fast-stretching Al-Mg alloy sheets	[126]
Apparatus for superplastic forming	2004	An apparatus for massive and rapid SPF production using dies of multi-layer structure	[127]
Method for double action gas pressure forming sheet material	2005	Pre-forming and final shape forming in a single press	[128]
Method for stretch forming sheet metal by pressing and the application of gas pressure	2005	Stretch forming and gas pressurizing in a single press	[129]
High throughput quick-plastic-forming	2006	Forming a sheet metal in multiple forming stages of single-action tooling	[130]
System and process for superplastic forming	2007	A system and method for SPF a workpiece	[131]
Method and apparatus for forming complex contour structural assemblies	2008	A method and associated pre-form for forming a complex	[132]
Sheet metal forming process	2008	A mechanical (double-action draw) forming step and a SPF step	[133]
Multistage superplastic forming apparatus and method	2010	Multistage steps in sequence of mechanical drawing, SPF, second pre-forming and final gas forming	[134]
Method and apparatus for hot forming of sheet metal in titanium-base alloys	2010	A low-temperature forming of titanium-base sheets	[135]
Preform for forming complex contour structural assemblies	2011	A pre-forming step together with a pressurized fluid	[136]

Hybrid forming process can be used to decrease the forming time for mass production, in which it may be either a pre-forming method in the die or a secondary operation such as a restrike operation to form the part [9]. A moving or adjustable die member in conjunction with gas pressure forming process has been reported in the Metals Handbook [137], it was also called a thermo-forming method. The moving punch in this process can assist in pre-stretching the sheet material inside the die cavity before gas pressure is applied. In some cases, the use of a cooled punch was able to increase the formability of drawing process [79].
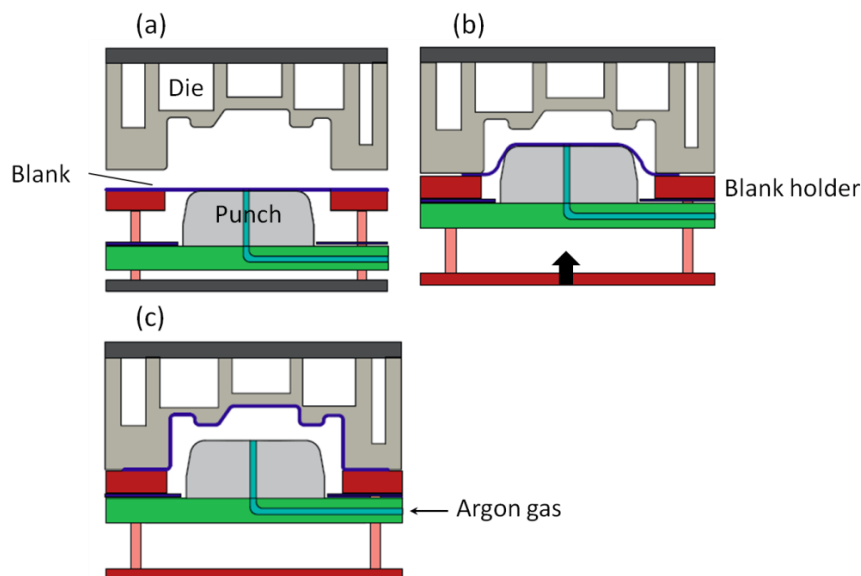
Figure 2-7 Schematic of the hot draw mechanical pre-forming process: (a) loading and sealing, (b) hot drawing and (c) superplastic forming [138].

By adopting a mechanical pre-forming operation into SPF, as shown in Figure 2-7, Luo *et al* [138] have enhanced formability and improved production efficiency for

superplastic grade AA5083 at 475ºC. The pre-forming process reported in their study was useful to draw the materials into the die assembly before SPF. The superplastic forming time were decreased from 20 min to 130 s when combined with the mechanical pre-forming operation.

2.3   MICROSTRUCTUE AND TEXTURE

2.3.1   Microstructure Evolution

During conventional superplastic forming of aluminum sheets, the evolution of microstructure related to strain, strain rate and temperature have been widely investigated in various forming conditions [139-143]. Stress − strain curves obtained in metals can provide clues on the complex internal processes [144] in terms of macro-scale, which were involved during hot deformation. However, the microstructural information in terms of micro-scale during hot deformation is still lacking.

The characterization and measurement of microstructure and texture are of great importance to evaluation of sheet forming because not only does the grain size strongly influence the mechanical properties (macro-scale) at low and high temperatures [145], but it also influences subgrain-boundary motion [146], recrystallization transformation [141], annealing behavior [142] and stress release [147] during deformation.

By using orientation imaging microscopy (OIM) [148], it is possible to collect and analyze large sample populations of individual grains (i.e. microstructure) and orientations (i.e. texture). Figure 2-8 shows the microstructure of an extruded Al-Mg-

Sc alloy superplastic-deformed to different strains. Two typical microstructural features, i.e. subgrain rotation and coalescence (from Figure 2-8(a) to (b)) and dynamic recrystallization (from Figure 2-8(b) to (c)), were obtained by electron backscatter diffraction (EBSD). For aluminum alloys, the changes in (sub-)grain structures can be accompanied only by deformation status and recrystallization due to the absence of phase transformation [147]. Furthermore, recrystallization in aluminum may occur either by dynamic continuous or discontinuous reactions, which can exhibit distinct textures and grain boundary characteristics [141, 142].
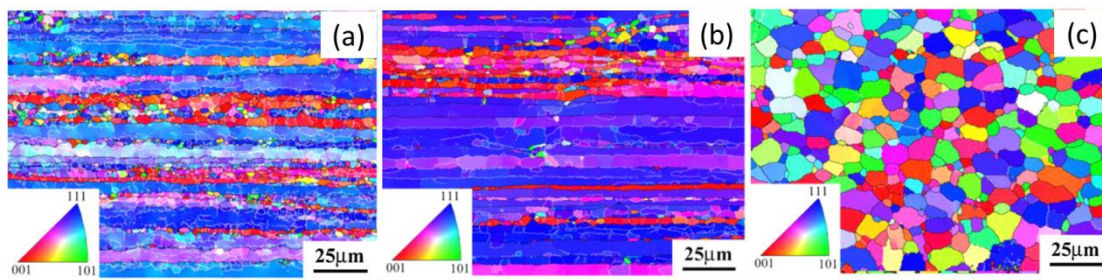
Figure 2-8 Microstructure evolution of Al-Mg-Sc alloy deformed to different strains: (a) as-extruded, (b) 0.6 and (c) 2.1 [146].

2.3.2 Texture Evolution

Regarding texture evolution, aluminum was usually considered as an isotropic material, but the textures developed by various working conditions would produce some directionality in properties. In particular, the textured structures was associated with the earing behavior during deep drawing of aluminum alloys [149]. For the deformed material, the anisotropic properties mainly depend on the texture, i.e.

orientation of grains and subgrains, which is known to be distributed randomly or oriented with some preferred crystallographic orientations during deformation [150].

The deformation textures of face-centered cubic (FCC) metals are determined primarily by the stacking fault energy (γ_{SFE}) [151]. Figure 2-9 shows a continuous tube which is used to describe the fiber texture. For metals with high values of γ_{SFE}, such as aluminum, the β–fiber is prominent in the texture which runs from Brass, {110} <112> at φ_1=35º, Φ=45º, φ_2=90º, through S, {123} <634> at φ_1=59º, Φ=37º, φ_2=63º to Copper, {112} <111> at φ_1=90º, Φ=35º, φ_2=45º. The α–fiber can also be described in Figure 2-9, where it extends from Goss, {110} <001> at φ_1=0º, Φ=45º, φ_2=90º to Brass component [152].
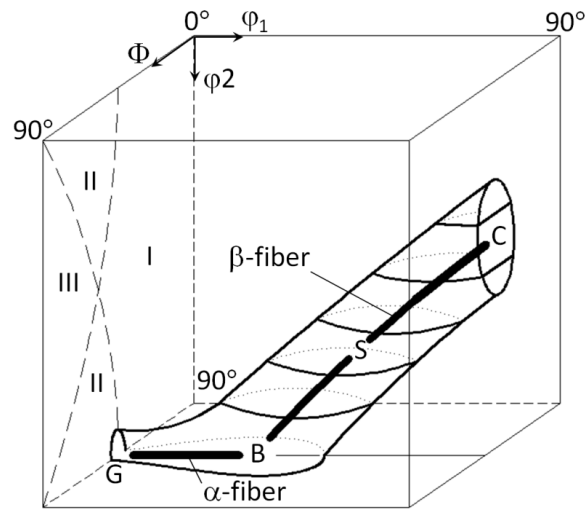
Figure 2-9 Schematic representation of the FCC rolling texture in the first subspace of three dimensional Euler angle space [152].

2.4   FINITE ELEMENT MODELING

2.4.1   Constitutive Behavior

A constitutive behavior can describe superplastic deformation and take account of the effect of damage in superplastic forming, in which much of this ability comes from an accurate constitutive model that characterizes the material behavior.

The parameters of the constitutive equation are typically derived by performing a number of high temperature uniaxial tensile tests on the material. The stress − strain data are fitted to the constitutive models to obtain the coefficients of the equations [153-157]. The effects that is taken into account for superplastic deformation involve temperature, strain hardening/softening, grain growth, cavitation and deterioration in mechanical properties [153].

2.4.2   Conventional Superplastic Models

Based on the postulated deformation mechanism of grain boundary sliding during superplastic deformation, conventional models to account for superplastic behavior were divided into three hierarchical levels [153], i.e. macroscopic (phenomenological), mesoscopic (grain) and atomistic. Those models developed decades ago are summarized in Table 2-4.

In Table 2-4, $K_1 − K_8$ are material constants, σ_0 is the threshold stress, T is absolute temperature, d is grain size, b is Burger's vector, E is Young's modulus, Q is activation energy, k is the Boltzmann constant, D_{gb}, D_L, D_{IPB}, and D_{eff}, are grain boundary, lattice, interphase boundary and effective diffusion coefficients, respectively.

Table 2-4 Superplastic models developed over the years [153].

Name	Year	Equations	Comments
Ball-Hutchison	1969	$\dot{\varepsilon} = K_1 (b/d)^2 D_{gb} (\sigma/E)^2$	GBS accommodated by dislocation climb
Langdon	1970	$\dot{\varepsilon} = K_2 (b/d)^1 D_L (\sigma/E)^2$	Movement of dislocations adjacent to GBs
Gifkins	1976	$\dot{\varepsilon} = K_3 (b/d)^2 D_{gb} (\sigma/E)^2$	Pile-up at triple points (core-mantle)
Gifkins	1977	$\dot{\varepsilon} = K_4 (b/d)^2 D_{IPB} (\sigma - \sigma_0/E)^2$	Pile-up at interphase boundary
Arieli and Mukherjee	1980	$\dot{\varepsilon} = K_5 (b/d)^2 D_{gb} (\sigma/E)^2$	Climb of individual dislocations near GBs
Ruano and Sherby	1984	$\dot{\varepsilon} = 6.4 \times 10^9 (b/d)^2 D_L / b^2 (\sigma/E)^2$	Phenomenological, $T = (0.4 - 0.6) T_m$
Wadsworth and White	1984	$\dot{\varepsilon} = 5.6 \times 10^8 (b/d)^3 D_{gb} / b^2 (\sigma/E)^2$	Phenomenological, $T > 0.6 T_m$
Kaibyshev et al	1985	$\dot{\varepsilon} = K_6 / kT (b/d)^2 D_0 \exp(-Q/kT)(\sigma - \sigma_0/E)^2$	Hardening and recovery of dislocations at GBs
Ashby-Verral	1973	$\dot{\varepsilon} = K_7 (b/d)^2 D_{eff} (\sigma - \sigma_0/E)$ $D_{eff} = D_L \left[1 + (3.3 w/d)(D_{gb}/D_L)\right]$	Rate controlling diffusional accommodation
Padmanabhan	1980	$\dot{\varepsilon} = K_8 (b/d)^2 D (\sigma/E)^2$	Non-rate controlling diffusional accommodation. D may differ from D_L and D_{gb}.

The models widely used for superplastic materials are rigid viscoplastic [50, 158, 159] and visco-elasto-plastic models [43, 154, 155]. Table 2-5 summaries more superplastic constitutive equations for various engineering materials that have been proposed to describe superplastic flow in recent years.

2.4.3 Physical-Based Models

Physical-based material models are models where knowledge about the underlying physical process, dislocation processes etc. are used to formulate the constitutive equations. Implicit-based models are those based on physical mechanisms but in the end the flow stress is expressed in variables, such as effective plastic strains, strain rates and temperature. Explicit-based model has internal state variables that represent some average quantities of the microstructure features, such as dislocation density.

The slip resistance [160, 161], as one of the internal state variables accounting for plasticity models, has been used to understand the deformation kinematics. This is particularly true for pure FCC materials, where the lattice resistance to dislocation motion is small and the flow stress is solely determined by dislocation-dislocation interaction [162]. Dislocation densities are the microstructural variables that govern the evolution of properties [163] and enable a more physical understanding. For materials with high stacking fault energy such as aluminum alloys, the plastic deformation is mainly caused by dislocation glide at low temperatures, but dynamic recovery increases at high temperatures and low strain rates [150]. The modeling work for AA5083 in this research is focusing on the dislocation motion that can describe the flow behavior of the material explicitly.

Table 2-5 Superplastic constitutive models used in various engineering alloys.

Materials	Equations	Comments	Reference
AA5083	$\dot{\varepsilon} = \dfrac{\dot{\sigma}}{E} + C\sigma^n$, $\dot{\varepsilon} = C\sigma^n$	Creep with internal variables	[43]
AA5083	$\dot{\varepsilon} = A(\dfrac{b}{d})^p \left(\dfrac{p(\sigma - \sigma_{th})}{E} \right)^n \exp(-\dfrac{Q_c}{RT})$	GBS and SD creep	[50]
AA5083	$\dot{\varepsilon} = \dfrac{ADG\vec{b}}{kT}(\dfrac{\vec{b}}{d})^p (\dfrac{\sigma}{G})^c$	High temperature tensile tests	[155]
AA5083	$\dot{\varepsilon} = (A/d^2)(\sigma - \sigma_0)^{1+q} + (K + A_1/d_3)\sigma^n$	Dislocation glide-climb	[154]
AA5083	$\dot{\varepsilon} = \left(\dfrac{\overline{\sigma}_m - (k_0 + R)}{C(T)} \right)^{1/m}$	Viscoplastic model	[158]
AA8090	$\overline{\sigma} = K\dot{\overline{\varepsilon}}^m$	Isotropic and ignored strain hardening	[164]
Al-Ti alloy	$\sigma = K\dot{\varepsilon}_{eq}^m \varepsilon_{eq}^n$	Elastic-viscoplastic model	[124]
Ti-6Al-4V	$\dot{\varepsilon} = \left(\dfrac{\sigma - R - k}{K} \right)^{1/m} d^{-\gamma}$	Isotropic hardening variable	[105]
Ti-6Al-4V	$\dot{\varepsilon} = \dfrac{C_i}{d^p}\left[\left(\dfrac{\sigma}{\{1-f_a\}} \right) - \sigma_0 \right]^{1/m} + C_{ii}\left[\dfrac{\sigma}{\{1-f_a\}} \right]^n$	Visco-plasticity with internal variables	[159]
Ti-6Al-4V	$\dot{\varepsilon} = \dfrac{\dot{\sigma}}{E} + C\sigma^n$ $\dot{\varepsilon} = C\sigma^n$	Superplastic creep flow	[165]
Ti-6Al-4V	$\dot{\varepsilon} = \dfrac{\overline{A}(\sigma - \sigma_0)\dfrac{1}{m}}{d^P} + \overline{D}\sigma^N$	Independent mechanisms	[166]
Ti-6Al-4V	$\overset{\triangledown}{\sigma}_{ij} = H(T)i_{jkl}(D_{kl} - D_{kl}^{vp} - D_{kl}^{th})$	Thermo-viscoplastic model	[167]
Ti-6Al-4V	$\dot{\overline{\varepsilon}} = A\overline{\sigma}^n$	Viscoplastic model	[168]
Pb-Sn60	$\overline{\sigma} = 3\mu\dot{\overline{\varepsilon}}$, $\mu = \dfrac{1}{3}K\dot{\overline{\varepsilon}}^{(m-1)}$	Viscous fluid plastic deformation	[156]

There have been numerous attempts to predict stress − strain behavior [169, 170] and to model the forming processes [171-174] based on dislocation concepts [175-179]. The mobility of dislocation density connected to mechanical behavior through Orowan's dislocation ring mechanism has been illustrated to quantitatively construct a dislocation density-based model for aluminum [180]. The mechanical behavior of crystalline matter is a multi-scale problem. The diffusion of solute atoms effects on the motion of dislocations has been discussed earlier [181]. The immobilization of mobile dislocations and slip system effects contribute to the change in the immobile dislocation density inside the cell blocks. Moreover, the thermally activated annihilation by the climb of the dislocations also causes the evolution of the dislocation densities [163]. The Taylor relation [179, 181] is commonly employed to calculate the evolution of the dislocation density, both in the cell interiors [182] and in the cell walls [174].

In respect to the flow behavior at elevated temperature, the climb of dislocations was considered as one of the recovery processes [182]. The dislocation glide associated with recovery was essential feature that described the kinetics of dislocation motion [183]. At this point, the dislocation cores [184] in atomic scales are also controlling macroscopic prediction for plasticity. The diffusion of vacancies is correlated with the recovery of dislocations [185]. This usually occurs at elevated temperature and therefore is a thermally activated reorganization process. The generation of vacancies increases entropy but consumes energy, and their concentration increases with strain rate and inverse temperature [186]. The diffusivity would be enhanced by the generation of vacancies [185].

Militzer *et al* [186] have revealed that the excess vacancies are more important in FCC

than in body-centered cubic (BCC) materials. The high concentration of vacancies near grain boundaries has enhanced the grain mantle creep [55] controlled by dislocation glide and climb processes. The activation energy for generation and migration of a vacancy has been covered from the macroscopic flow stress and strain rate for AA5083 in the physical-based plasticity model.

2.4.4   Superplastic Forming Process Designed by FEM

Conventional SPF manufacturing processes are invariably designed on a trial-and-error basis coupled with considerable experience and some simple calculations. But if the maximum benefit of SPF is to be gained then some form of numerical simulation of the forming process is essential [187].

The use of the FEM coupled with systematic optimization techniques can facilitate the SPF process design. Modeling of the process variables, e.g. pressure cycles [159], strain rate evolution [124] and die design [188], can be derived from these analyses. Most of the experiments and the SPF simulations are carried out by using commercial FEM codes, such as ABAQUS, ANSYS and MARC. In superplastic forming, the ability of the simulation code to predict the deformation behavior of the material is a key factor in developing optimum gas pressure cycles that can form the part in the least time and obtain the best results.

Researchers showed examples of SPF modeling using commercial FEM codes to predict the optimal forming pressure cycles [156, 157], thickness profiles [166] and verifications of experimental measurements [165, 189]. However, FEM for SPF process is still a complicated work when the material behavior is involved. The simulations describing superplastic forming and taking account of deformation

mechanisms, i.e. (a) large deformation in metal forming [167], (b) microstructure and damage evolution [158], (c) forming complex parts with die design [189, 190] and (d) forming path determination [191, 192] are required to optimize the forming process so as to obtain a better formed component with minimum thickness variation, together with the optimum forming temperature and cycle.

2.5 SUMMARY

Superplastic forming is an attractive process in the sheet forming of lightweight alloys with superplasticity. It has some advantages, such as forming large and intricate workpieces, excellent precision and fine surface finish, and little springback or residual stress in the formed parts. The study of this forming process mainly comprises of the material selection, processing technique, microstructure evolution and finite element modeling. Technology gaps in the improvement of superplastic forming come from the specific requirements of the process as follows:

1. **High cost material**: Superplastic materials need to have small grain sizes and to be thermal stable during forming at elevated temperature. Therefore, an alternative process that can form normal material (namely non-superplastic grade) is required.

2. **Low production rate**: The typical forming time for superplastic process lies between 30 to 120 min depending on the parts, while the forming strain rate is in the range of 10^{-5} to 10^{-3} s^{-1}. To address the limitations, it is essential to promote the development of a fast-forming technique for mass production, e.g. for aerospace and automotive applications.

3. **High forming temperature range**: Mostly, the temperature for superplastic forming is higher than $0.5T_m$. At these temperatures, some of the materials may encounter problems, such as oxidation at the grain boundary that reduces the ductility (e.g. for Ti-6Al-4V) or grain growth that causes unstable forming behavior (e.g. for magnesium alloy AZ31 and aluminum alloy AA5083).

4. **High degree of thinning**: The material is normally subjected to pure stretching stress during conventional SPF. The expansion ratio relies significantly on the formability at the prescribed strain rates and temperatures.

CHAPTER 3   EXPERIMENTAL DETAILS

3.1   MATERIAL CHARACTERIZATION

3.1.1   Materials for Study

AA5083 is a non-heat-treatable aluminum alloy possessing moderate to good mechanical strength (155 − 300 MPa) and excellent resistance to corrosion. Ti-6Al-4V is characterized as an alpha rich alpha-beta titanium alloy. In this study, non-superplastic grade AA5083 sheets with thickness of 3 mm were used for tensile test and superplastic-like forming. Ti-6Al-4V alloy sheets with thickness of 1.6 mm were used to expand the application of superplastic-like forming process. The compositions of AA5083 and Ti-6Al-4V alloys are provided in Tables 3-1 and 3-2, respectively.

Table 3-1 Compositions (weight percentage) of AA5083.

Element	Si	Fe	Cu	Mn	Mg	Cr	Ti	Zn	Al
AA5083	0.19	0.36	0.04	0.6	4.5	0.11	0.02	0.03	Remainder

Table 3-2 Compositions (weight percentage) of Ti-6Al-4V alloy.

Element	Al	V	Fe	C	N	H	O	Ti
Ti-6Al-4V	6.08	3.96	0.12	0.019	0.006	0.0011	0.11	Remainder

3.1.2   Microstructure Examination

For AA5083 samples, an aging treatment at 150ºC for 24 h was carried out to successfully reveal the microstructure by decorating the grain boundary with precipitates [11]. The samples were then mechanically polished and etched with Graf Sergeant reagent (15.5 ml HNO_3, 0.5 ml HF, 3 g Cr_2O_3 and 84 ml H_2O). Figure 3-1(a) shows the optical microstructure of AA5083 in annealed condition. The grains were fairly equiaxed. The grain size was determined by the linear intercept method [55], measuring 12.9 μm in mean grain size.

The specimens of Ti-6Al-4V alloy were etched using Kroll's reagent (5 ml HNO_3, 10 ml HF and 85 ml H_2O). All the specimens used for microstructural observations were machined along the cross-section of sheet thickness. The microstructure in as-received condition can be seen in Figure 3-1(b), exhibiting inhomogeneous grain structures. The mean grain size was measured to be 3.4 μm.
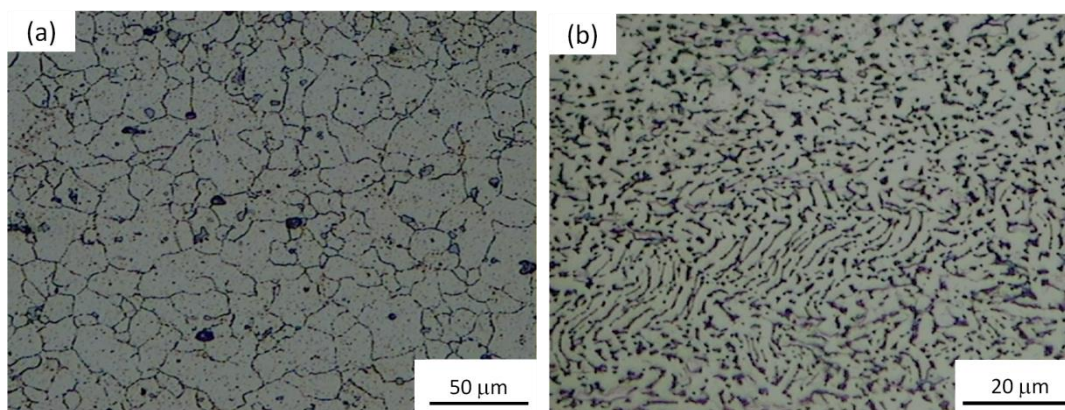
Figure 3-1 Optical micrographs of (a) annealed AA5083 and (b) as-received Ti-6Al-4V.

3.2   HIGH TEMPERATURE TENSILE TEST

3.2.1   Tensile Specimen

AA5083-H321 has been annealed for 2 h at 345ºC before testing and forming to obtain homogeneous formability and strength. Tensile specimens with 20 mm gauge lengths and 4 mm gauge widths, as illustrated in Figure 3-2, were cut from the annealed and formed AA5083. The thickness of as-received Ti-6Al-4V sheet is 1.6 mm, and the gauge length was determined to be 11 mm [78].
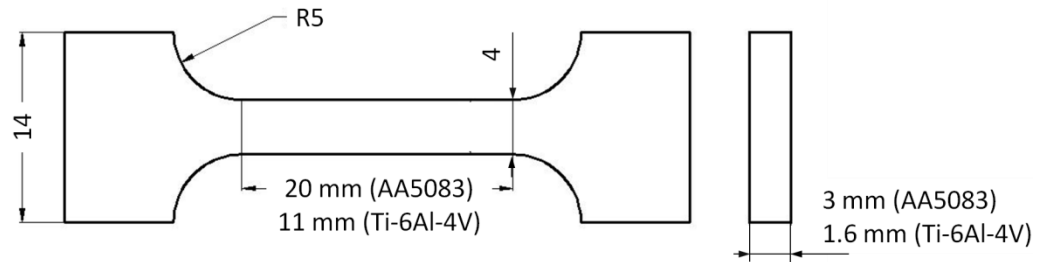
Figure 3-2 Dog-bone shaped tensile specimen (unit: mm).

3.2.2   Tensile Test Procedures

Tensile tests of the specimens were performed using Instron 8500 testing machine equipped with an electrical resistance furnace chamber. The specimens were tested in the temperature range from room temperature to 550ºC and at constant crosshead velocities, with the corresponding initial strain rates from 10^{-4} to 3×10^{-1} s^{-1}.

The time required to raise the temperature to the desired value greatly depends on the test temperature, which could range from 1 to 40 min. In order to make it fully heated to the desired temperature, tensile tests were started 3 min after the preset temperature having been reached. Temperature fluctuation inside chamber usually was less than 5°C during the whole testing process. The machine was stopped immediately once the specimen fractured at its maximum elongation. The specimen was then water quenched so as to maintain its original microstructure in the deformation stage.

3.2.3 True Stress and True Strain

The true stress and true strain can give a true indication of the deformation characteristics of a material, because it is based on the actual cross-sectional dimension of the specimen during testing. If both parameters are all based on instantaneous measurements, the obtained curve is known as a true stress − true strain curve.

The raw data recorded during the tensile tests are based on engineering stress − engineering strain measurements. Equations from (3-1) to (3-9) describe the different definitions of stress and strain.

Engineering strain:

$$e = \frac{\Delta L}{L_0} = \frac{1}{L_0} \int_{L_0}^{L} dL \qquad\qquad \text{Eq. (3-1)}$$

True strain:

$$\varepsilon = \int_{L_0}^{L} \frac{dL}{L} = \ln \frac{L}{L_0} \qquad\qquad \text{Eq. (3-2)}$$

$$e = \frac{\Delta L}{L_0} = \frac{L - L_0}{L_0} = \frac{L}{L_0} - 1 \qquad\qquad \text{Eq. (3-3)}$$

$$e + 1 = \frac{L}{L_0} \qquad\qquad \text{Eq. (3-4)}$$

$$\varepsilon = \ln \frac{L}{L_0} = \ln(e + 1) \qquad\qquad \text{Eq. (3-5)}$$

Engineering stress:

$$s = \frac{P}{A} \qquad\qquad \text{Eq. (3-6)}$$

True stress:

$$\sigma = \frac{F}{A} = \frac{F}{A_0} \frac{A_0}{A} \qquad\qquad \text{Eq. (3-7)}$$

$$\frac{A_0}{A} = \frac{L}{L_0} = e + 1 \qquad\qquad \text{Eq. (3-8)}$$

So,

$$\sigma = \frac{P}{A_0}(e + 1) = s(e + 1) \qquad\qquad \text{Eq. (3-9)}$$

3.3 SUPERPLASTIC-LIKE FORMING

3.3.1 Experimental Set-Up

Dry graphite was applied as lubricant, and evenly sprayed on both surfaces of the workpiece. The superplastic-like forming was carried out on a Murdock 140-10000 SPF/DB 100 Ton Press, as shown in Figure 3-3(a). The force can be varied up to 90.7 tonnes (100 US tons), and operating temperature set up to 982ºC. Argon gas was used

as forming pressure for the bulging. Due to limitations of the forming press, the gas blow stage could be conducted with the maximum pressure of 4.2 MPa.

Figure 3-3(b) shows the die assembly for superplastic-like forming. During forming, the entire furnace is heated to a preset operating temperature (namely global temperature). The lower die is equipped with 8 cartridge heaters, by which a non-isothermal heating system is formed. The temperature in these specific zones will be maintained at a high level (namely local temperature).
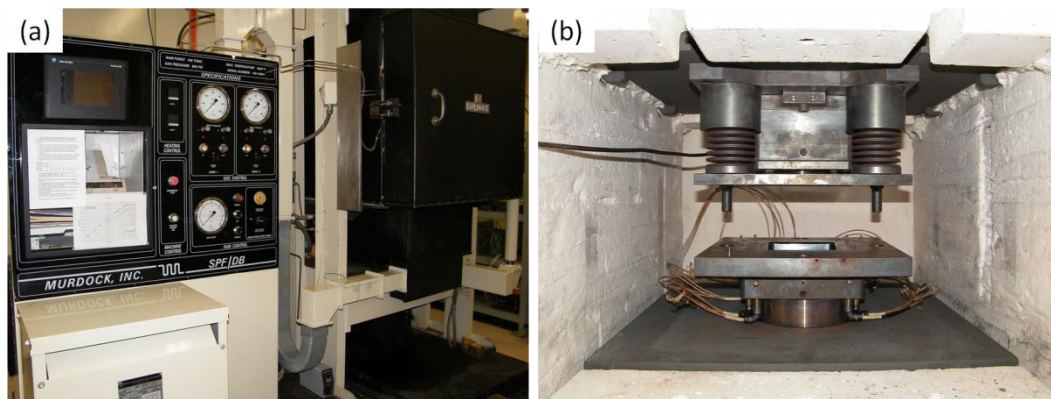
Figure 3-3 Experimental set-up of superplastic-like forming machine: (a) Murdock SPF/DB press and (b) die assembly inside the furnace.

The technology proposed in this study is a combination of mechanical pre-forming (namely hot drawing) and gas forming (also called blow forming). This combination can take advantage of benefit of both drawing and superplastic forming to establish a fast forming process. The major components used in the process are illustrated in Figure 3-4 and described as follows:
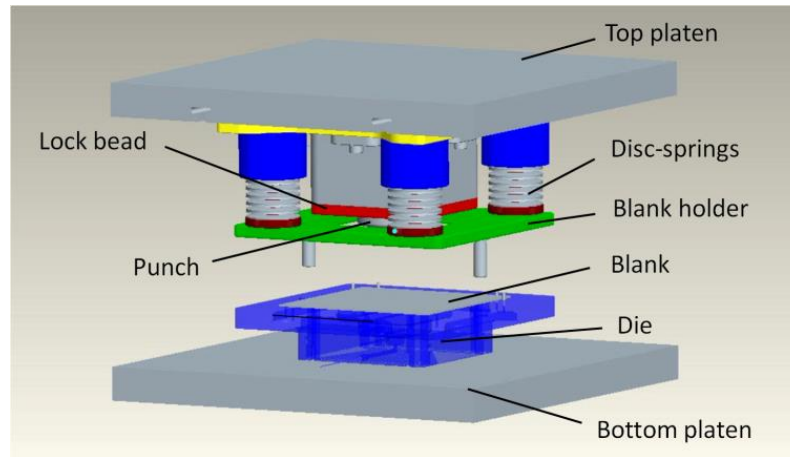
Figure 3-4 Components of the die assembly for superplastic-like forming.

1. **Die:** A rectangular die with three steps is used to demonstrate the different level of surface expansion. The surface expansion ratio of a sheet is defined as the percentage increase in surface area that occurs during forming. The three different steps indicate different deformation levels, with 80%, 135% and 150% surface expansion ratios respectively.

2. **Blank holder:** A blank holder was used to avoid wrinkling during hot drawing. Four series of disc-springs made from INCONEL material are utilized to apply load on it. The blank holder force as a function of the deflection of disc-springs is plotted in Figure 3-5.

3. **Punch:** The punch was designed specifically for drawing the material into the die cavity before applying gas pressure on the sheet. The holding system for the punch is changeable so as to study the effect of hot drawing. Two punches with strokes of 20 and 43 mm were used.

4. **Sealing system:** The sealing system was designed to ensure no gas leakage during blow forming. A lock bead was used in this process for sealing purpose.
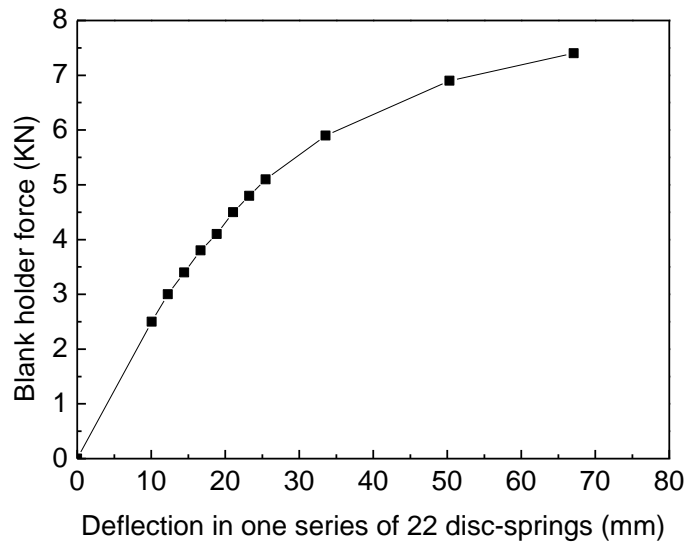
Figure 3-5 Blank holder force as a function of the deflection of disc-springs.

3.3.2   Forming Procedures

The main principle of the hybrid forming process is to mechanical pre-form more material into the die chamber for further deformation during pressuring. As illustrated in Figure 3-6, the forming process comprises of three stages as follows:

(a) Heating stage

The workpiece on the die is heated to an operating temperature, which is 400ºC for AA5083 and 800ºC for Ti-6Al-4V. The cartridge heaters equipped inside the die are used for selective heating at the die radii to make the local temperature in those regions is about 20ºC higher than the operating temperature, as shown in Figure 3-6(a).

(b) Hot drawing and sealing stage

At this stage, the sheet is drawn into the die cavity by the punch at the working temperature, and as a result some material at the flange area flows into the deformation sections of the sheet. As shown in Figure 3-6(b), the punch moves down at a constant speed until it reaches a total displacement of 20 mm (or 43 mm) within 9 s. Subsequently, significant amount of blank-holder force and the lock bead are used to ensure that the flange area is sealed completely.

(c) Gas forming stage

After hot drawing, the pre-formed sheet is maintained in the hot die till the temperature adjacent to the corner radii rises to the prescribed level. Finally, argon gas is applied onto the sheet so as to further form the sheet into the die configuration, as shown in Figure 3-6(c). The rate of pressurization is normally determined by the application of finite element modeling. For AA5083 and Ti-6Al-4V alloys, the gas forming operation is completed within 8 and 16 min, respectively.
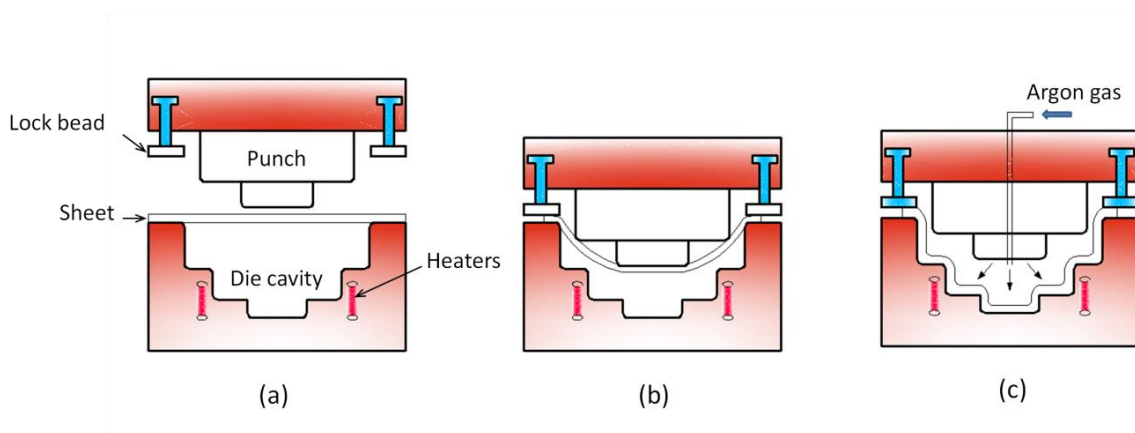
Figure 3-6 Schematic of the superplastic-like forming process: (a) heating and clamping, (b) hot drawing and sealing and (c) gas forming.

3.4   MICROTEXTURE DETERMINATION

3.4.1   Electron Backscatter Diffraction

To observe the internal microstructures during deformation, electron backscatter diffraction (EBSD) is the most recently developed scanning electron microscope (SEM) based technique. This technique was considered as an important tool for quantitative metallography [145, 146, 148, 193]. By using EBSD, it is possible to collect and analyze large sample populations of individual grains (microstructures) and their preferred orientation (textures).

Figure 3-7 shows a schematic of the main components of an EBSD system. An EBSD detector system typically consists of a phosphor screen and a sensitive charge coupled device (CCD) camera for viewing the diffraction pattern. The acquisition suite of programs is required to acquire the diffraction data, index and analyze the diffraction patterns as well as display results and do further processing [194].
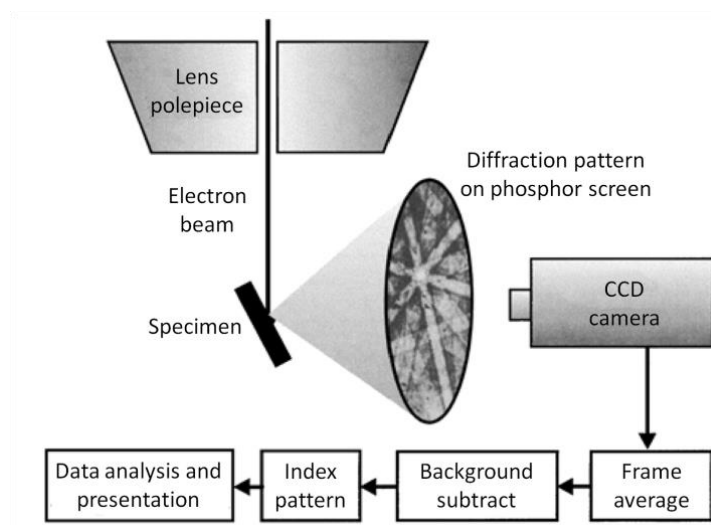
Figure 3-7 Schematic diagram of a typical EBSD installation [145].

3.4.2 EBSD Specimen Preparation

To investigate the evolution of microstructure and texture in different forming stages, the as-received (or annealed) and hot deformed samples have been characterized. After hot deformation, the formed part was immediately water quenched, and cut (across the transverse plane) for optical and EBSD observations. The AA5083 samples were initially ground and mechanically polished, and then electropolished in a $HClO_4$: C_2H_5OH (1 : 4) solution at room temperature and 20 V for 20 s. The Ti-6Al-4V samples were electropolished in a $HClO_4$: CH_3COOH (1 : 8) solution at room temperature and 30 V for 30 s [195].

3.4.3 Operation of EBSD Mapping

The EBSD examinations were conducted using a JEOL 7600F field emission scanning electron microscope (FE-SEM) with an Oxford Instruments HKL® EBSD system working at 20 kV with a working distance of 24 mm and a 70° tilt angle. The CHANNEL® 5 suite of programs developed by Oxford Instruments was adopted to manipulate, analyze and display EBSD data.
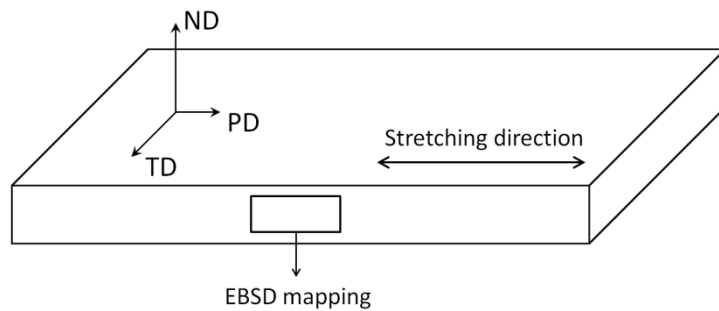
Figure 3-8 Cross-section of the sheet sample used for EBSD mapping.

The primary sample axes (CS_0), e.g. plane direction (PD), transverse direction (TD) and normal direction (ND), have been brought into coincidence with the microscope coordinate system (CS_m) by aligning the specimen surface. The mapping data were measured in the PD-ND plane, as the cross-section of the sample shown in Figure 3-8. During the course of forming, the sheet material was mainly stretched along the stretching direction.

3.4.4 EBSD Data Acquisition

For the texture and grain orientation measurements, an area of 0.8×0.6 mm^2 was observed using a scanning step size of 2 μm. For the microstructure determination, individual specimen locations of 200×150 μm^2 were investigated using step sizes from 0.5 to 1 μm. For the data sets obtained from EBSD mapping, all the fractions of successfully indexed data pixels were higher than 85%, which was thought reliable for determining the crystallographic texture [196].

For the inverse pole figure (IPF) maps, the grains were colored according to orientation, with red, green and blue levels proportional to the three Euler angles (Euler contrast). Low angle grain boundaries (LAGBs) between 2° and 15° were depicted as white lines, and high angle grain boundaries (HAGBs) greater than 15° as black lines. In order to avoid spurious boundaries, misorientation below 2° was not taken into account. Grain size measurement was carried out in the EBSD software by determining the grain areas exclusive of border grains.

3.5   FINITE ELEMENT MODELING

A dislocation density-based model was coupled with the constitutive equations in the user subroutine interface FORTRAN, and was implemented in the commercial finite element code MSC.MARC. According to the actual process route, modeling was carried out to predict the hot drawing and gas forming procedures in sequence.

For the first stage of the simulation, the load was applied by the punch displacement. The two-stepped punch moved down at a constant speed until it reached a total displacement of 43 mm in 9 s. During the second stage of the simulation, the punch was fixed and an external pressure was applied on the surface of the sheet. The pressure control in this loadcase was used to automatically adjust the pressure on the sheet to maintain the target strain rate at 2×10^{-3} s^{-1} throughout the forming, as the pressure cycle plotted in Figure 3-9.
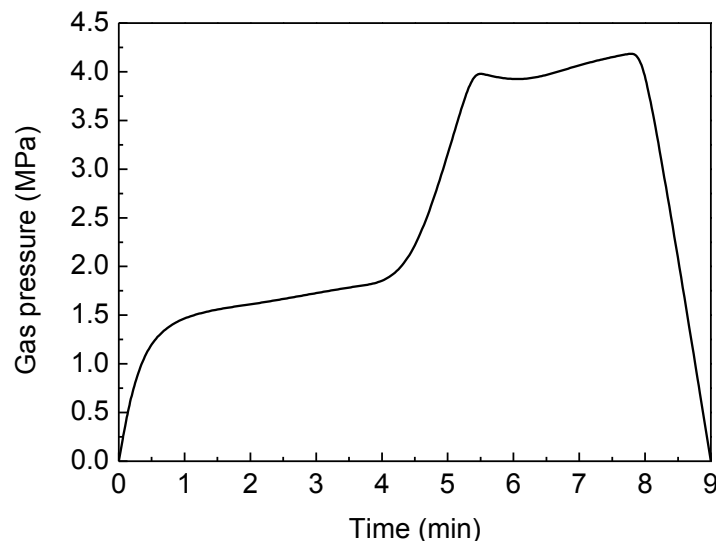
Figure 3-9 Pressure cycle predicted by FEM for gas forming of the pre-formed AA5083 sheets at 400 °C and a target strain rate of 2×10^{-3} s^{-1}.

It should be noted that, for a superplastic material, it usually has good superplasticity at a specific strain rate. However, the deformation mechanisms of superplastic materials differ from the non-superplastic grade. The non-superplastic grade AA5083 used in the experiment was deemed to be formed at the constant strain rate of 2×10^{-3} s^{-1}, not only because it has a good formability lying between the strain rate of 10^{-4} to 10^{-3} s^{-1}, but also due to the limitation of the forming press. The average strain rate of all the elements within the deformation area was maintained at 2×10^{-3} s^{-1} during gas forming. The predicted pressure schedule is presented in Figure 3-9. It reveals that a higher gas pressure is required with forming time in order to generate sufficient membrane stress as the panel curvature becomes larger.

Friction is a complex physical phenomenon during sheet forming, as it depends on many variables [197]. The friction coefficients were varied with forming conditions, such as temperature, strain rate and normal pressure [198]. No direct measurement of friction coefficient between aluminum and tool material was carried out in this study. Coulomb friction model of bilinear type was applied in the simulations [199]. It has been indirectly predicted from forming experiments [200] that the friction constant was quite high with graphite as the lubricant, which was at the level of 0.4. According to the effect of friction [166], the thickness prediction was sensitive to the value of friction constant. Therefore, the friction coefficient of 0.4 was chosen to account for surface interaction between the sliding sheet and the die assembly.

CHAPTER 4   HIGH TEMPERATURE BEHAVIOR OF

AA5083

Non-superplastic grade AA5083 was investigated during high-temperature tensile testing to study its formability. The results of tensile tests and microstructures were shown, which indicated the deformation properties under various operating conditions. The flow stress as a function of temperature and strain rate has been used to determine its formability. In addition, the strain rate sensitivity index (m value) was obtained. Microstructure changes, including cavitation and grain growth were also found as a result of the variations in strain rate and temperature.

4.1   HIGH TEMPERATURE TENSILE TEST

4.1.1   Tensile Test Results

The tests cover the temperature range from 300 to 550ºC and the initial strain rate from 10^{-4} to 3×10^{-1} s^{-1} on AA5083 specimens. The results of high temperature tensile tests are provided in Table 4-1.

The largest percent elongation-to-failure is 93% for AA5083 at 500ºC. The results are fairly consistent with the trend that a higher elongation can be obtained at relatively higher temperature. However, the material used in this study is a normally rolled and annealed alloy, which cannot be considered as the superplastic material. More efforts

should be concerned to the formability and make it possible to be utilized under the

superplastic-like forming conditions.

Table 4-1 Summary of high temperature tensile test results of AA5083.

	Strain rate (s⁻¹)	Yield Stress (MPa)	UTS (MPa)	Elongation (%)
300 ℃	3×10^{-1}	161	191	42
	10^{-1}	155	176	45
	2×10^{-2}	142	151	44
	10^{-2}	138	146	44
	10^{-3}	76	87	59
	10^{-4}	29	47	64
400 ℃	3×10^{-1}	116	122	64
	10^{-1}	86	94	70
	10^{-2}	40	55	72
	2×10^{-3}	30	44	80
	10^{-3}	18	31	79
	3×10^{-4}	14	22	70
	10^{-4}	13	19	64
500 ℃	3×10^{-1}	71	73	93
	10^{-1}	56	60	87
	2×10^{-2}	24	28	84
	10^{-2}	25	27	82
	3×10^{-3}	19	21	75
	10^{-3}	14	17	57
	3×10^{-4}	12	14	42
	10^{-4}	10	12	32
550 ℃	3×10^{-1}	51	54	87
	2×10^{-2}	22	24	72
	10^{-2}	21	22	72
	10^{-3}	12	13	37
	10^{-4}	8	9	21

4.1.2 True Stress – True Strain Curves

Figure 4-1 shows the true stress vs. true strain curves for a series of initial strain rates at 300ºC. It reveals that the tensile stress increases with decreasing strain rate. Generally, weak strain hardening effect dominates all the tensile strains. The material exhibits higher strain hardening at strain rate of 10^{-4} s^{-1} as compared to that of 10^{-2} s^{-1}. The enhanced strain hardening may be because of the occurrence of dynamic grain growth [11].
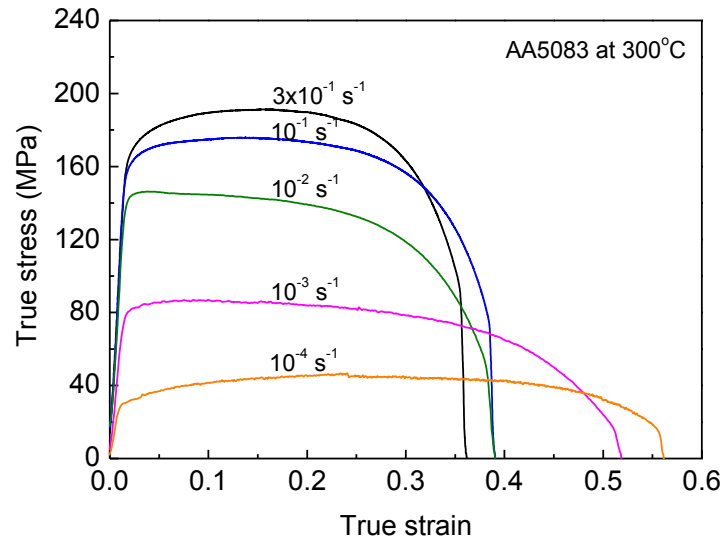
Figure 4-1 True stress – true strain curves of AA5083 at 300 ℃.

The curves of 400ºC show the similar profiles as that of 300ºC, as shown in Figure 4-2. The flow stress is highly correlated with strain rate, from which it is a higher strain rate showing a significantly higher flow stress. The material exhibits low strain hardening at the high strain rates of 10^{-1} and 10^{-2} s^{-1}. Furthermore, the flow stress also decreases significantly with increasing temperature.
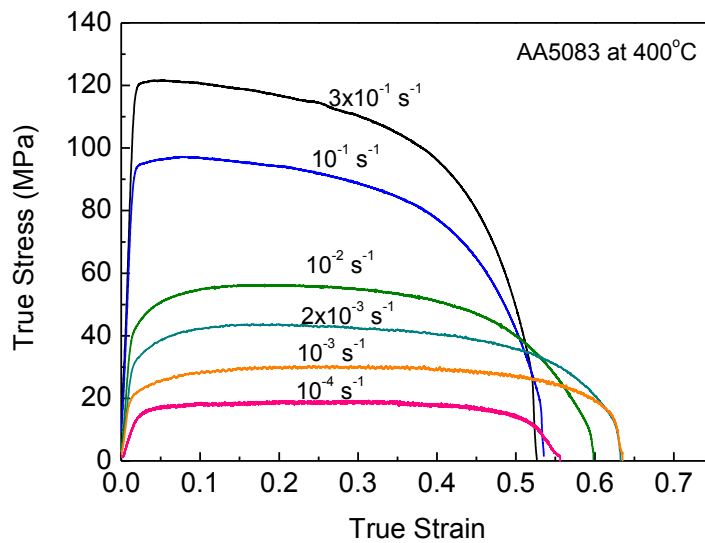
Figure 4-2 True stress – true strain curves of AA5083 at 400 °C.
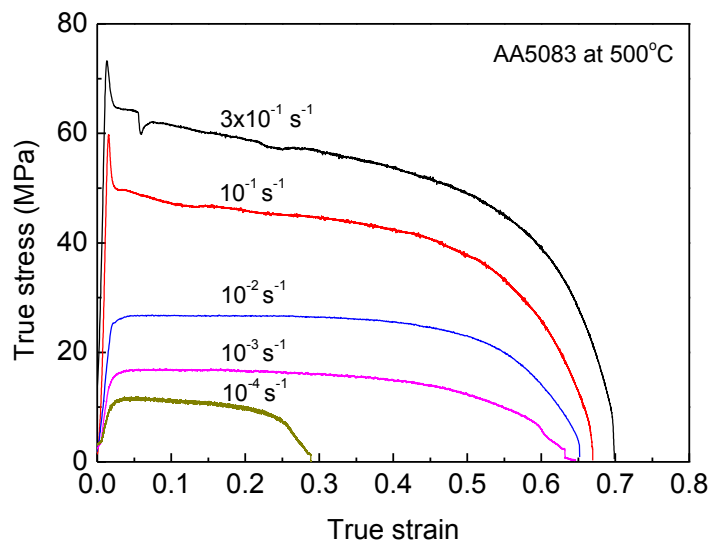
Figure 4-3 True stress – true strain curves of AA5083 at 500 °C.

Figures 4-3 and 4-4 show the true stress – true strain curves at 500 and 550ºC, respectively. For the strain rate greater than 10^{-1} s^{-1}, the curve exhibits a high (peak) initial stress within a small strain ($\varepsilon < 0.02$), and a sharp decrease is found occurred

following the increasing strain. This is evidenced in dynamic recrystallization (DRX) [201]. DRX may commence well before the peak stress during hot deformation where the deformed grains are replaced by strain free (recrystallized) grains [150].

It appears that the flow stress shows a wide range ($\varepsilon > 0.02$) of steady state, where it gradually falls with increasing strain. However, recrystallization can only be found at the faster strain rates ($\dot{\varepsilon} \geq 10^{-1}$ s^{-1} at 500ºC and $\dot{\varepsilon} \geq 10^{-2}$ s^{-1} at 550ºC), from which it can also be concluded that this kind of softening may be activated by the fast straining.
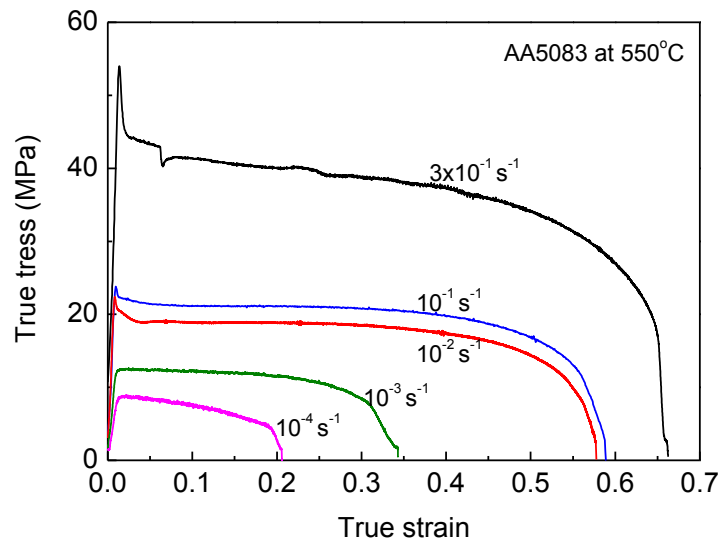
Figure 4-4 True stress – true strain curves of AA5083 at 550 ºC.

4.1.3 Percent Elongation-to-Failure

The percent elongation-to-failure is used as a measurement of the formability of a material, and is typically a function of strain rate and temperature. The tensile elongations plotted as a function of log strain rate are shown in Figure 4-5.

The tensile elongation increases with increasing strain rate and at temperatures greater than 400ºC. This trend is different from the superplastic materials with lower strain rate showing higher percent elongation-to-failure [49, 56-58]. However, the elongation does not vary much with strain rate at 400ºC. That is probably due to the influence of less cavitation and weaker strain hardening at lower temperature. The failure under these conditions is necking due to stress concentration at the failure tips.

The percent elongation-to-failure at 500 and 550ºC increases with increasing strain rate, where it shows the largest elongation at strain rate of 3×10^{-1} s^{-1} and the smallest elongation at strain rate of 10^{-4} s^{-1}. The maximum tensile elongation is 93% for AA5083 at 500ºC. There is an increasing amount of cavities and grown grains formed during tensile testing at high temperatures and very slow strain rates. As a result, the tensile elongation is much more decreased when the tensile test is conducted above 500ºC and strain rate below 10^{-2} s^{-1}.
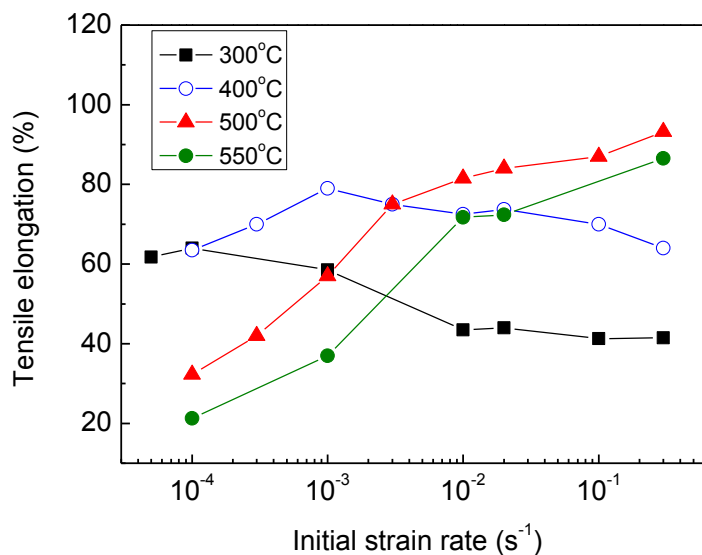
Figure 4-5 Tensile percent elongation-to-failure of AA5083 as a function of initial strain rate.

4.1.4 Strain Rate Sensitivity of Flow Stress

The flow stress as a function of strain rate at different temperatures is plotted in Figure 4-6. It can be found that all the curves at different temperature show typical sigmoidal profiles. The flow stress increases with increasing strain rate.
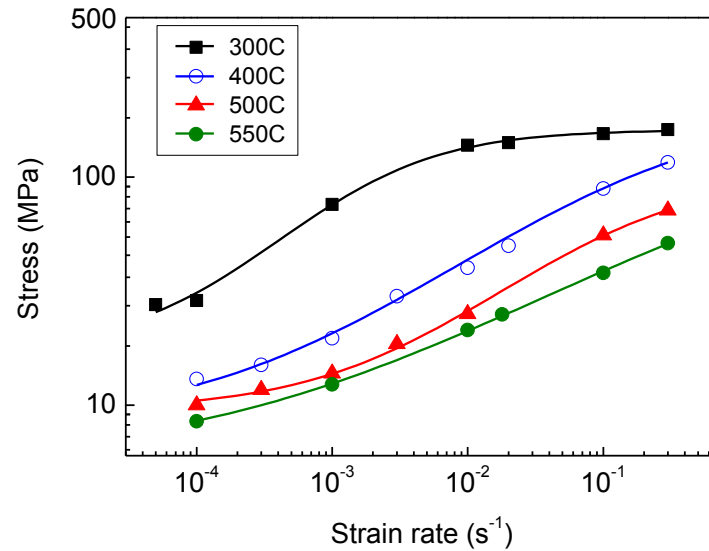
Figure 4-6 Strain rate dependence of flow stress for AA5083 at different temperatures.

The strain rate sensitivity index (m value), calculated from slopes of the log stress vs. log strain rate, is plotted in Figure 4-7. For superplastic behavior, m value is greater than or equal to 0.3 [41]. Unlike the superplastic material, a maximum m value of 0.41 is obtained for AA5083 at 300ºC. The influence of temperature on m value can also be concluded from the plot. The peak m value seems to be decreased with increasing temperature. Additionally, the m value confers a high resistance to necking development and results in high tensile elongations [41]. Therefore, the maximum elongation coincides with the range of highest m value distribution.
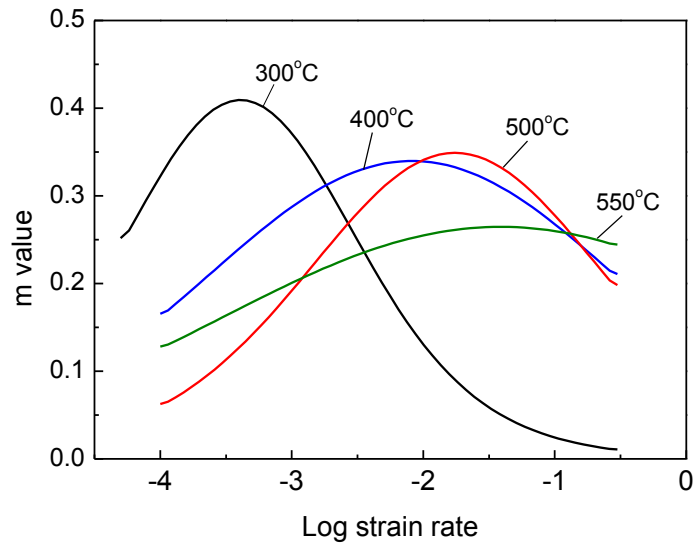
Figure 4-7 The *m* values plotted as a function of log strain rate for AA5083 at different temperatures.

4.2   MICROSTRUCTURES DURING HIGH TEMPERATURE DEFORMATION

4.2.1   Microstructure Changes

The microstructures of AA5083 tested at 300ºC with initial strain rates of 10^{-1} s^{-1} and 10^{-4} s^{-1} in the grip and gauge regions are shown in Figures 4-8 and 4-9, respectively. As expected, the grains in the deformed samples appear to be coarser due to grain growth during high-temperature tensile testing. Compared within the two different tensile strain rates, the grains seem to be larger when testing is conducted under the faster strain rate of 10^{-1} s^{-1}.
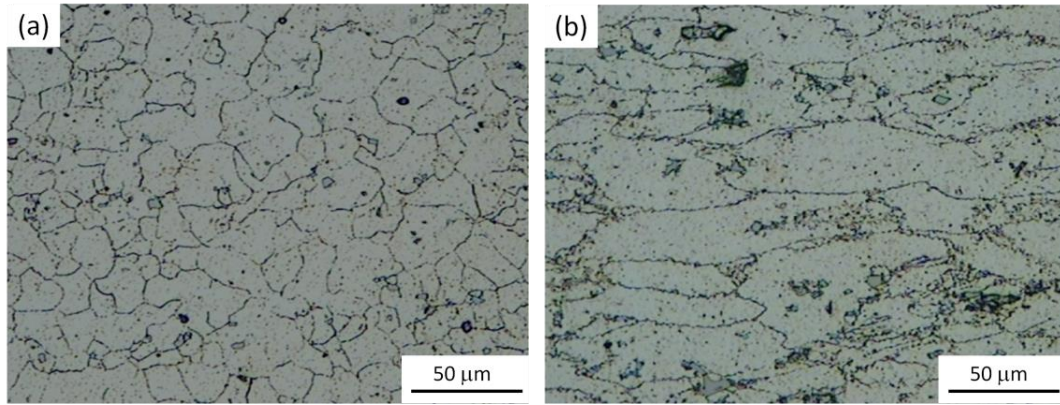
Figure 4-8 Microstructures of AA5083 tested at 300 ℃ and initial strain rate of 10⁻¹ s⁻¹: (a) grip and (b) gauge region.
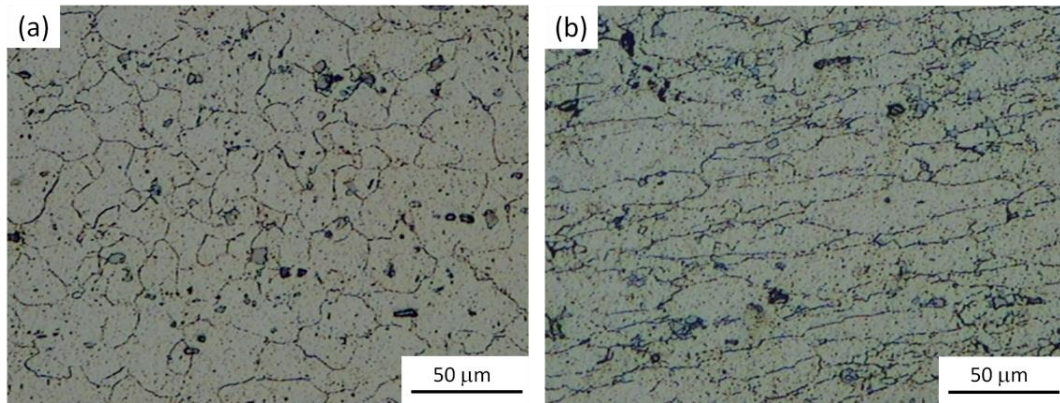
Figure 4-9 Microstructures of AA5083 tested at 300 ℃ and initial strain rate of 10⁻⁴ s⁻¹: (a) grip and (b) gauge region.

Micrographs of AA5083 tested at 400ºC with initial strain rates of 10^{-1} s^{-1} and 10^{-4} s^{-1} in the grip and gauge regions are provided in Figures 4-10 and 4-11, respectively. It is reported that the initial heating prior to deformation causes recrystallization and the formation of equiaxed grain structure [49]. The increase in grain size caused by the longer cycle time is evident by comparing the microstructure in Figure 4-10(a) to that in Figure 4-11(a). In addition to grain growth, fine grains are visible among the coarse grains (in Figure 4-10(b)), which is ascribed to the occurrence of recrystallization.

59
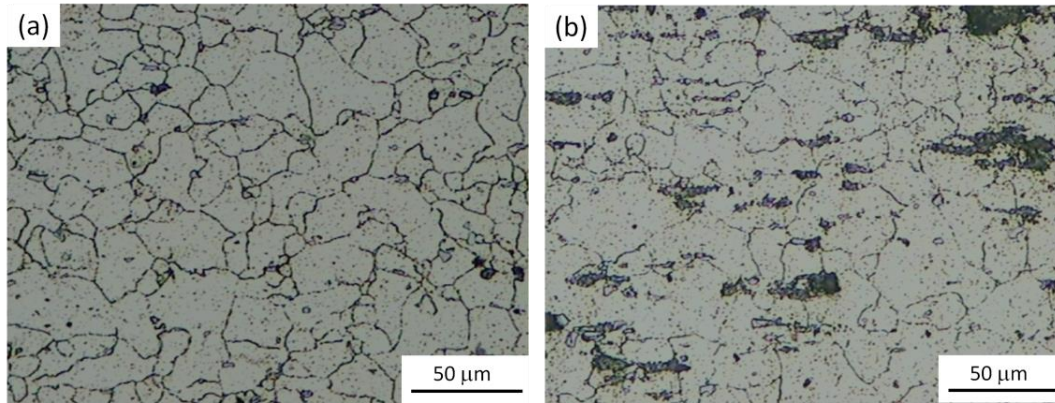
Figure 4-10 Microstructures of AA5083 tested at 400 ℃ and initial strain rate of 10^{-1} s^{-1}: (a) grip and (b) gauge region.
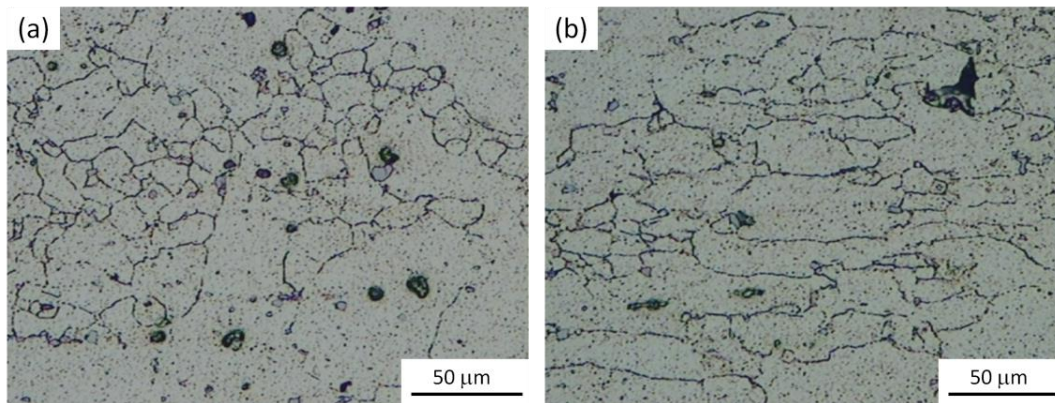
Figure 4-11 Microstructures of AA5083 tested at 400 ℃ and initial strain rate of 10^{-4} s^{-1}: (a) grip and (b) gauge region.

The increase in grain growth caused by different temperature is obvious by comparing the microstructure changes in Figures 4-8 and 4-12. Similar to superplastic materials [49], the alloy shows much more grain growth at 500ºC. The average grain size of grip region is about 22.5 μm at 300ºC, while some of the grains grow as big as 200 μm at 500ºC. The microstructure also contains a wide range of grains, in which there are many fine grains formed due to recrystallization, as shown in Figure 4-12(b).
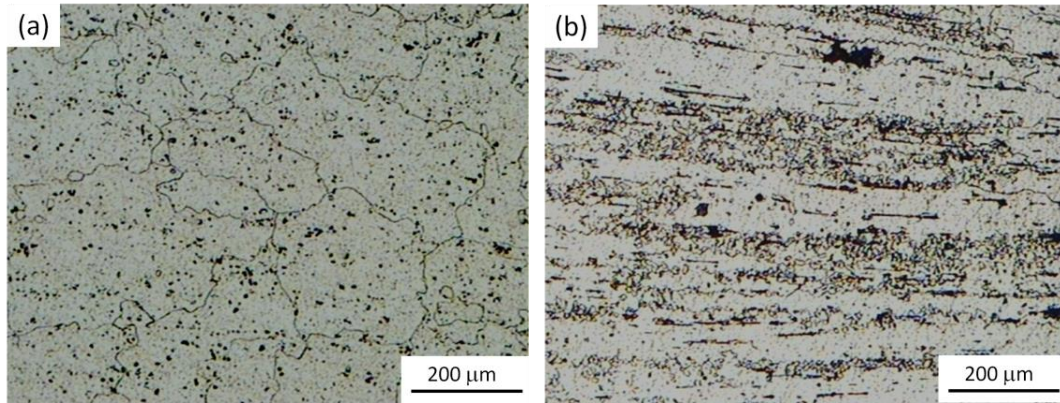
Figure 4-12 Microstructures of AA5083 tested at 500 ℃ and initial strain rate of 10^{-1} s^{-1}: (a) grip and (b) gauge region.
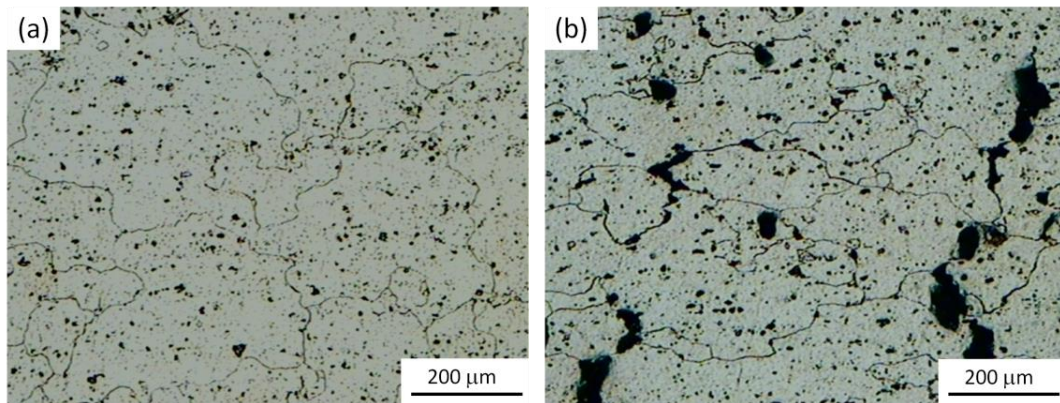
Figure 4-13 Microstructures of AA5083 tested at 500 ℃ and initial strain rate of 10^{-4} s^{-1}: (a) grip and (b) gauge region.

4.2.2   Cavitation Phenomenon

Cavitation has been observed in superplastic alloys including aluminum, copper, iron, lead, silver, titanium and zinc. The cavities are internal voids, which are located on the grain boundaries of the deformed material. Failure during superplastic deformation occurs as a result of the nucleation, growth and coalescent of internal cavities. In

general, as an important requirement, tensile stress plays a great role for initiation and propagation of the cavities within the superplastic regime.

Formation of the voids or cavities at the intergranular locations of non-superplastic AA5083 is visible during tensile testing. Little cavitation is observed in the grip region of tested sample because of low tensile stress induced in this area, while much more and larger cavities are produced in the gauge region after tensile testing.

Figure 4-14 shows the typical micrographs of the fracture tips, from which the influences of temperature and strain rate to the cavitation phenomenon and fracture behavior are obtained. It has been widely accepted that the failure is mostly due to external necking at a higher strain rate (Figure 4-14(a)); but it changes to internal cavitation at a lower strain rate (Figure 4-14(b)). Because of the inherent resistance to necking during deformation, it is possible for it to sustain a large degree of cavitation before fracture. It appears that the cavities have begun to coalesce with each other to form a larger void between grains. As a result, there are more cavities with the decrease of strain rate.

The fracture tip has a jagged appearance especially at the low strain rates. This is most likely because the sample fractures along the intergranular cavities, as shown in Figure 4-14(b). In this region, the section is weakened by these cavities and may no longer support the flow stress. In addition to the tensile stress, there appears to be an effect of temperature on the amount of cavitation, with higher temperature showing more cavitation than that of lower temperature. Comparing the microstructures at 300 and 500 ℃, it is found that there are much more cavities and grain growth at 500 ℃.
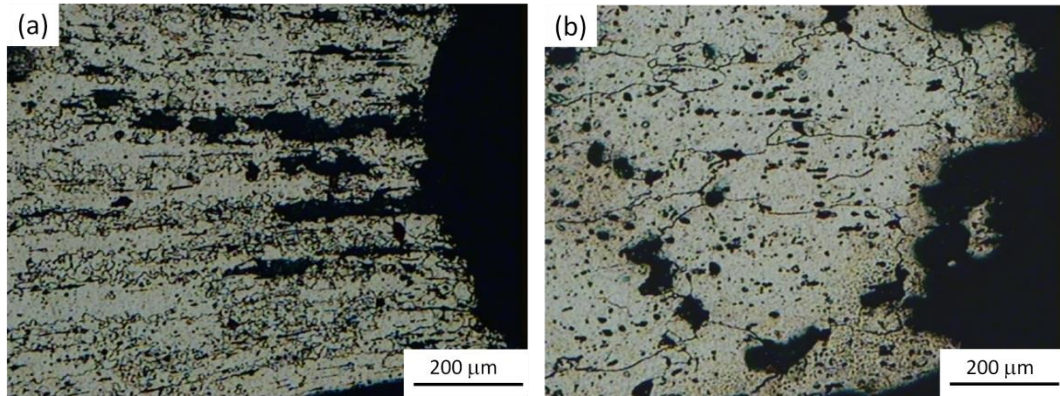
Figure 4-14 Micrographs of the fracture tips of AA5083 tested at 500 ℃: (a) 10^{-1} s^{-1} and (b) 10^{-4} s^{-1}.

Although the small tensile elongation indicates that AA5083 is a non-superplastic grade material, the relative low flow stress and moderate ductility at specific temperatures and strain rates can be taken into account. Hence, the moderate formability could be applied by using the non-superplastic material to exploit a sheet-metal forming technology that does not require full superplasticity.

4.3 SUMMARY

Uniaxial tensile tests have been conducted at various temperatures and strain rates to investigate the high-temperature formability of the non-superplastic grade AA5083. The conclusions are summarized as follows:

1. AA5083 exhibits relatively weaker strain hardening at a relatively lower strain rate. The flow stress increases with increasing strain rate for a given temperature.

2. The largest percent elongation-to-failure is 80% at 400 °C with a strain rate of 2×10^{-3} s^{-1}, and 93% at 500 °C with a strain rate of 10^{-1} s^{-1}. The peak of elongation coincides with the range of highest *m* value.

3. The grains appear to be coarser in the samples deformed due to the grain growth at the high temperatures. The mean grain size of AA5083 is about 12.9 μm in annealed condition, while it increases to 22.5 μm at 300 °C and as big as 200 μm at 500 °C.

4. Dynamic recrystallization occurred during tensile testing at temperatures greater than 500 °C and strain rates faster than 10^{-1} s^{-1}. The deformed grains appeared to be coarser with increasing test temperature and time.

5. There were more cavitation accompanied by initiation, propagation and coalescence of internal cavities observed at higher temperatures and slower strain rates. The tensile samples fractured mainly due to internal cavitation at lower strain rates ($< 10^{-2}$ s^{-1}), but the failure mode changed to external necking at higher strain rates ($> 10^{-1}$ s^{-1}).

CHAPTER 5   SUPERPLASTIC-LIKE FORMING OF AA5083

The purpose of this chapter is (i) to discuss the design of a prototype hybrid process and (ii) to investigate the process parameters (i.e. punch shape, temperature and initial sheet size) on the formability of AA5083 in terms of material draw-in, bulge height, thickness distribution and microstructure.

5.1   FORMING PROCESS DESIGN

5.1.1   Prototype Die Design

From the prototype die design, a maximum surface expansion of 150% would be attained when forming a sheet into the three-stepped rectangular die. The surface expansion ratio of the sheet in this study is defined as the percentage increase in surface area that occurs during superplastic-like forming.
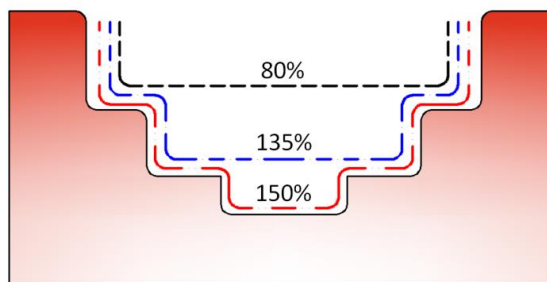
Figure 5-1 Schematic of the surface expansion amount in the die cavity.

As shown in Figure 5-1, the three different steps indicate accumulative deformation levels, with 80%, 135% and 150% surface expansion ratios respectively. Later experimental work will show that, during superplastic-like forming of AA5083, the sheet have been almost fully formed at 400ºC attaining 137% surface expansion.

5.1.2 Punch Design

In the hot drawing stage, the sheet is drawn into the die chamber with the assist of a moving punch. The punch design has an influence on the amount of material draw-in which can minimize expansion by getting the bumped part sheet closer to the final configuration. For comparisons of the hot drawing process, two punches with strokes of 20 and 43 mm were tested.

The punch geometry and drawing ratio are two key parameters to be determined. Since the die is a three-stepped cavity, the punch nose is therefore designed according to the die cavity geometry. The 20 mm stroke is used as the one-stepped punch to draw material sheet into the cavity within the die, as shown in Figure 5-2(a). For a greater amount of material draw-in, a longer (two-stepped) punch with 43 mm stroke is used, as illustrated in Figure 5-2(b).
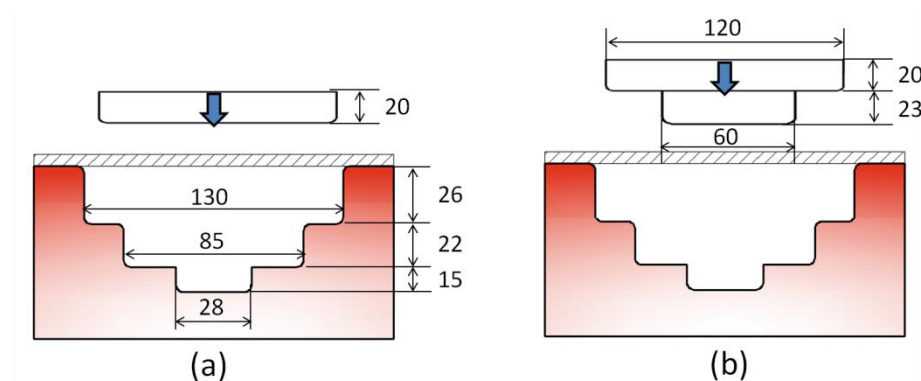
Figure 5-2 Schematics of punch geometry with two strokes of (a) 20 mm and (b) 43 mm.

Table 5-1 The effect of punch displacement on hot drawing process at 400ºC.

Punch displacement	20 mm	43 mm
Material draw-in length	10 mm	29 mm
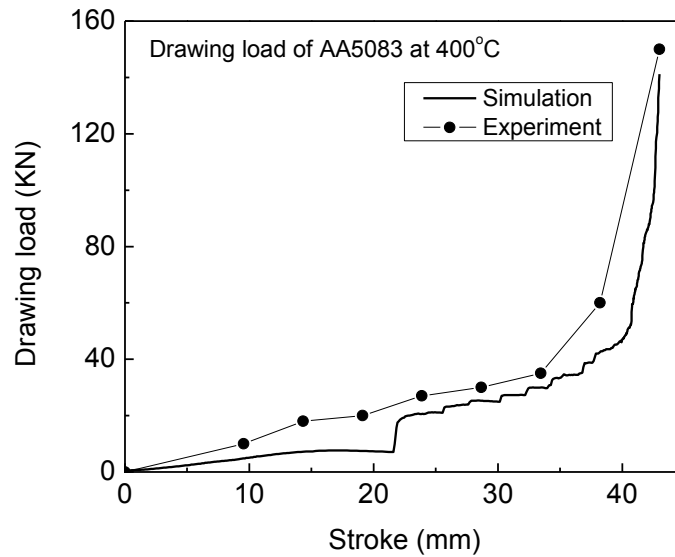
Figure 5-3 The measured and simulated loads during hot drawing of AA5083 sheet at 400 ℃.

The influence of punch displacement on material draw-in has been studied. A comparison of the measured material draw-in length at 400ºC is provided in Table 5-1. The initial sheet dimension is $200 \times 200 \times 3$ mm³. As the drawing stroke increased, the amount of material draw-in increased significantly as well.

The variations of measured punch load along with stroke were given for the hot drawing stage. As shown in Figure 5-3, a comparison of the drawing load vs. stroke with the simulation results for AA5083 at 400ºC is also plotted. It was not possible to record the punch loads continuously during hot drawing, therefore the measurement

had to be manually performed at selected displacement. The maximum simulated load value is 141 KN, while the maximum measured value is about 150 KN.

5.1.3 Conventional Superplastic Forming

The non-superplastic AA5083 sheet has been deformed by conventional superplastic forming (pure stretching or blow forming) operation without the aid of mechanical pre-forming. The gas pressure cycle was applied as same as that used in superplastic-like forming process (Figure 3-9).
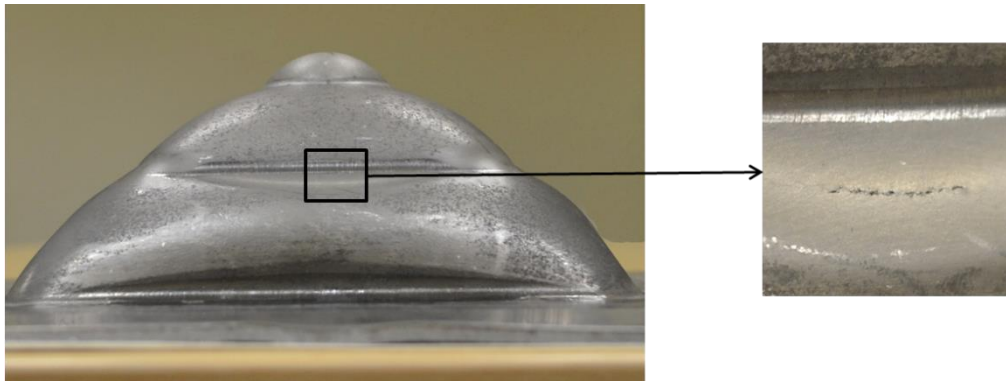
Figure 5-4 Cracking of AA5083 part during conventional superplastic forming showing a maximum percentage thinning of 65%.

Cracking occurred, as shown in Figure 5-4, the cracking is situated at the area where the material is directly in contact with the die radii. The maximum bulge height was measured to be 50 mm. The maximum percentage thinning adjacent to the cracking location is 65%. Experimental measurements reveal that the pure blow forming was not able to solely form the non-superplastic AA5083 sheet due to the limited material

plasticity and formability at 400ºC. In order to obtain a good formed part, a drawing

operation is therefore required to mechanically pre-form a portion of material into the

deformation area in advance of blow forming.

5.2   INVESTIGATION OF PROCESS PARAMETERS

5.2.1   Effect of Punch Displacement on Formability

5.2.1.1   Hot drawing with 20 mm stroke

The 20 mm stroke was used to conduct the hot drawing operation. In the initial stage, a

portion of the sheet was drawn by the punch at 400ºC, and as a result some material at

the flange flowed into the deformation area. This operation was followed by blow

forming of the bulged material into the die cavity. Material draw-in was calculated by

measuring the length of $L_0 - L_1$ at the location identified in Figure 5-5, which is

similar to the approach used by Luo *et al* [138]. The line L_0 is the width of the initial

sheet before forming, while L_1 is the distance between the middle points of the flange

area after forming.
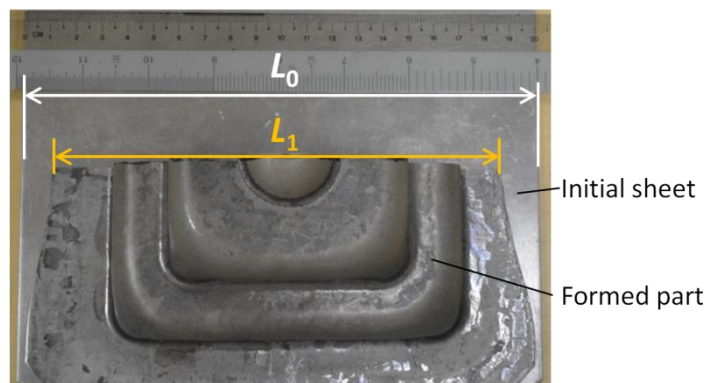
Figure 5-5 Illustration for measurement of material draw-in.

As shown in Figure 5-6(a) side view of the pre-formed component, a bumped sheet with punch displacement of 20 mm was obtained after hot drawing at 400ºC. Some material at the flange area was drawn inside the die cavity, especially at the middle edge of the blank (Figure 5-6(b)). Figure 5-6(c) shows the cross-section of the final part formed at 400ºC.
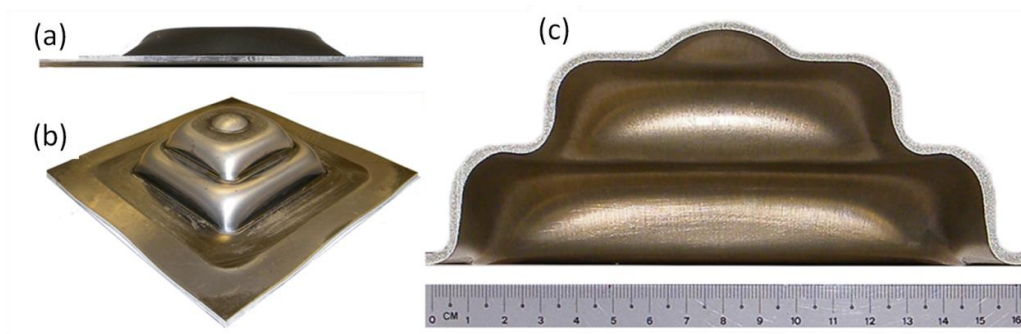
Figure 5-6 Photographs of AA5083 sheet formed at 400 ℃: (a) hot drawing part − side view, (b) formed part − top angle view and (c) cross-sectional part − side view.

Table 5-2 Material draw-in length of AA5083 at different drawing temperatures.

Temperature (ºC)	Punch displacement (mm)	Sheet size (mm²)	Material draw-in length $L_0 - L_1$ (mm)
300	20	250×250	6.4
350	20	250×250	6.4
400	20	250×250	6.9
450	20	250×250	7.0
500	20	250×250	6.2

More results at different temperatures are summarized in Table 5-2, which shows that calculating material draw-in levels by utilizing this method is proved to be effective. Furthermore, the larger amount of material draw-in is assumed to give rise to better formability and more fluidity for the subsequent operation of blow forming.

5.2.1.2   Hot drawing with 43 mm stroke

The dimension and geometry of the workpiece and punch have been redesigned for the purpose of enhancing the material draw-in level. The punch used in above work was replaced by a two-stepped punch with a stroke of 43 mm, as shown in Figure 5-2(b). The initial sheet size was also reduced into a dimension of 200×200 mm^2.

The material draw-in and bulge height are compared in Table 5-3. As the drawing displacement increases, the fractional material draw-in increases significantly from 5% to 14.5% at 400ºC.

Table 5-3 Comparisons of measured material draw-in dependent on punch displacement and drawing temperature.

Temperature (ºC)	Punch displacement (mm)	Sheet size (mm^2)	Material draw-in length $L_0 - L_1$ (mm)
400	20	200×200	10.0
	43	200×200	29.0
500	20	200×200	8.5
	43	200×200	29.6

Additionally, there is little variation found in material draw-in length when drawing is conducted using the same punch against different temperatures. It reveals that the punch displacement and geometry mainly influence the amount of material draw-in during hot drawing. The detailed size effect on hot-drawing formability will be discussed in *Section* 5.2.1.3.

5.2.1.3   Drawing limit

A considerable amount of material draw-in could be attained by using the two-stepped punch with a stroke of 43 mm, therefore, this punch are used for further investigation of hot drawing parameter, such as the optimal sheet-metal size.

In order to determine the sheet dimension with good formability for hot drawing and the subsequent gas forming, a series of drawing was performed through a parametric study to compare the amount of material draw-in and the forming state (good or ruptured). Table 5-4 summarizes the material draw-in length dependent on the initial sheet dimension.

The limiting drawing ratio (LDR) for first draw of aluminum alloys at room and high temperature are well known to be 2.1 and 3.0, respectively [77]. However, from the results of successful drawing operations, the maximum LDR values were measured to be 3.0 and 3.67 at room and high temperature (400 and 500ºC), respectively.

Friction during conventional deep drawing comes from the sheet in contact with the blank holder and die wall. The friction between the sheet and die wall introduces localized stress concentration at this area and easily results in failure of the workpiece.

Table 5-4 Material draw-in length dependent on initial sheet size. The 43 mm stroke was used.

Drawing temperature (℃)	Sheet size (mm²)	Drawing ratio	Draw-in Length (mm)	Remarks
RT	155×155	2.58	30	Good
RT	165×165	2.75	28	Good
RT	170×170	2.83	27	Good
RT	180×180	3.00	21	Good
RT	190×190	3.17	20	Ruptured
RT	200×200	3.33	20	Ruptured
400	160×160	2.67	31	Good
400	170×170	2.83	30	Good
400	180×180	3.00	30	Good
400	195×195	3.25	28	Good
400	200×200	3.33	29	Good
400	220×220	3.67	26	Good
400	230×230	3.83	Nil	Ruptured
400	250×250	4.17	Nil	Ruptured
500	165×165	2.75	31	Good
500	180×180	3.00	30	Good
500	190×190	3.17	30	Good
500	200×200	3.33	28	Good
500	210×210	3.50	29	Good
500	220×220	3.67	26	Good
500	230×230	3.83	Nil	Ruptured

In the current drawing system, because of 5 mm die clearance (i.e. no contact between the sheet and the die wall), the (frictionless) material from the bottom of the cup to the wall can carry less drawing stress leading to a higher LDR at room temperature. Furthermore, the improved drawability at elevated temperature is attributed to a differential temperature method (higher temperature at the flange and lower temperature at the sheet center), which also permits an increase in the LDR at high-temperature drawing.

Figure 5-7 shows two photographs of the ruptured AA5083 parts during drawing at room temperature (RT) and 400ºC, respectively. At room temperature (Figure 5-7(a)), the sheet was ruptured when the initial size was 200×200 mm^2. At 400ºC (Figure 5-7(b)), the sheet was ruptured when the initial size was 250×250 mm^2. As can be seen from the ruptured parts, the cup bottom tears off and is attached to the wall by only a small web. The failure encountered during RT and hot drawing is ascribable to too large drawing ratios with respect to sheet geometry.
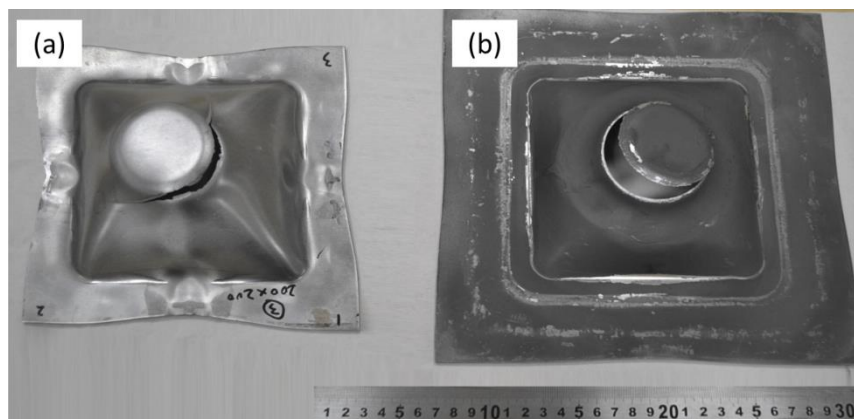
Figure 5-7 Photographs of ruptured AA5083 parts during drawing (a) at room temperature and (b) at 400ºC.

74

The cleavage of RT-drawn workpiece (Figure 5-7(a)) appears brittle features without apparent occurrence of plastic deformation on the sheet surface. Strain hardening is usually required to achieve good formability for deep drawing. Due to the poor ductility and limited achievable strains at room temperature, the drawing load transmitted from punch to the sheet can easily exceed the material strength, resulting in tearing off. However, material is not exclusively strain-hardened at high temperature since stretching can offer clear aid to deep drawing [77]. Therefore, as a comparison, plastic deformation took place at the fracture tip of the hot-drawn part (Figure 5-7(b)) showing localized thinning in the material adjacent to the punch radius.

The material draw-in as a function of initial sheet width is plotted in Figure 5-8 according to the data in Table 5-4. The scattered points represent the experimental data obtained at RT, 400 and 500ºC, while the dashed line is a linear fitting of those data for predicting the gradient of material draw-in length. The linear relationship at 400ºC can be represented by Eq. (5-1).

$$L_D = 43.5 - 0.078W_o \qquad\qquad \text{Eq. (5-1)}$$

where W_o is the initial sheet side length of a square piece (namely sheet width), and L_D is the material draw-in length.

The drawing limit zone for hot drawing AA5083 sheet is identified in Figure 5-8, from which the draw-in amounts associated with the initial sheet size are clearly visible.

It should be noted that, from the prototype die design, a sealing system was used to prevent the leakage of gas during blow forming. During the sealing stage, the sheet width after hot drawing is required to have a marginal value such that the sealing bead

could clamp the sheet flange completely. Based on the existing die assembly, the sealing bead width was preset to be 165 mm, as shown in Figure 5-9.
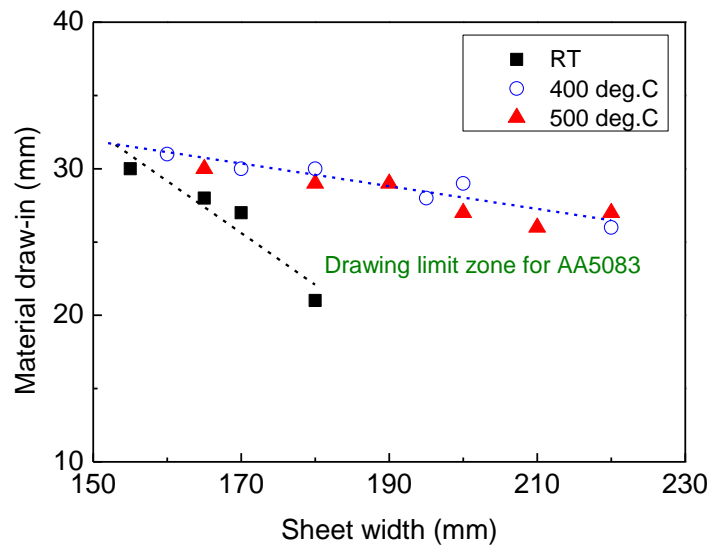
Figure 5-8 Material draw-in as a function of initial sheet width. The drawing limit zone for hot drawing is also indicated by the dashed lines.
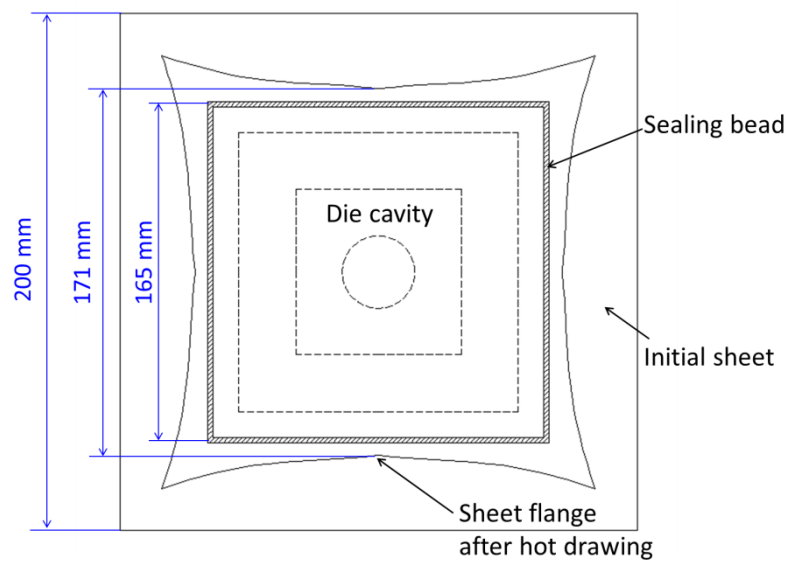
Figure 5-9 Illustration of the sealing system when forming a 200×200 mm² sheet – top view.

Eq. (5-2) reveals the relationships of the minimum required flange width, initial sheet width and material draw-in length.

$$W_f = W_o - L_D > 165 \text{ mm} \qquad \text{Eq. (5-2)}$$

where W_f is the minimum required flange width.

In the case of hot drawing, L_D value predicted from Eq. (5-1) is used in Eq. (5-2), and the initial sheet width could be obtained as

$$W_o > 193 \text{ mm} \qquad \text{Eq. (5-3)}$$

Additional, sheet metal allowance is required in order to effectively avoid the assembly error. Therefore, based on the existing die set, the initial sheet size was determined to be 200×200 mm^2 for a balance between the maximum amount of material draw-in and the best sealing condition.

5.2.2   Effect of Forming Temperature on Formability

5.2.2.1   Bulge height

The level of bulging into the three-stepped die cavity after mechanical pre-forming was obtained from a series of experiments conducted within the temperature range from 300ºC to 500ºC. After the introduction of the forming gas, bulging was present and the sheet formed corresponded to the inner die shape in 8 min. Figure 5-10 shows the bulge height profiles of formed parts against the different forming temperatures. The prototype die depth is 63 mm. The bulge height reaches as high as 58 mm at 400ºC, which is nearly 92% of the full height.

In comparison with the results formed at various temperatures, there is more than 30% increase (38 to 58 mm) in bulge height as the temperature increases from 300 to 400ºC, while the increase is less than 10% (57 to 62.4 mm) from 400 to 500ºC. As a result, the increase of bulge height in the temperature range of 300 to 400ºC is much higher than that in the 400 to 500ºC range. In addition, the changes of the microstructural features such as grain growth, cavitation and dynamic recrystallization have also been introduced in the formed component due to a higher forming temperature. The microstructure observations are presented in *Section* 5.4.
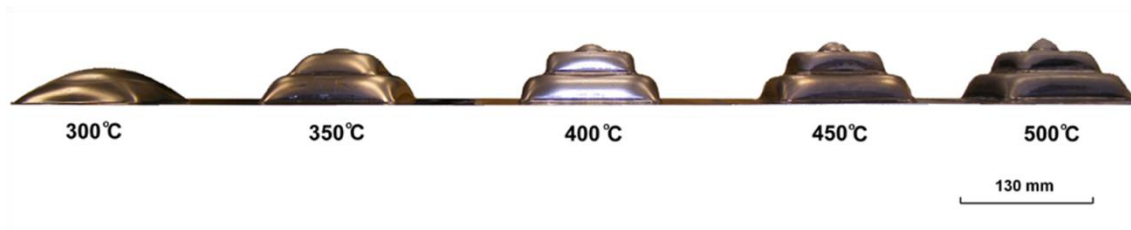
Figure 5-10 Bulge height profiles of formed AA5083 parts at different temperatures.
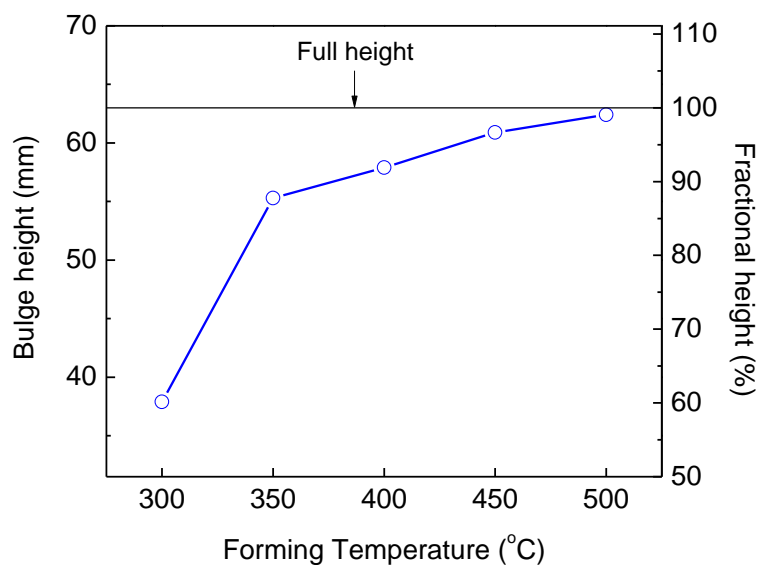
Figure 5-11 Bulge height as a function of forming temperature.

5.2.2.2   Surface expansion

In order to investigate how much percentage completion that the formed part reaches, surface expansion ratios at different temperatures were compared. The surface expansion ratio is defined as the percentage increase in surface area that occurs during superplastic-like forming. The maximum surface expansion ratio for the prototype die configuration is 150% representing a net-shape formed part.

The forming temperature would not be as high as that for superplastic forming, because the expansion ratio does not depend solely on the formability of the material as more material is introduced into the forming area during the hot drawing stage. Table 5-5 lists the surface expansions at temperature ranging from 300 to 500ºC. The maximum gas pressure applied during gas forming was 4.2 MPa.

Table 5-5 Surface expansion as a function of forming temperature.

Forming temperature (℃)	Surface expansion (%)
300	60
350	106
400	137
450	140
500	145

It can be concluded that the surface expansion increases with increasing temperature, indicating the formability influenced by the forming temperature as well. At 500ºC, the

surface expansion reaches 145%. However, it should be mentioned that the sheet was ruptured when the forming pressure reached 2.7 MPa at 500ºC. The cracking is located on the dome center area, as shown in Figure 5-12. One of the reasons to account for the cracking is the limited plasticity of AA5083 (*Section* 4.1.3) and the occurrence of cavitation (*Section* 4.2.2) during high-temperature deformation.
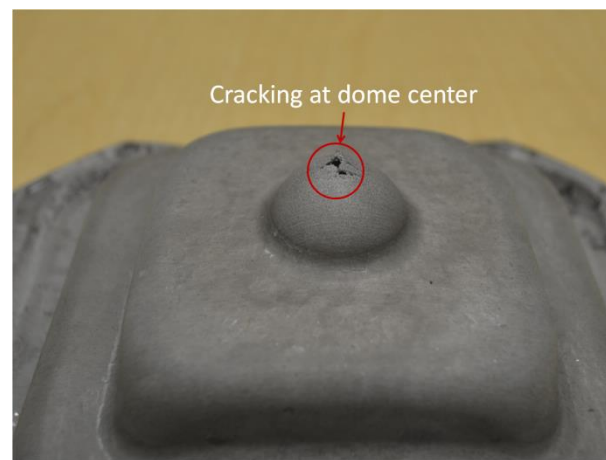
Figure 5-12 Cracking of the AA5083 part during superplastic-like forming at 500 ℃.

5.3 THICKNESS DISTRIBUTIONS

5.3.1 Non-Isothermal Heating System

During the initial stage of superplastic-like forming, the temperature was maintained at the lowest possible level. Only the temperature in some specific zones, such as corner radii, will be high in order to ensure that the material in that particular area has enough ductility to form at the designed corner radius. This technique is referred to as non-isothermal heating system. Figure 5-13 illustrates the selective heating areas with a

higher local temperature, as compared to the other areas with a global (furnace) temperature of 400 ℃.

AA5083 sheet was initially mechanical pre-formed at 400 ℃ during hot drawing. Cartridge heaters were used to heat the die entry radii to a temperature high than 400 ℃. As shown in Figure 5-13, the temperatures at different areas are monitored by *K* type thermocouples showing that the temperatures inside the die chamber are not uniformly distributed. The temperature variations may be due to the differences in heat conduction.
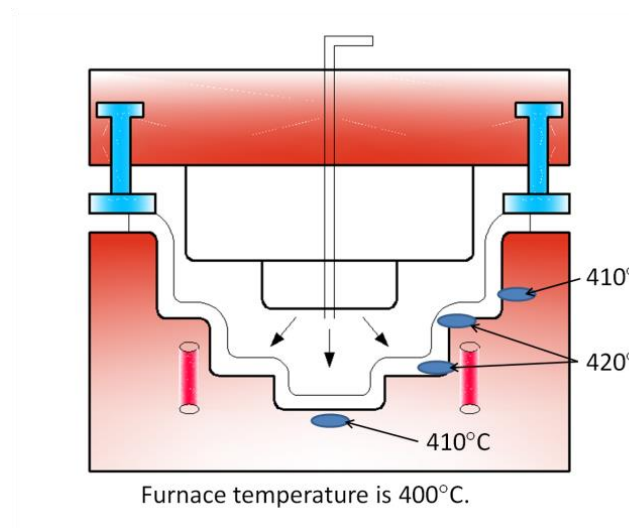
Figure 5-13 Temperature distributions for the non-isothermal heating system.

The comparisons of bulge height, thickness and surface expansion are summarized in Table 5-6. The bulge height was mainly affected by the material ductility and the gas pressure cycle during gas blow forming. Accordingly, the final bulge heights show a little variation (< 2%). The increased bulge height under non-isothermal conditions

may be due to a better flowability arising from the localized higher temperature. The thickness variation ($< 6\%$) reveals that the higher bulge height leads to a thinner thickness.

However, the surface expansion is influenced significantly. The expansion ratio does not depend solely on the formability of the material, as more material is introduced in the forming area during the drawing stage. The reduced global temperature and the increased local temperature have ensured the sheet being successfully formed with a greater percentage completion.

Table 5-6 Bulge heights and thinning under different heating conditions.

Global temperature 400 ℃	Punch displacement (mm)	Bulge height (mm)	Minimum thickness (mm)	Surface expansion (%)
Isothermal	20	57	1.5	121
Non-Isothermal	20	58	1.4	130
Isothermal	43	57	1.9	130
Non-isothermal	43	58	1.8	137

5.3.2   Thickness Distributions at 400ºC

5.3.2.1   Non-isothermal forming using 20 mm stroke

The sheet was almost fully formed without any failure on the surface by utilizing the superplastic-like forming process at 400ºC. In order to measure the thickness

distributions, the formed part was cut along two sections, as shown in Figure 5-14. From Figure 5-14(b) and (c), a thickness gauge was used to measure the thickness along the two sections from the dome center to the edge; each section was named from locations #1 to #12. In both of the sections, locations #3, #7 and #11 represent the inward corners, while locations #5 and #9 represent the outward corners.
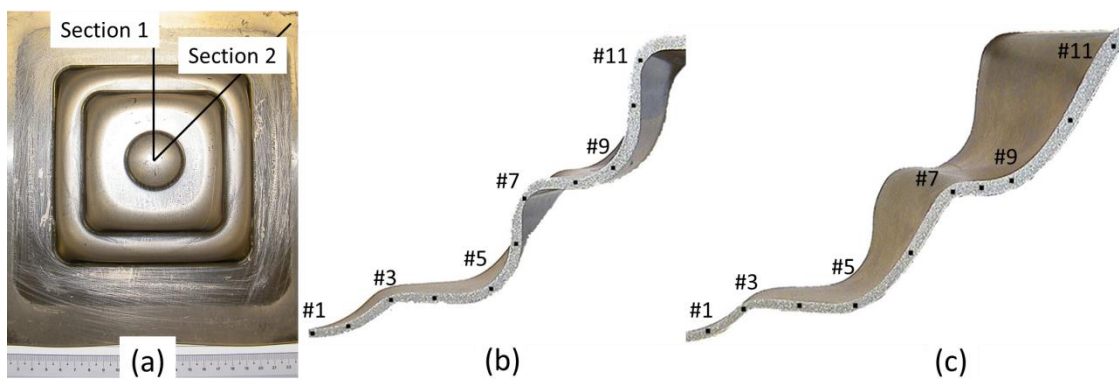
Figure 5-14 Illustration for measurement of thickness distributions of the formed part at 400ºC: (a) schematic sections, (b) section 1 and (c) section 2. The 20 mm stroke was used.

The formed component shows no cracking, but exhibits localized thickness reduction near the part corners. Figure 5-15 plots the thickness distributions along the two sections, in which the localized thinning locations are easily observed.

In section 1, the relatively higher variations in thicknesses occurred in the corner positions, where the sheet deformed largely inward from its surface to contact the die entry radius. This result is similar to the work of Kim *et al* [98], which was focused on magnesium alloys. However, the minimum thickness formed at the inward corner of

location #7. The maximum thickness reduction in this section was 54%. The result was influenced by the forming sequence, in which the sheet firstly came into contact with the die surface at the radii during free bulging. Material within this area was then locked against the tool by friction and gas pressure [41], as a result necking occurred due to the large strain developed.
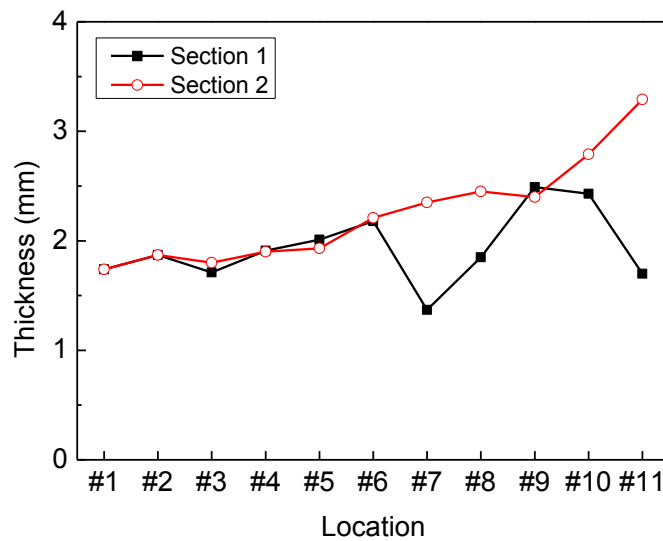
Figure 5-15 Thickness distributions after forming at 400 ℃. The 20 mm stroke was used.

In section 2, the thickness distributes relatively evenly compared with that in section 1 except at location #11. There is a thickening (with thickness of 3.29 mm) at location #11, which is due to the occurrence of compressive stress located at the corner radii in the die during bulging. The minimum thickness was formed at the dome center (location #1), and the maximum thinning in this section was 42%. Comparing both the thickness distributions along the two sections, there was less thickness reduction in the inward corners (locations #3, #7 and #11) in section 2.

5.3.2.2   Non-isothermal forming using 43 mm stroke

The thickness is more uniformly distributed when using the 43 mm stroke, as compared to the thickness distributions in Figure 5-15. No sharp reduction is found from the thickness profiles, as shown in Figure 5-16. The thickness at location #4 remains the same value of 1.8 mm as it was measured from Figure 5-15, while the thickness at location #7 increases from 1.4 to 2.1 mm after utilizing the 43 mm stroke. Furthermore, the thicknesses at other locations are also thicker than before.
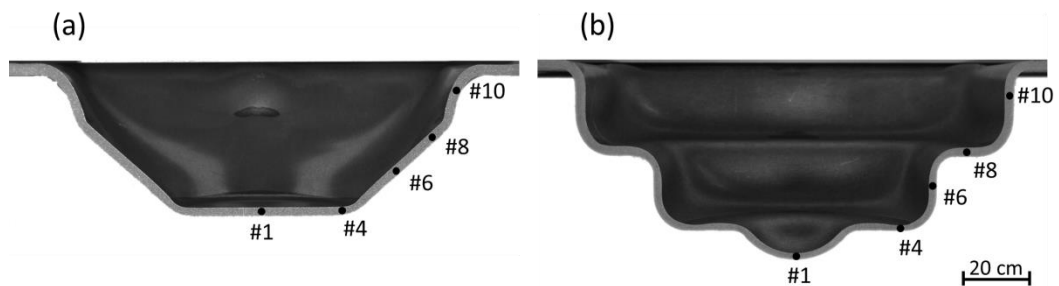
Figure 5-16 Cross-sections of the formed AA5083 parts at 400 ℃: (a) hot drawing and (b) gas forming. The 43 mm stroke was used.
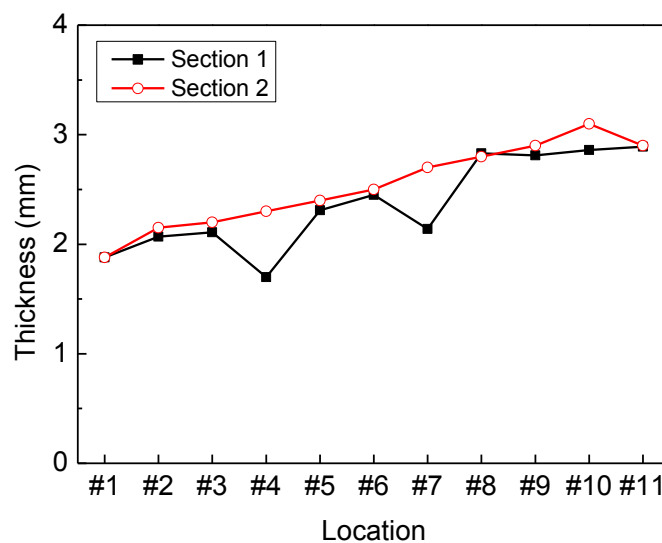
Figure 5-17 Thickness distributions after forming at 400 ℃. The 43 mm stroke was used.

It has been found that, after adopting a longer stoke, the material draw-in length would increase, as can be seen from Table 5-3. The great amount of material draw-in could facilitate the use of non-superplastic material for blow forming. Subsequently, the high pressure gas was flown inside to form the designed shape or geometry. With the larger punch displacement, more material has been introduced into the deforming sections of the sheet, therefore leading to less localized thinning at the corners.

5.3.3   Thickness Distributions at 500ºC

5.3.3.1   Non-isothermal forming using 20 mm stroke

In this work, the furnace was heated to a constant temperature of 500ºC, and the die radii were selectively heated to 520ºC. The local temperature cannot reach a higher temperature due to the heat dissipation in the non-isothermal heating system.
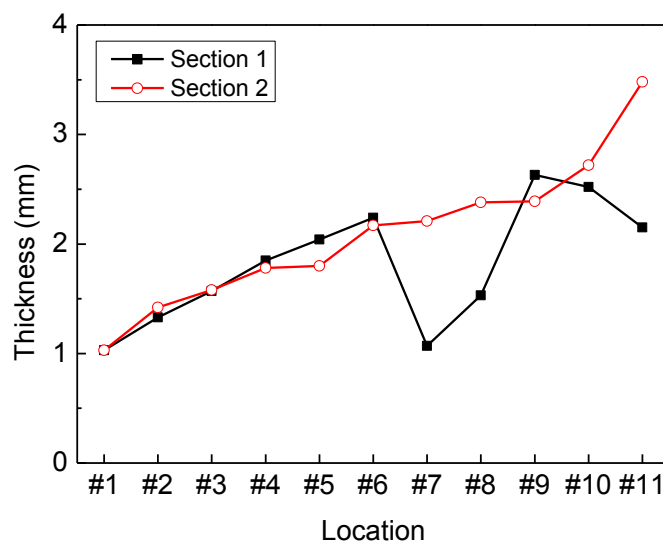
Figure 5-18 Thickness distributions after forming at 500 ℃. The 20 mm stroke was used.

The thickness distributions at 500ºC along two sections are compared in Figure 5-18. Thickness values measured from section 1 show two sharp reductions that are located at the same locations (#7 and #11) at 500ºC as those at 400ºC (see Figure 5-15).

The maximum percentage thinning at location #7 is almost 64%. The thickness gradients correlated to temperature changes during forming reveal that the increased temperature would cause softening and result in more microstructural defects in the deformation area, especially at locations #1 and #7.

5.3.3.2   Non-isothermal forming using 43 mm stroke

The thickness profiles measured from the formed AA5083 part when using the 43 mm stroke are plotted in Figure 5-19. In section 1, similar to the plots at 400ºC in Figure 5-17, there are also two locations exhibiting localized thinning, in which the minimum thickness in this section was measured to be 1.5 mm at 500ºC. Stretching of the sheet resulting from the moving punch during hot drawing and friction between the sheet and hot die surface during gas forming are two main reasons that account for localized thinning at the two locations.

In section 2, the minimum thickness is formed at the dome center (location #1), and the maximum percentage thinning is 47%. Thought the sheet is ruptured by cavitation at location #1, the thickness in section 2 appears uniform and not localized. Limited plasticity resulting in less ductility is one of the reasons that is responsible for the cracking. In addition, because of the more observed cavitation at the higher temperature, the material could easily rupture due to the initiation and interlinking of inner cavities. Table 5-7 summarizes the maximum percentage thinning occurred at different temperatures.
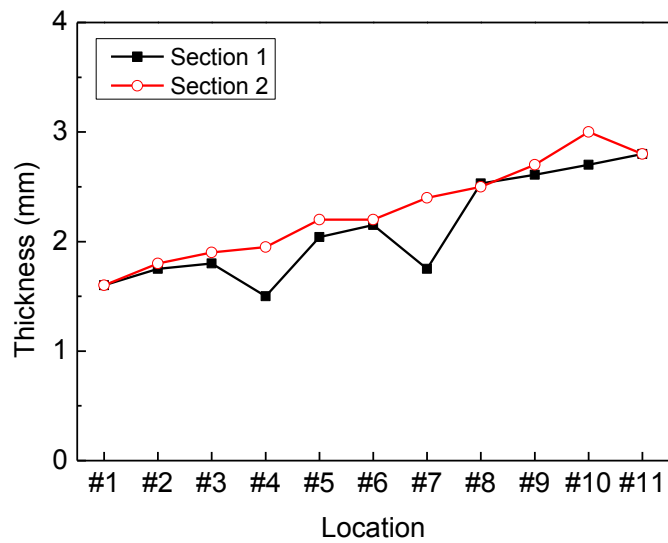
Figure 5-19 Thickness distributions after forming at 500 ℃. The 43 mm stroke was used.

Table 5-7 Summary of the results for AA5083 parts formed under non-isothermal conditions.

Forming temperature (ºC)	Punch displacement (mm)	Section 1		Section 2	
		Max % thinning	Location	Max % thinning	Location
400	20	54%	#7	42%	#1
	43	40%	#4	37%	#1
500	20	64%	#7	64%	#1
	43	50%	#4	46%	#1

5.4 MICROSTRUCTURES

Only the parts formed using the 20 mm stroke were used for microstructure observations via optical microscope. For the part formed by the 43 mm stroke at 400ºC, it is further examined by EBSD which will be presented in *Chapter* 6.

5.4.1 Microstructures of the Formed Part at 400ºC

Microstructures obtained after polishing and etching along section 1 are shown in Figure 5-20. There are evidences showing some grain growth and cavitation after forming from the microstructures of locations #3, #7 and #11. Every corner was divided into 3 zones for detailed observations, including interior, middle and exterior, as the schematic shown in Figure 5-20.

The grains appear to be much coarser, especially in the middle zones. Because the grains can stretch much more in the longitudinal direction under high pressure, grains with large aspect ratio were also obtained. The grain aspect ratio at this section increased as a result of large strain and thinning, especially along the middle zones. At location #11, much larger grains were found, which was due to the long contact time between the sheet and the hot die.

Cavitation is an important phenomenon when the aluminum is subjected to high stress and high temperature. Failure during deformation occurs as a result of the nucleation, growth and coalescent of internal cavities [41]. The maximum thickness reduction along this section was found at location #7, where the microstructure changes were also coinciding with the thinning results. More cavitation took place due to the high deformation in areas where cavitation had reached the highest level. With increasing

strain, the cavities grew along the grain boundary and coalesced with each other. Furthermore, dynamic recrystallization as a result of large deformation and high forming temperature was observed by comparing the microstructure changes.
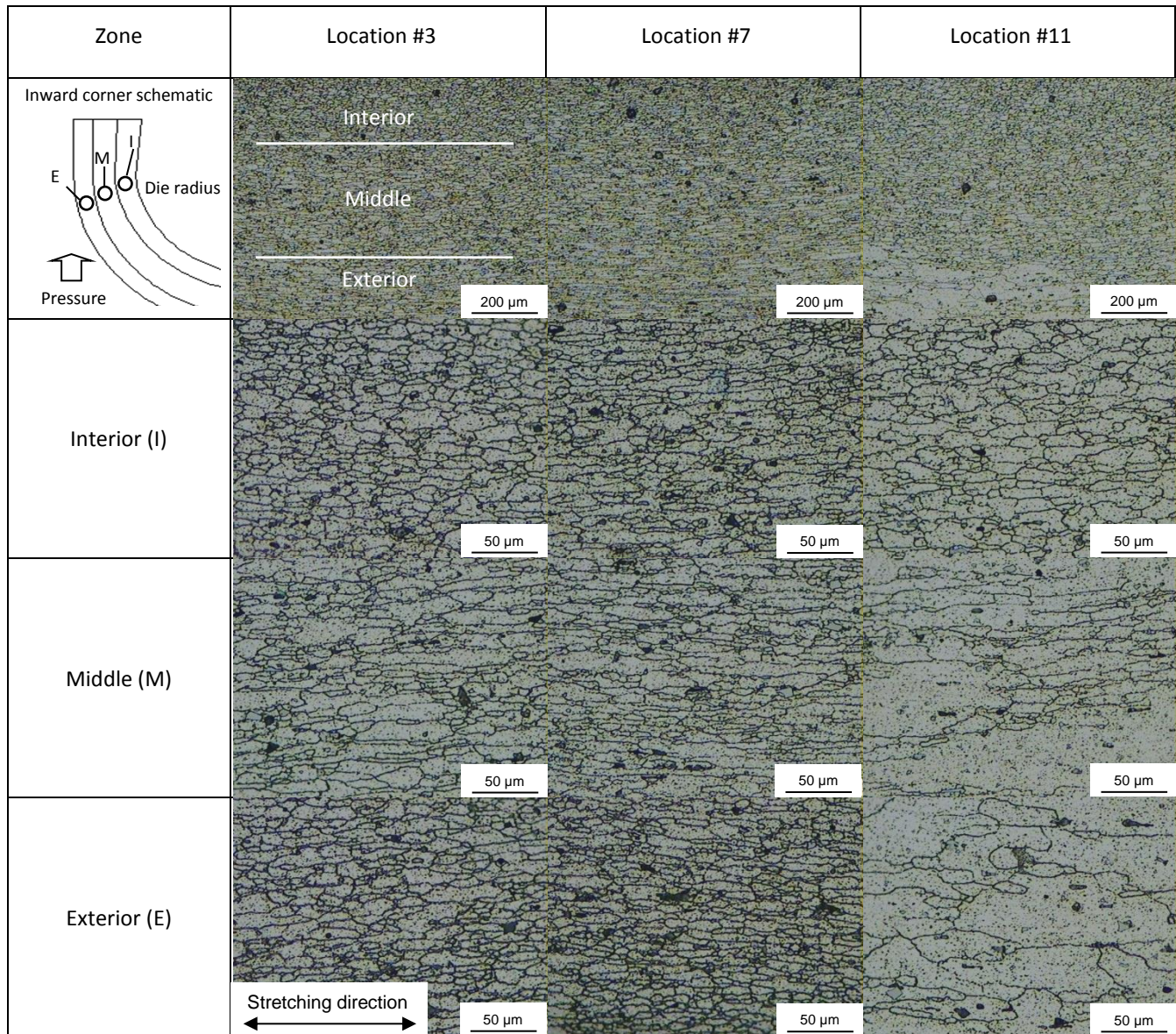
Figure 5-20 Schematic and microstructures of formed AA5083 at location #3, #7 and #11 along section 1 at 400 ℃.

5.4.2   Microstructures of the Formed Part at 500ºC

As compared to the formed part at 400ºC, the changes in the microstructural features, such as grain size and cavitation after forming at 500ºC, were monitored in order to obtain comparison results. Figure 5-21 represents the microstructures observed at 500ºC corresponding to the same zones indicated in Figure 5-20.
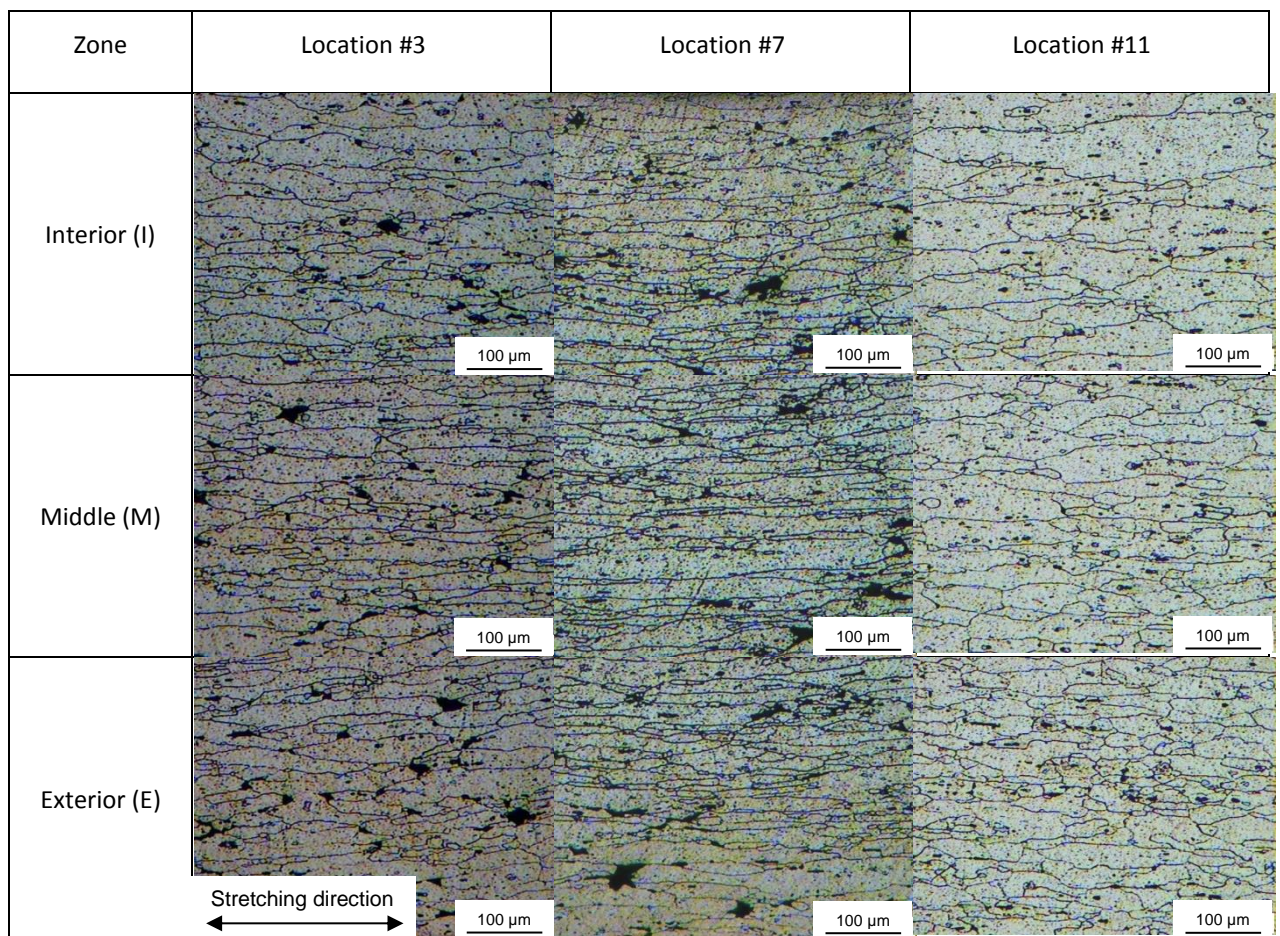
Figure 5-21 Microstructures of formed AA5083 at location #3, #7 and #11 along section 1 at 500 ºC.

The grains at 500ºC grow much coarser than they were at 400ºC. Because the grains were stretched along the stretching direction by the imposed pressure, the elongated

grains with large aspect ratios are found. From the thickness gradient along this section, the maximum thickness reduction is found at location #7. The grain aspect ratio at this location increases as a result of large strain and great thinning. With increasing strain, the cavities grow along the grain boundary and coalesce with each other. More cavities are also clearly visible from the microstructure at this location.

However, little cavitation could be found at location #11, which is ascribed to the small sheet thinning during deformation. Large grown grains at this location also indicates the effect of high temperature and long contact time between the sheet and hot die.

5.5   THINNING CHARACTERISTICS

The process design and microstructure observations have demonstrated that AA5083 sheets were successfully formed by the combination of hot drawing and gas forming. Further investigations on the experimental components, i.e. material draw-in, bulge height and thickness distributions, have determined the optimal process parameters. The non-superplastic grade AA5083 sheets can be pre-formed with good formability by a stroke of 43 mm and then blow-formed at a target forming strain rate of 2×10^{-3} s^{-1} at 400ºC. The sheet thinning characteristics will, therefore, mainly focus on the final parts formed under these conditions.

For the multi-stepped die, the three cavities named as top, mid and bottom cavity represent the accumulative surface expansion ratios of 80%, 135% and 150%, respectively. As shown in Figure 5-22, the top and mid cavities are rectangular parts; the bottom cavity is regarded as a spherical dome because the sheet material is freely bulged into this cavity during the last stage of gas forming.
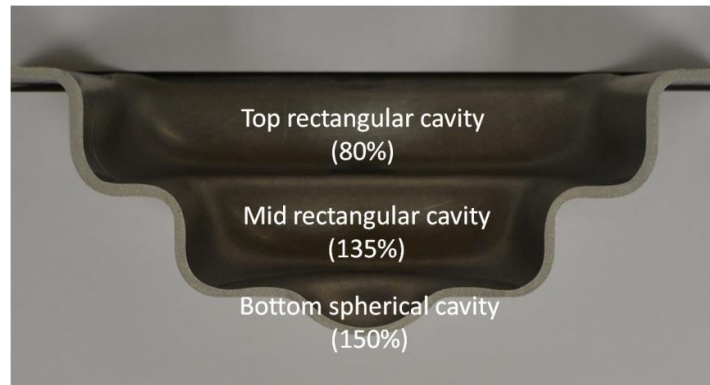
Figure 5-22 Schematic of the three cavities and the accumulative surface expansion ratios.

The factors that contribute to the thinning characteristics in rectangular parts are the local stress state and the geometric inhomogeneity. The difference in the local stress leads to strain rate gradients, and the strain rate gradients develop directly into thickness gradients [137]. The geometric inhomogeneity, as well as the rectangular parts, is studied in this section by experimental measurements.
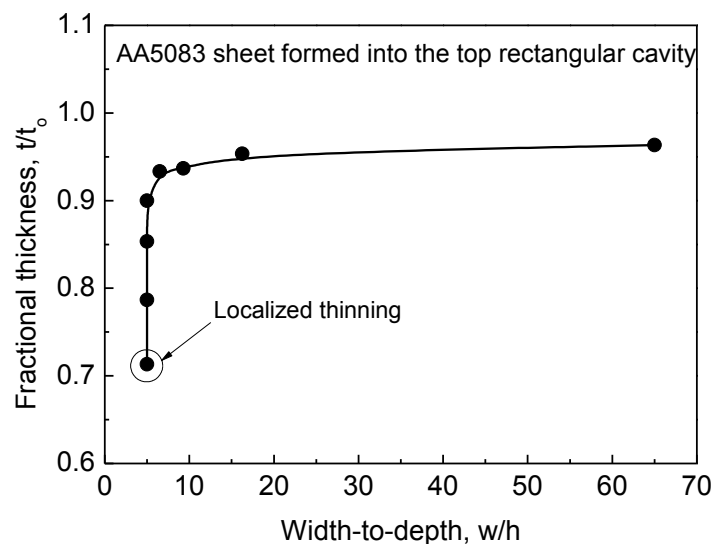
Figure 5-23 Measured fractional thicknesses as a function of the width-to-depth (w/h) ratio for AA5083 part of the top rectangular cross-section.

Figures 5-23 and 5-24 show the thickness variations corresponding to various width-to-depth ratios of the top rectangular and mid rectangular cavities. t is the measured thickness along the cross-section. t_0 is the initial thickness of AA5083 sheet, which is 3 mm in this work. It is revealed from the figures that the mid rectangular cavity produced a greater amount of localized thinning (maximum percentage thinning of 40%), as compared to the top rectangular cavity (percentage thinning of 29%).
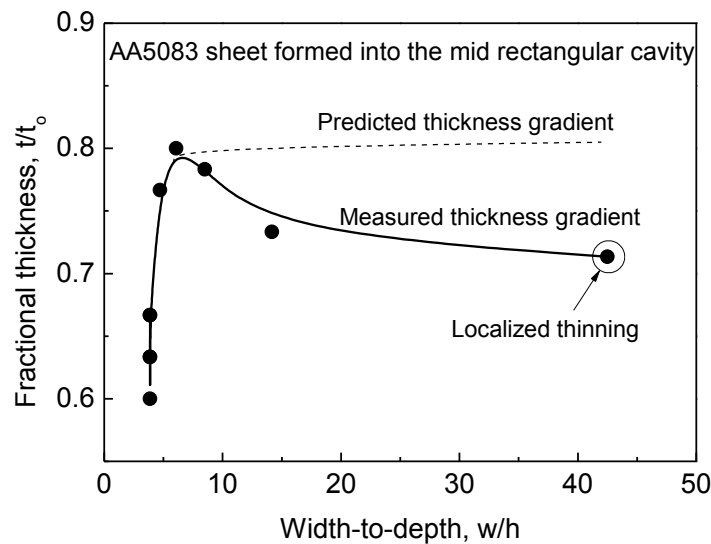
Figure 5-24 Measured fractional thicknesses as a function of the width-to-depth (w/h) ratio for AA5083 part of the mid rectangular cross-section.

In Figure 5-24, the thinning strain when the width-to-depth ratio is higher than 10 is predicted to be maintained at a constant value. However, the measured values are decreasing with increasing w/h ratios. This is ascribed to that the material adjacent to the edge of mid cavity here also acts as a part of pre-formed material in the top rectangular cavity (Figure 5-23). The pre-formed sheet has undergone thinning before

it makes contact with the die surface at the sidewall. Therefore, the decreasing thickness gradient is obtained. As can be distinguished in the two figures, the circled points indicate the same location that has the same localized thinning value.

The material used in the forming process is the non-superplastic grade AA5083 with small strain rate sensitivity index (m value). In such case, the effect of m value on the variations of thinning will not be included. It is assumed that the stress gradient in a forming dome causes a more rapid thinning rate at the pole [137]. The stress contributions to thickness variations during forming will be discussed in *Chapter* 7.
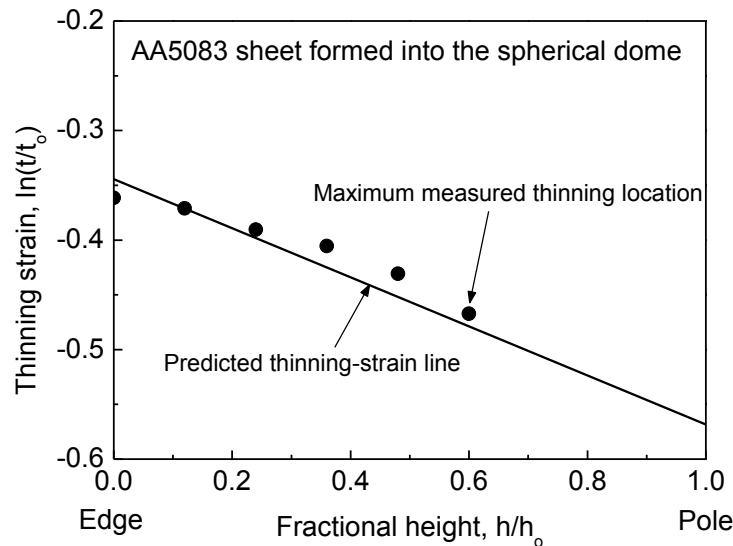
Figure 5-25 Thickness strain as a function of the fractional height for AA5083 part of the dome-shaped cross-section.

Figure 5-25 plots the calculated thickness strain as a function of the fractional height (h/h_0), where h is the height on the dome at which the thickness is measured and h_0 is the full height of the spherical dome. As the straight line shown in Figure 5-25, it

indicates the maximum thinning occurring at the pole, where $h/h_0 = 1$. A maximum

percentage thinning is predicted to be 44% when the material is fully flowing into the

bottom spherical cavity.

However, due to the limitations of the forming press, the maximum imposed gas

pressure is limited to be 4.2 MPa, which is not high enough to deform the material

fully into the multi-stepped cavity. Therefore, the maximum percentage thinning in this

section is experimentally measured to be 37%, as the location indicated in Figure 5-25.

5.6 SUMMARY

Non-superplastic grade AA5083 sheets, with a peak elongation of 80% based on

tensile test at 400ºC, was used in this work for superplastic-like forming. Compared

with the conventional SPF of superplastic materials, the disadvantages of slow forming

rate (usually more than 30 min) and high temperature requirements (mostly higher than

500ºC) were overcome by conducting a mechanical pre-forming in advance of the

blow forming process. Experimental tests have shown the feasibility of using the

combined process to fabricate the non-superplastic sheet into a complex-shaped (multi-

stepped) part at a relatively lower temperature. The following results have been

summarized.

1. The influences of process parameters, i.e. punch geometry and forming
   temperature were investigated. The longer punch displacement introduced larger
   amount of material draw-in, and produced a better formed part with less thickness
   variations. The maximum forming bulge height increased with increasing

temperature. The drawing limit zone obtained experimentally is able to determine the optimal initial sheet size for hot drawing.

2. By using the non-isothermal heating system, the higher local temperature has ensured the sheet being successfully formed with a greater percentage completion, as compared to the isothermal conditions.

3. The optimal forming temperature for AA5083 is 400ºC, at which it takes only 8 min for the gas blow forming, and the process produced an almost fully formed part with 92% fractional height and 137% surface expansion. The forming strain rate during gas blow forming was maintained at 2×10^{-3} s^{-1} for a good material formability at 400ºC.

4. The minimum thickness was formed near the outward corners; and the maximum percentage thinning of the final part is 40%. The geometric inhomogeneity is used to discuss the thinning characteristics. Large stretching strains in the forming sheet as a result of gas pressure and friction between the locked material and die surface are believed to account for the localized thinning, especially for the part outward corners at location #4.

5. Microstructure changes were found during forming, e.g. grain growth and cavitation, as a result of the large level of deformation. More cavitation and grown grains were observed during forming of AA5083 at 500ºC.

CHAPTER 6   MICROSTRUCTURAL DEVELOPMENT

DURING FORMING OF AA5083

AA5083 parts with near-net-shape and minimized sheet thinning were fabricated at 400ºC. Fairly uniform microstructure can be achieved by this forming process. There was little understanding of microstructure evolution and texture transformation during forming, especially for the hot-drawing influence on microstructural development. To investigate the microstructural information, the annealed and hot deformed samples were characterized using electron backscatter diffraction (EBSD) technique.

6.1   SAMPLES FOR EBSD MAPPING

Figure 6-1 shows the cross-sections of samples taken from the formed workpieces at the end of two forming stages, i.e. hot drawing and gas forming. The different specimen locations chosen for EBSD mapping were labeled by numbers, and the location numbers at both of the cross-sections correspond with each other.

In this study, the specimen locations to be focused on are mainly located at #1, #4, #6, #8 and #10, as indicated in Figure 6-1. It should be noted that since the process has adopted a non-isothermal heating method during gas forming (Figure 6-1(b)), the temperature (420ºC) at location #4, # 5 and # 6 is higher than that (400ºC) in the other zones of the forming sheet.
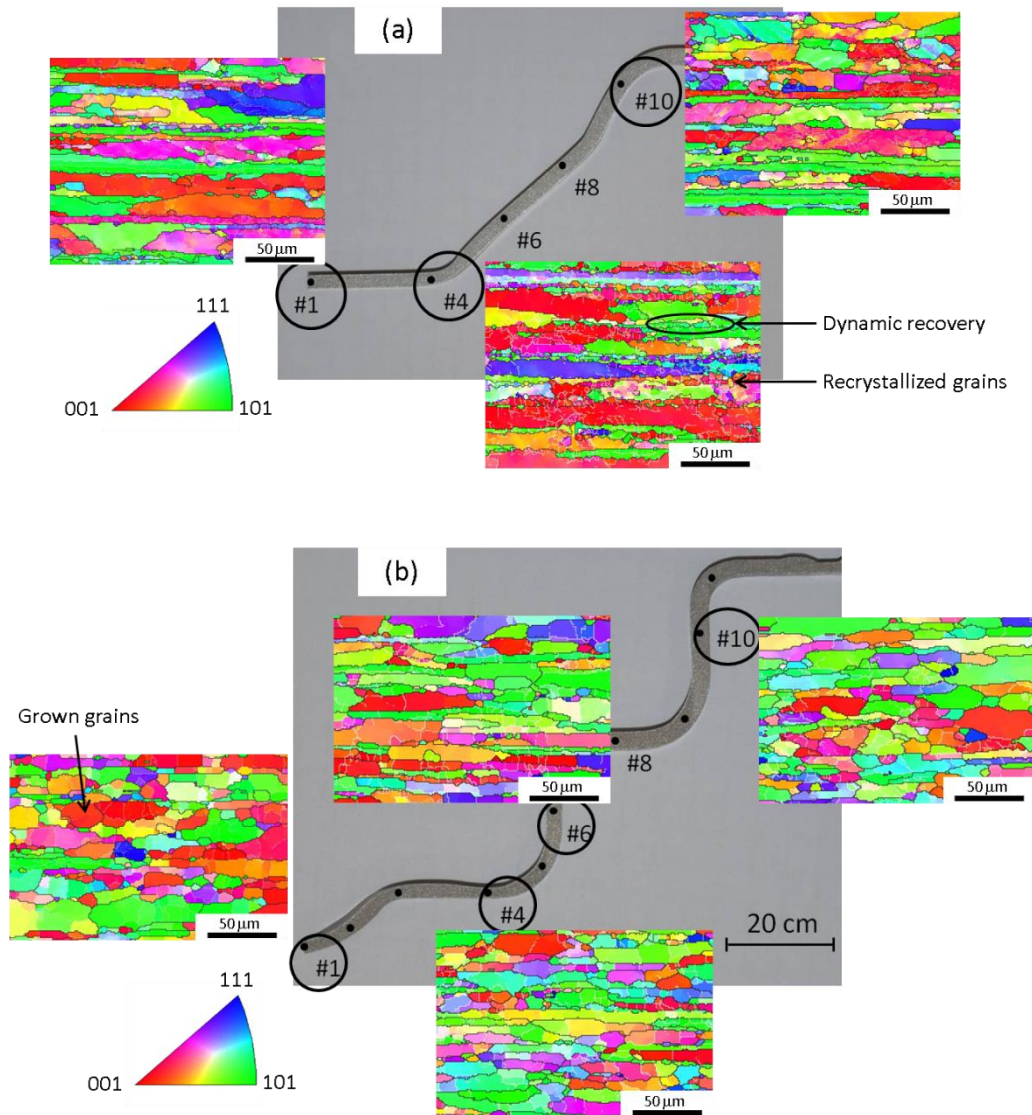
Figure 6-1 Cross-sections of formed AA5083 parts for EBSD mapping (a) after hot drawing and (b) after gas forming.

Thickness distributions of the specimens after hot drawing and gas forming were plotted according to the location, as shown in Figure 6-2. The minimum thickness of 1.8 mm after superplastic-like forming was found at location #4, in which the corresponding percentage thinning was 40%.

After observing all the microstructural features (grain structures and textures) over the entire formed part, it was found that the microstructure, misorientation and texture exhibited similarity at those selected locations (#1, #4, #6, #8 and #10 in Figure 6-1). The location #4, where maximum thinning occurred, was therefore chosen for investigation of microstructural characteristics, deformation mechanism and post-forming properties.
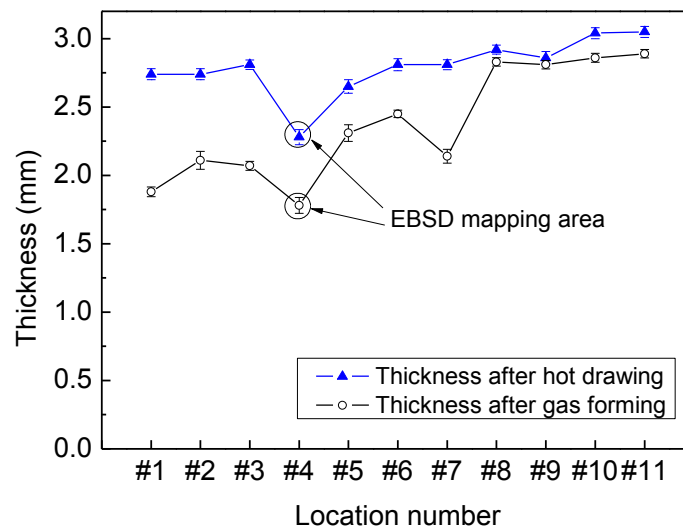
Figure 6-2 Thickness gradients measured at different locations corresponding to EBSD mapping.

6.2　MICROSTRUCTURE EVOLUTION

6.2.1　Annealed Microstructure

The typical microstructure of commercial AA5083-O (annealed) is shown using an IPF map in Figure 6-3(a). It is clear that there are many sub-structures with a high density of low angle grain boundaries (LAGBs, the white lines) assembling together to form

cells. These cells with dimensions of several micrometers were recognized as subgrain boundaries. The mean grain size of parent material is 12.9 μm, and the average aspect ratio of the grains is 2.3. All the grains with red <100>, green <101> and blue <111> orientations are near randomly distributed in annealed condition.
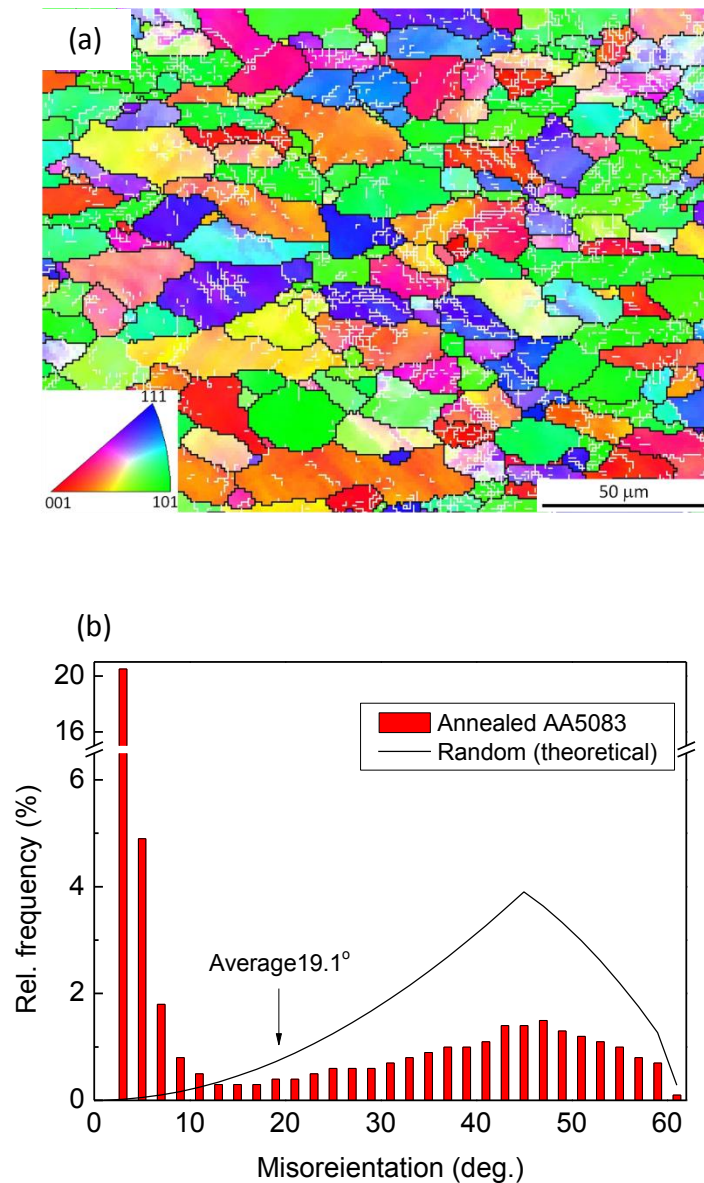
Figure 6-3 (a) EBSD map of annealed AA5083 showing a mean grain size of 12.9 μm and (b) grain boundary misorientation distribution.

Figure 6-3(b) provides the frequency distribution of boundary misorientation angles for the annealed specimen. The theoretical distribution of a random set of orientations for aluminum was also displayed by a black solid curve (Mackenzie plot) [202]. It is obvious that there is a decreasing fraction of LAGBs in the range of $2 - 15°$ and a low peak value of HAGBs around 45°. The average misorientation angle was determined to be 19.1°. The fraction of LAGBs is 60%, indicating those subgrain boundaries were occupying most proportion of the boundary structure.

6.2.2   Microstructure after Hot Drawing

The microstructure after hot drawing is shown in Figure 6-4(a). When the sheet was hot drawn into the die cavity during hot drawing, it was assumed to be extensively dislocation-based (high strain-rate hardening) deformation and consequently the grains were elongated during this stage. Many grains were elongated to reach aspect ratios of 2 and up to 12. The average aspect ratio was determined to be 5.3. By comparisons of the sub-structure (white lines) in Figures 6-3(a) and 6-4(a), it can be seen that the subgrain boundaries re-arranged (or grew) into brick-shape during hot drawing. Subgrain rotation is one of the mechanisms accounting for coarsening of the subgrains [150]. It also explains the occurrence of some high-angle grains within the elongated grain. The brick-shaped subgrains and grains influenced rapidly the misorientation angle distribution. As compared to the annealed specimen (Figure 6-3(b)), a decreased frequency of the LAGBs in the range of $< 5°$ occurred with an obvious increase of HAGBs in the range of $> 50°$ (Figure 6-4(b)). This trend is consistent with the observation that subgrain rotation and coalescence in the low-strain stage lead to strain hardening [146].
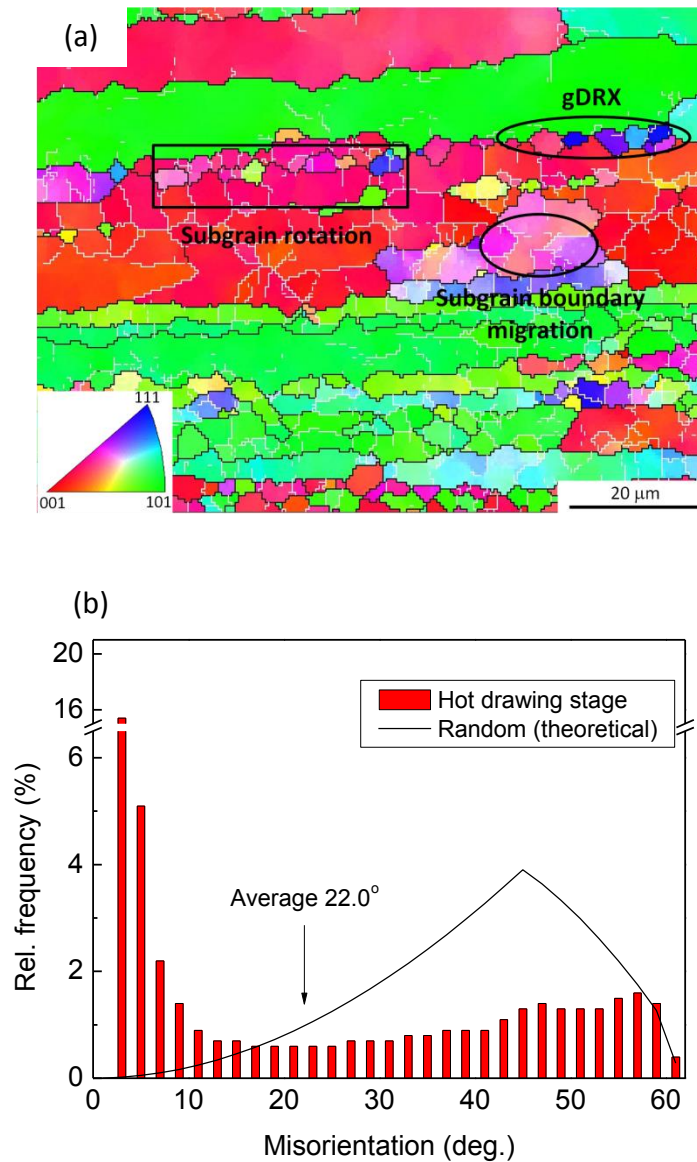
Figure 6-4 (a) EBSD map of AA5083 at the end of hot drawing showing typical dynamic recrystallization and subgrain structures and (b) grain boundary misorientation distribution.

Additionally, the proportion of boundaries in the mid-misorientation range of $15 - 50°$ increased as compared to that of annealed AA5083. The average misorientation angle after hot drawing, see Figure 6-4(b), increased from $19.1°$ to $22°$ and the fraction of HAGBs increased from 40% to 47%. Therefore, another deformation mechanism involves subgrain boundary migration [203]. Subgrain boundaries migration gradually

resulted in coarsening of the subgrains and grains, as evidenced in Figure 6-4(a). There still exist many subgrain boundaries (white lines) within the large grains, which have not completely migrated into high-angle grain boundaries (black lines) during hot drawing.

A small amount of HAGB serrations are visible adjacent to the elongated grains after hot drawing, exhibiting typical geometric dynamic recrystallization (gDRX) [204]. These serrations on neighboring structures met resulting in pinching off the elongated grains [205], and consequently contributed to the increase of grain boundary misorientation angle as well. These recrystallized grains were also identified by measuring the internal grain misorientation below 3 °[206]. The mean grain diameter of the hot drawn specimen was 9.4 μm, which is smaller than that of parent material (12.9 μm). The occurrence of the fine recrystallized grains and re-arrangement (rotation and migration) of subgrain boundaries seem to be the reasons to account for the decrease in mean grain size.

6.2.3 Microstructure after Gas Forming

Fairly uniform microstructure was obtained after completion of forming. The microstructure shows brick-shaped grains and subgrains, as shown in Figure 6-5(a). The mean grain size is 13.6 μm. By comparison of the grain structures before and after blow forming, it can be seen that most of the grains and subgrains have grown. The average aspect ratio of the grains was measured to be 4.9. The elongated grains with subgrain boundary arrays have illustrated the occurrence of subgrains re-arrangement as well. It is obvious that the brick subgrains have coarsened to as big as 20 μm. This is likely ascribed to subgrain boundary migration during blow forming.
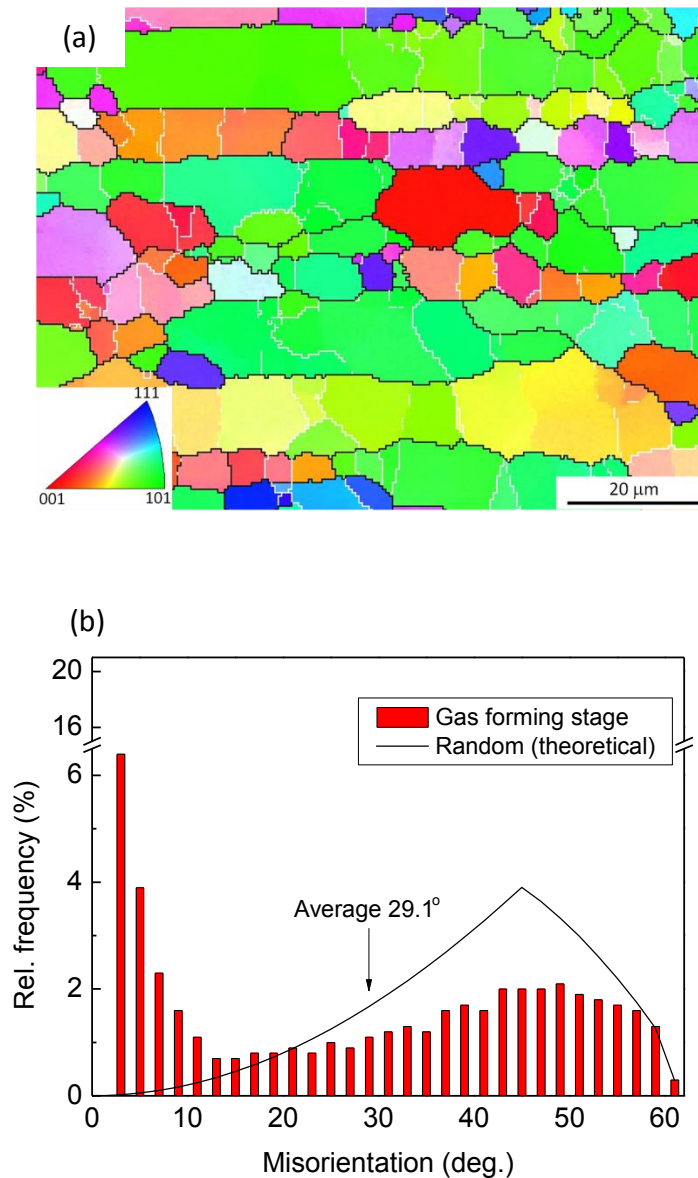
Figure 6-5 (a) EBSD map of AA5083 at the end of gas forming showing brick-shaped grain structures and (b) grain boundary misorientation distribution.

The average misorientation angle was determined to be 29.1º, and the fraction of HAGBs was 67%. As shown in Figure 6-5(b), there is a noticeable change in the proportion of grain boundaries with misorientation angles of 15 − 50º. As gas forming proceeded, the gradual transition from LAGBs to HAGBs occurred in the form of

subgrain boundary migration. By comparison of the distribution of boundary misorientation between hot drawing and gas forming, there is no rapid increase of HAGBs in the range of $> 50º$. Due to the absence of strain hardening, no obvious evidence of subgrain rotation was found during gas forming stage. Therefore, subgrain boundaries gradually migrated into grain boundaries, increasing the mid-misorientation angles in the range of $15 - 50º$. Subgrain boundary migration mainly occurred within the elongated grains, although the migration was not extensively completed showing some subgrain boundaries still retained after superplastic-like forming. In addition, dynamic recrystallization continued as gas forming proceeded, though in limited number, seemed to contribute to randomly distribution of the boundary misorientation angles. The fraction of the recrystallized grains was measured to be 4.5%.

Table 6-1 Summary of grain structures for AA5083 obtained from EBSD calculations.

Material	Mean grain size (μm)	Fraction of grain size < 10 μm	Average aspect ratio
Annealed	12.9	8%	2.3
Hot drawing	9.4	16%	5.3
Gas forming	13.6	11%	4.9

Table 6-1 summarizes the grain information of AA5083 in different forming stages. The smallest mean grain size is found from the hot drawn sample. The decrease of mean grain size is mainly due to the inclusion of fine grains (grain size < 10 μm) when calculating the grain diameters, as can be seen from Table 6-1, where the fraction of

fine grains is increased. As gas forming progressed, the grain structure has a decreased fraction of fine grains. The decreased portion of fine grains is likely due to grain growth of these grains. As a result, these growing grains are not included in the calculation of small grains since they are already bigger than 10 µm.

6.3   TEXTURE EVOLUTION

6.3.1   Pole Figures

Figure 6-6 provides the corresponding texture data in the form of {111} pole figures. The texture intensity values that were calculated by the CHANNEL software for strength of clustering at the poles relative to a random texture are illustrated by the smoothing contours. The texture intensity of 1.0 indicates a completely random texture. The orientations present here are near the typical deformation texture components [151], Copper, {112} <111>, Brass, {110} <112> and S, {123} <634>.
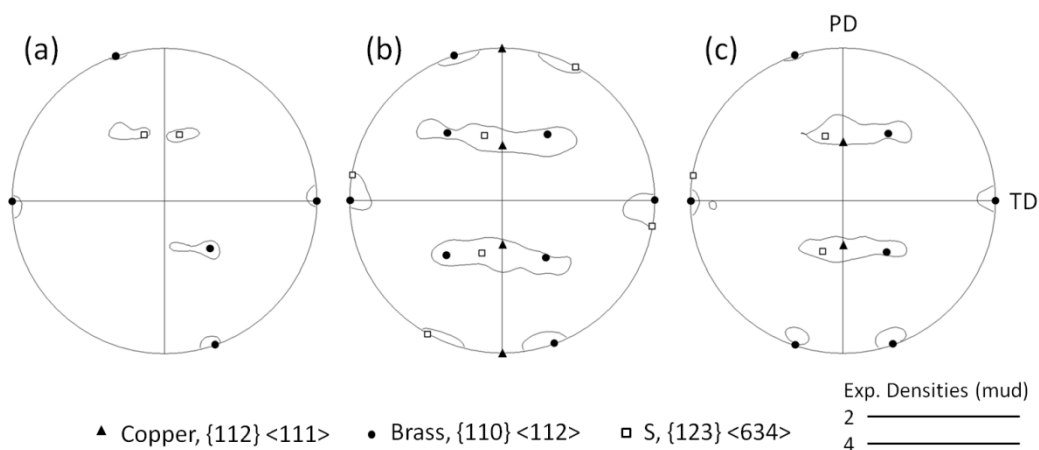
Figure 6-6 {111} pole figures for AA5083 (a) in annealed condition, (b) after hot drawing and (c) after gas forming.

The contour lines mainly show symmetric shapes indicating that most of the components listed in the pole figures are present. For the parent material (Figure 6-6(a)), the intensity value of 2.4 demonstrates a low level of texture. After hot drawing, it was found from the microstructure evolution in Figure 6-4(a) that the re-arrangement of subgrain boundaries within the elongated grains and the occurrence of recrystallization might give rise to overall level of texture. There was some texture developing, reaching the maximum intensity of 4.9 during hot drawing (Figure 6-6(b)). Figure 6-6(c) shows considerable weakening of the texture as gas forming proceeded. The texture intensity dropped to 3.6 after completion of superplastic-like forming.

Table 6-2 Proportions of three texture variants extracted from Figure 6-6.

Material	Copper, {112} <111>	Brass, {110} <112>	S, {123} <634>
Annealed	16%	20%	35%
Hot drawing	17%	35%	46%
Gas forming	14%	28%	40%

The proportions of each texture variant are summarized in Table 6-2. It is clear that the material, which has undergone hot drawing, contains more Brass and S textures as compared to it was in the annealed condition. The increase in the Brass texture component for aluminum alloy at elevated-temperature deformation has been reported by Bate *et al* [207]. The subsequent gas forming process would weaken texture intensity as the fractions of Brass and S textures decreased. One implication of the

variation was associated with the microstructure information, in which a proportion of LAGBs (or subgrains) accompanied with occurrence of dynamic recrystallization was rotated to a preferred orientation (Brass or S) during hot drawing. This is consistent with the subgrain rotation observed through hot drawing. However, the material that had been quickly deformed by drawing was then imposed to a relatively slow strain rate (2×10^{-3} s^{-1}) in the gas forming stage. During this stage, grain growth and subgrain boundary migration were dominating, which have influenced the abilities of grains to rotate and in turn led to decreased portion of the texture.

6.3.2 Orientation Distribution Functions

As a high stacking fault FCC metal, aluminum mainly contains three types of texture, i.e. Copper, Brass and S components. Additionally, there likely exist some more texture components [150], such as Cube, {001} <100> and Goss, {110} <100>, that have not been identified by the pole figures in Figure 6-6. A detailed description of the textures observed before and after hot deformation is provided by the orientation distribution functions (ODFs), as show in Figures 6-7, 6-8 and 6-9.

By comparison of the three ODFs, the primary texture containing Brass component, which was previously insignificant, predominate during hot drawing. The Brass component located at $\varphi_1=35°$, $\Phi=45°$, $\varphi_2=90°$, have the texture intensity of 4.8, 10.2 and 5.6, respectively. The increase of Brass component was consistent with that only after high strain-rate deformation was the peak in orientation density near {110} <112> retained [208]. This trend indicated that overall multiple slip occurred during hot drawing. However, the contribution of Brass component decreased with decreasing strain rate during gas forming.
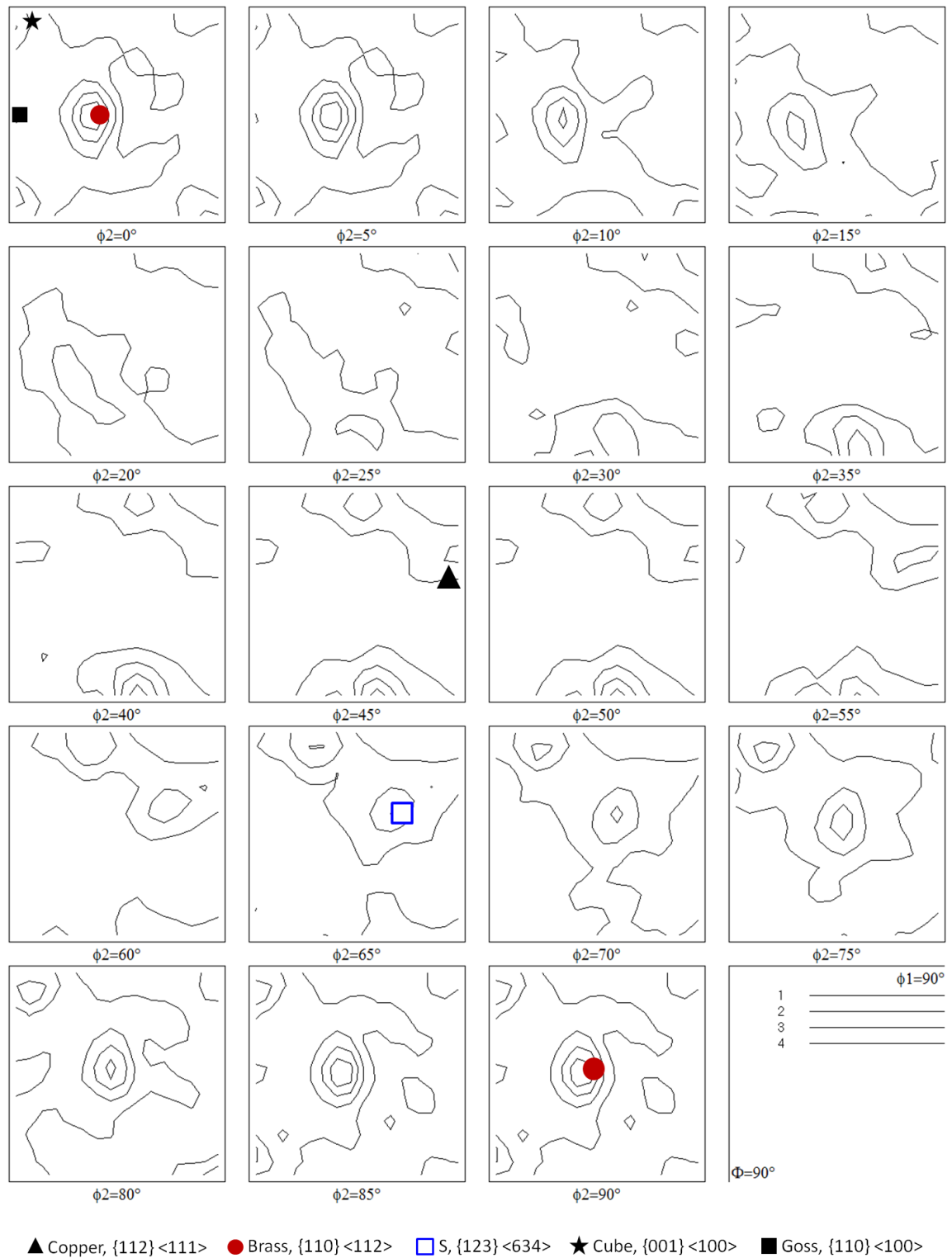
Figure 6-7 ODF of annealed AA5083. The positions of typical texture components are indicated.
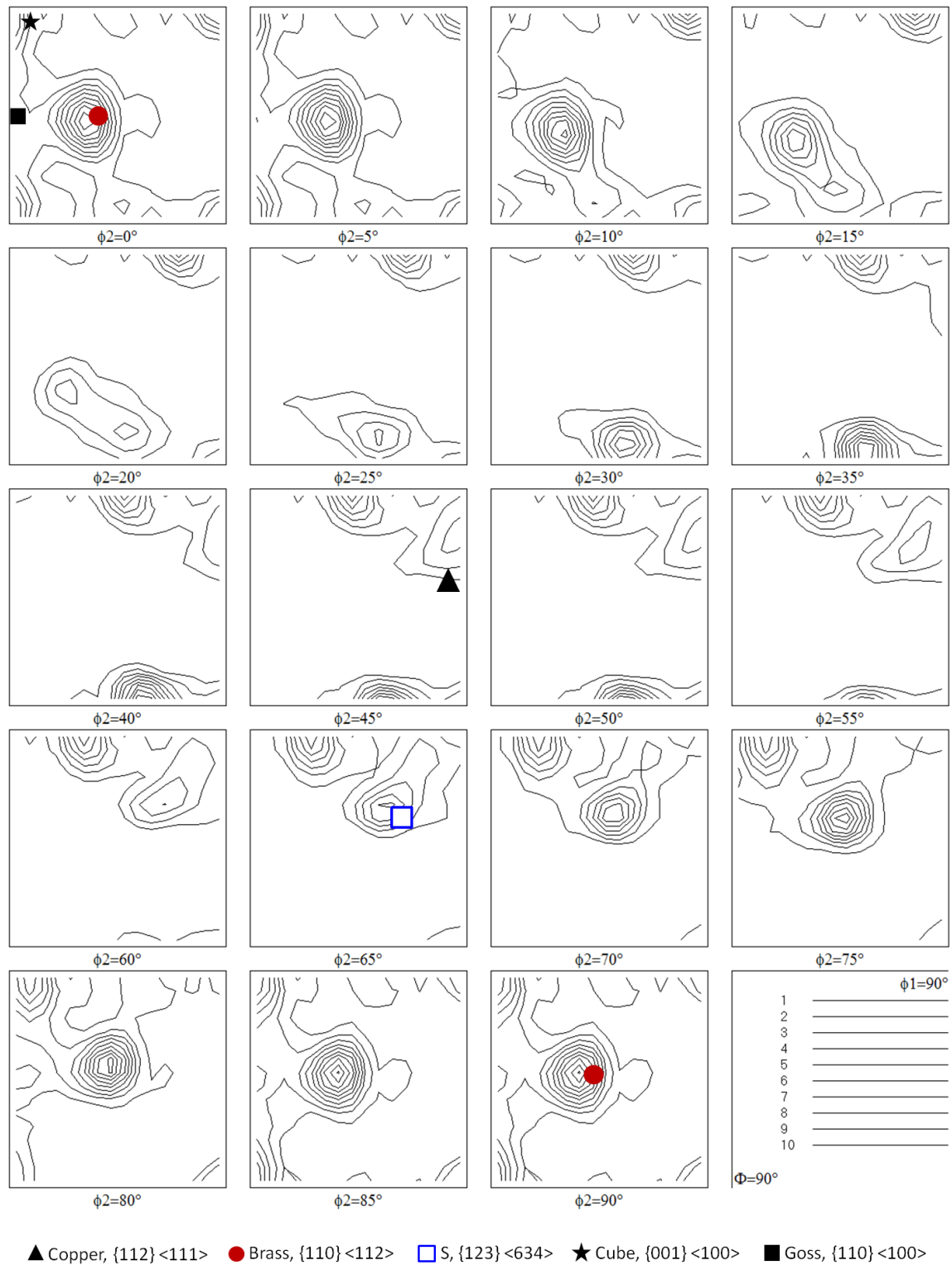
Figure 6-8 ODF of AA5083 at the end of hot drawing. The positions of typical texture components are indicated.
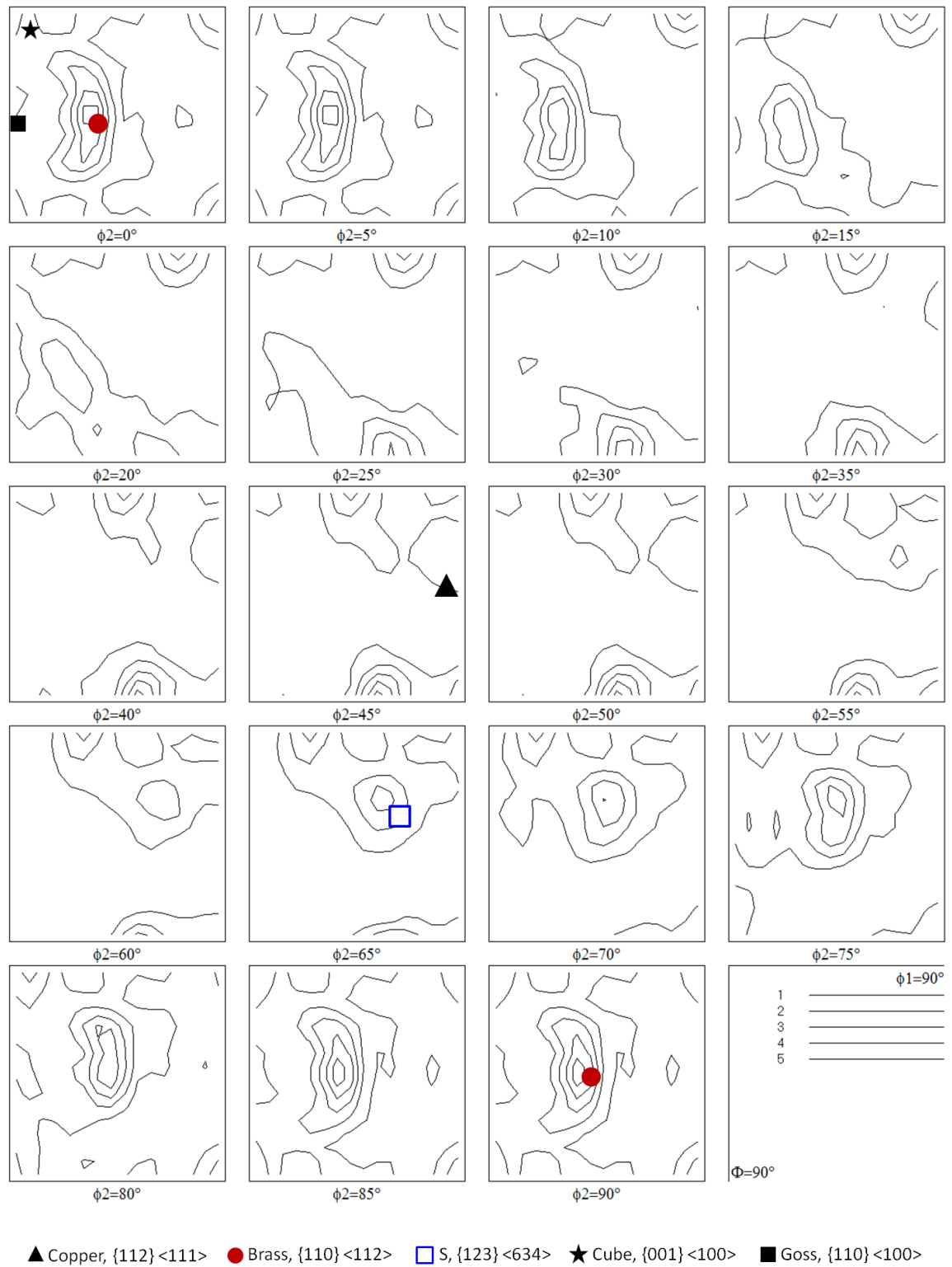
Figure 6-9 ODF of AA5083 at the end of superplastic-like forming. The positions of typical texture components are indicated.

The Goss, {110} <100> is recognized as a discontinuous recrystallization texture component [209], exhibiting a very weak intensity throughout forming. The increased Cube, {001} <100> component after hot drawing was removed during gas forming, as shown in Figure 6-9. Therefore, it can be concluded that the amount of slip system decreased as strain rate was reduced in the gas forming stage.

It is clear that the ODF after gas forming revealed splitting of the Brass component in the $\varphi_2=0^\circ$ section. This also represents formation of recrystallization texture [208], though limitedly distributed in the microstructure after superplastic-like forming as shown in Figure 6-5.

6.3.3 Inverse Pole Figures

The crystals are commonly known to rotate towards either the <111> or <100> orientation for FCC materials depending on the starting orientation. In order to study the orientation of fiber texture in the case of hot drawing, the inverse pole figures were obtained to determine grain rotations during this stage.

As shown in Figure 6-10, it displays a small concentration of grain orientation in the vicinity of <100> along the sheet plane direction (PD). The fiber texture after hot drawing, although not very strong, is found to be aligned along the plane direction with a maximum intensity of 4.18. The stretching stress applied by the drawing punch is deemed to result in the grain rotations. Additionally, during the course of hot drawing, a greater proportion of grains seemed to rotate in the direction of <100> compared to that of <111>.
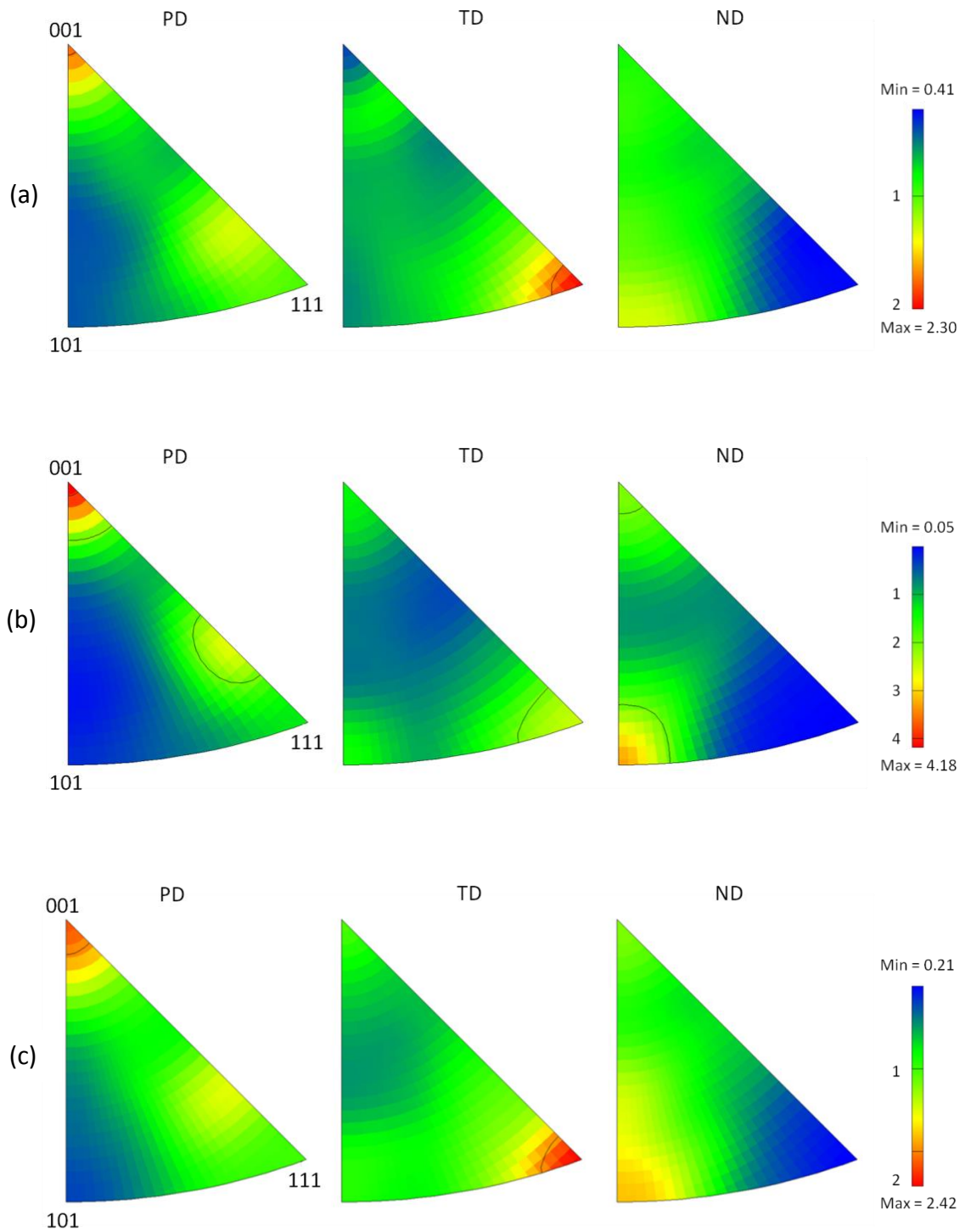
Figure 6-10 Inverse pole figures of AA5083 (a) in annealed condition, (b) after hot drawing and (c) after superplastic-like forming.

The inverse pole figure at the end of gas forming is presented in Figure 6-10(c), however, it is noted that the maximum intensity along <100> orientation dropped to 2.42 after gas forming, which is similar to that of the annealed condition. In connection with microstructure evolution, subgrain boundary migration and grain growth were supposed to be responsible for the weakening of fiber texture in the gas forming stage. In addition, at intermediate strains, textures developed more slowly in coarse-grained materials [150]. Since the average boundary misorientation increased and fraction of LAGBs decreased after gas forming from Figure 6-5(b), the fresh and newly grown grains were then likely to be distributed randomly. As a result, the ability of grain to rotate was therefore weakened in this stage.

6.4 MICROSTRUCTURE DEPENDENT MECHANICAL PROPERTIES

6.4.1 Tensile Properties

To understand the microstructural evolution and evaluate the mechanical response before and after forming, uniaxial tensile tests were performed to obtain the relationship between microstructure and mechanical properties.

AA5083-H321 (parent material) and AA5083-O (annealed) specimens were used. The difference between the annealed and formed specimens is the deformation procedure: (i) the annealed sample was without any deformation, and (ii) the formed sample underwent microstructural evolution during forming. As shown in Figure 6-11, the tensile specimens were machined from the formed part. The tensile specimens after hot

drawing together with gas forming (GF), labeled by GF #4, #6, #8 and #10 here, correspond to the locations where the microstructures were observed in Figure 6-1(b).
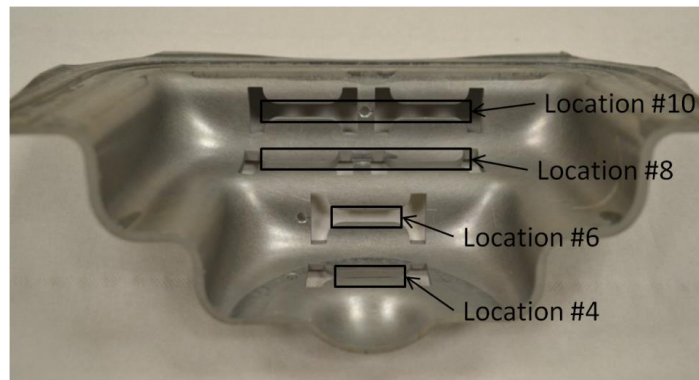
Figure 6-11 Photograph of the formed part showing the locations of tensile specimens.

Figure 6-12 shows the tensile stress − strain curves for the parent (H321), annealed (O) and formed (#4, #6, #8 and #10) specimens. From the tensile testing data plotted in Figure 6-13, the elongations of formed specimens (#4 to #10) are a little higher (about 5%) than that of the parent and annealed materials. The average yield strength (YS) decreased from 193 to 134 MPa, whereas the ultimate tensile strength (UTS) was little influenced showing identical values before and after superplastic-like forming.

As has been discussed, the texture components and orientation density of the material before and after forming are similar; therefore, the strength of the alloy is likely determined by microstructure evolutions (e.g. grain growth and movement of sub-structures).
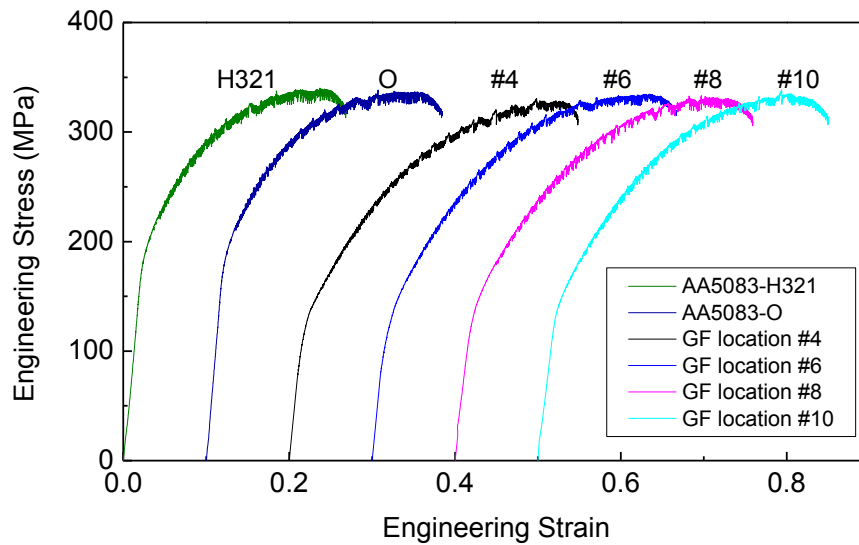
Figure 6-12 Engineering stress – strain curves for AA5083 at different processing conditions and specimen locations.
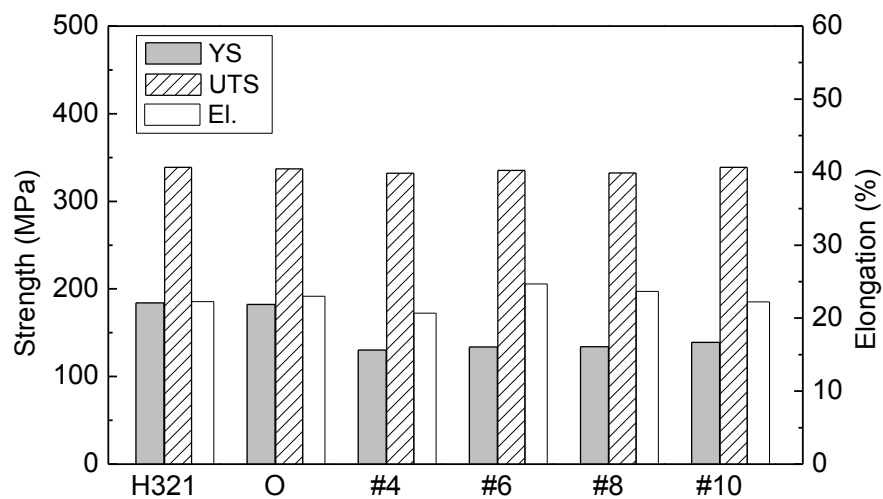
Figure 6-13 Comparisons of yield strength, ultimate tensile strength and tensile elongation for AA5083 at different processing conditions and specimen locations.

The influence of grain size on yield strength of a material at room temperature is given by Hall-Petch relation [210, 211]:

$$\sigma_y = \sigma_0 + k_1 d^{-1/2}$$ Eq. (6-1)

where σ_0 and k_1 are material constants [212], σ_0 is the yield strength for a single crystal [210], in which solutes and particles mainly contribute to the yield strength [213], and k_1 is a Petch parameter (unpinning constant) of yielding associated with the dislocation activity at grain boundary [211].

Due to the large grain sizes and high aspect rations after deformation, the grown grains are therefore responsible to the variations in yield strength of undeformed and deformed samples. The exact relationship for AA5083, however, has been rarely reported. From the investigation on the deformed aluminum by Hansen [214], a modified Hall-Petch relation was able to express the yield strength – grain size relationship with good agreement, yet the effects of grain size and strain on the Petch parameter k_1 had varying tendencies when the dislocation concept was introduced into the theoretical interpretations [215].

The annealed sample (Figure 6-3) comprise a high density of subgrain boundaries (also known as dislocation tangles), as compared to the deformed samples (Figure 6-4). From Figure 6-5, the significant development in microstructure is the decreased fraction of subgrain boundaries and occurrence of coarse grains, as compared to that of sample before hot deformation (see Figure 6-3). Generally, the flow stress is proportional to the root of the dislocation density [169]. The strain hardening associated with dislocation motion [216] and subgrain [217] have revealed that the increased density of dislocation cells could result in a higher yield strength arising, and

vice versa. In this case, the material was initially tensile tested under identical conditions at room temperature. Therefore, in addition to the grain size, subgrains might also play a role [218], since the material after hot processing contained less dislocation motion, leading to a lower yield point.

The yield strength and ultimate tensile strength of the annealed specimens are closed to that of the as-received AA5083-H321. This also corresponds to the stabilized microstructures before and after annealing, which is probably that the static annealing in the process here did not influence much on the changes of dislocation or subgrain boundary motion. Consequently, the structure was filled with high-density dislocations that would hinder the movement of dislocation during plastic deformation, resulting in similar yield strength as that of parent material (AA5083-H321).

6.4.2 Microhardness

On the basis of Hall-Petch relation, the hardness in terms of a similar relationship dependent on grain size was also connected to determine the variations in hardness [219]. The hardness of a material is proportional to the yield stress and has an approximate relationship of $H_V \approx 3\sigma_y$ for rigid perfectly-plastic material [215]. The plastic constraint factor 3, increases for high strain-hardening materials.

For AA5083-H321, it is a strain hardened and stabilized alloy. The strain-hardening process during fabrication has introduced plastically deforming the metal below recover and recrystallization temperature (150ºC). This process produced some weak-intensity texture components that could also retained after annealing, as can be found in Figure 6-7. For the specimens from #1 to #10 after forming, dynamic recovery generated the subgrain structure and increased internal dislocation density [205].

120
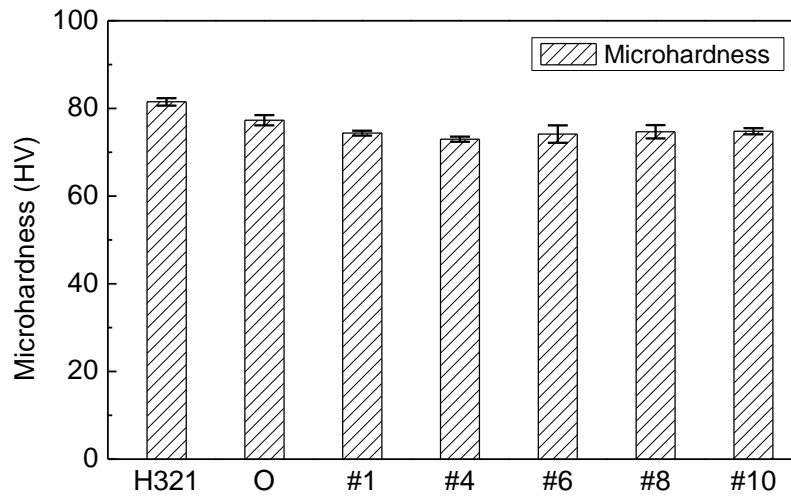
Figure 6-14 Comparison of microhardness for AA5083 at different processing conditions and specimen locations.

The LAGBs of annealed AA5083, as shown in Figure 6-3(b), has a fraction of 60% indicating a large number of entangled subgrain boundaries. The LAGBs fraction in the formed part decreases to 33% (Figure 6-5(b)). It is known that those subgrain boundaries are produced due to the movement and multiplication of dislocations [150]. The consequence of this process is that further plastic deformation will require more energy, or in other words, the annealed material is harder (higher yield stress) due to a more fraction of LAGBs, and vice versa.

On the basis of hardness, Figure 6-14, the amount of recrystallization was calculated to be around 8% using a previous approach [53]. In addition, calculations based on the EBSD characterization showed that only 4.5% recrystallized grains was produced after forming at 400ºC. Both approaches have revealed the occurrence of recrystallization, thought in limited number; it seemed to contribute to the decrease of hardness.

6.5 SUMMARY

The microstructure evolution and the variations in mechanical response were investigated in the stages of hot drawing and gas forming. The conclusions are summarized as follows:

1. The maximum sheet thinning after process optimization is 40%. The yield strength of formed AA5083 decreased due to the microstructural features (coarsening of the grains and re-arrangement of the subgrain boundaries) occurred during forming.

2. The annealed AA5083 contains a large fraction of subgrain boundaries and weak-intensity texture components.

3. The main deformation mechanisms during hot drawing are subgrain boundary migration and subgrain rotation. The arrays of elongated grains and formation of new HAGBs containing more Brass and S components increased the texture intensity.

4. The blow forming operation can weaken the texture intensity, mainly because the relatively slow strain rate (2×10^{-3} s^{-1}) aided further subgrain boundary migration and grain growth. The initial fairly equiaxed structure in the annealed AA5083 was replaced by brick-shaped structures and a small amount (4.5%) of recrystallized grains during superplastic-like forming.

CHAPTER 7   FINITE ELEMENT MODELING FOR SUPERPLASTIC-LIKE FORMING OF AA5083

A model based upon dislocation density and calibrated using tensile test data yielded a good description of the deformation behavior of non-superplastic grade AA5083. The deformation behavior under tensile test conditions was then studied by post processing in connection with the physical-based model. This model can inherently incorporate the physics of plasticity over a large strain, strain rate and temperature range. Henceforth, it was implemented into macroscopic simulations for the superplastic-like forming process at 400 and 500ºC. Finite element modeling (FEM) results were obtained for evaluating the thickness uniformity and thinning characteristics after deformation and this method has been validated between the simulation and experimental data.

7.1   FLOW STRESS MODEL AND ITS EVOLUTION

7.1.1   Material Model

The isotropic hardening/softening and restoration behavior are employed to describe the evolution of flow stress. The flow stress is assumed to consist of two parts, as discussed by Bergström [169] and Kock [220].

$$\sigma_y = \sigma_G + \sigma^* \qquad \text{Eq. (7-1)}$$

where σ_G is the athermal stress contribution from the long-range interactions of the dislocation substructure, and σ^* is the friction stress needed to move dislocations through the lattice and to pass short-range obstacles. Thermal vibrations can assist the stress to overcome these obstacles.

The long-range term (athermal stress) in Eq. (7-1) is written as

$$\sigma_G = m\alpha G b \sqrt{\rho_i} \qquad \text{Eq. (7-2)}$$

where m is the Taylor orientation factor translating the effect of the resolved shear stress in different slip systems into effective stress and strain quantities. α is a proportionality factor, G is the shear modulus, b is the Burger's vector and ρ_i is the immobile dislocation density [169]. Contributions from the Hall-Petch effect and solute hardening are accounted for indirectly via the initial dislocation density. The evolution of the long-range term is quite insensitive to the value of the used initial dislocation density. The contribution from precipitate hardening is not needed for the current material.

The second term (friction stress) in Eq. (7-1), the strain rate dependent part of the yield stress and the short-range stress component [221], is written as

$$\sigma^* = \tau_0 G \left[1 - \left[\frac{kT}{\Delta f_0 G b^3} \ln \left(\frac{\dot{\bar{\varepsilon}}_{ref}}{\dot{\bar{\varepsilon}}^p} \right) \right]^{1/q} \right]^{1/p} \qquad \text{Eq. (7-3)}$$

where Δf_0 is the free energy required to overcome the lattice resistance or obstacles without aid from external stress. The quantity τ_0 is the athermal strength that must be exceeded in order to move the dislocation across the obstacles [222]. $\dot{\bar{\varepsilon}}_{ref}$ and $\dot{\bar{\varepsilon}}^p$ are the reference and plastic strain rate, respectively. The other parameters for this model

are described in Tables 7-1 and 7-2 hereinafter.

7.1.2 Evolution of Immobile Dislocation Density

The basic components for the yield stress in Eq. (7-1) are obtained from equations (7-2) and (7-3). However, the evolution of ρ_i in Eq. (7-2) needs to be further computed. The model for evolution of the immobile density has two parts: hardening $\dot{\rho}_i^{(+)}$ and restoration $\dot{\rho}_i^{(-)}$ [223] as

$$\dot{\rho}_i = \dot{\rho}_i^{(+)} + \dot{\rho}_i^{(-)} \qquad\qquad \text{Eq. (7-4)}$$

7.1.2.1 Hardening

The BCC structured material has a sole plastic hardening state hardly influenced by temperature. In the case of FCC materials, such as aluminum and copper, the plastic strain is mostly dependent not only on the temperature but also on the strain rate [224, 225]. It is assumed that mobile dislocations move, on average, a distance Λ (named as the mean free path), before they are immobilized or annihilated to immobile dislocation on the next cell. As a consequence, introducing hardening to the flow stress is required to interpret the effects of thermal obstacles during motion. According to the Orowan equation, the density of immobile dislocations and their average velocity are proportional to the plastic strain rate [173]:

$$\dot{\rho}_i^{(+)} = \frac{m}{b}\frac{1}{\Lambda}\dot{\bar{\varepsilon}}^p \qquad\qquad \text{Eq. (7-5)}$$

where m is the Taylor orientation factor used for polycrystalline metals. One further remark is that the hardening represented by the current model has ignored the initial

(small) strain effects on account of the weak strain hardening, especially for the deformation at the slow strain rates and high temperatures.

The mean free path (Λ) for an FCC material can be computed from the grain size (g) and dislocation sub-cell diameter (s) [226]:

$$\frac{1}{\Lambda} = \frac{1}{g} + \frac{1}{s} \qquad\qquad \text{Eq. (7-6)}$$

In this model, K_c is a calibration parameter dependent on temperature. It describes the relationship between the dislocation structure and sub-cell size:

$$s = K_c \frac{1}{\sqrt{\rho_i}} \qquad\qquad \text{Eq. (7-7)}$$

7.1.2.2   Recovery

With regards to the recovery process, the glide and climb of dislocations are introduced into this model since the primary focus is on the elevated-temperature behavior (namely hot forming). Based on the formulation by Bergström [227], the immobile dislocation density recovered by dislocation glide is proportional to the plastic strain rate as

$$\dot{\rho_i}^{(-)} = \Omega \rho_i \dot{\bar{\varepsilon}}^p \qquad\qquad \text{Eq. (7-8)}$$

where Ω is a recovery function that is dependent on temperature and strain rate. In addition to the dislocation glide, this study together with a model for recover by climb is then deduced from Militzer *et al* [186]:

$$\dot{\rho_i}^{(-)} = 2c_\gamma D_V \frac{c_V}{c_V^{eq}} \frac{Gb^3}{kT} \left(\rho_i^2 - \rho_{eq}^2 \right) \qquad\qquad \text{Eq. (7-9)}$$

where c_V and c_V^{eq} are current fraction and equilibrium vacancy concentrations, c_γ is a calibration coefficient, D_V is a self-diffusivity, and ρ_{eq} is the equilibrium density of dislocation.

7.1.3 Evolution of Vacancy Concentration

The annihilation of vacancies is diffusion controlled and takes place at grain boundaries and dislocations. In FCC materials, the concentration of strain-induced vacancy is significant due to their low diffusivities. A model for excess vacancy concentration with generation and annihilation components has been proposed by Militzer *et al* [186]. Assuming that only long-range stress contributes to vacancy formation and introducing mean free path (Λ), it is written as

$$\dot{C}_V^{ex} = \left[\chi \frac{\sigma b^2}{Q_{vf}} + \varsigma \frac{c_j}{4b^2} \right] \frac{\Omega_0}{b} \dot{\bar{\varepsilon}} - D_{Vm} \left(\frac{1}{\Lambda^2} \right) \left(C_V - C_V^{eq} \right) - c_V^{eq} \left(\frac{Q_{vf}}{T^2} \right) \Delta T \qquad \text{Eq. (7-10)}$$

where χ is the fraction of mechanical work for the vacancy generation, ς is the neutralization effect by vacancy emitting and absorbing jogs, c_j is the concentration of jogs, Ω_0 is the atomic volume, D_{Vm} is the vacancy diffusivity, and Q_{vf} is the activation energy for forming a vacancy. It is assumed that the stress σ in Eq. (7-10) is equal to the flow stress during a plastic deformation.

7.1.4 Implementation of the Flow Stress Model

To compute the flow stress evolution for arbitrary paths, the radial return algorithms from references [228-230] are commonly used. This requires updated internal variables and hardening modulus for each time increment. As shown in Figure 7-1, the input and output arrows to the strain − stress box illustrate the return method for the control

variables that need to be updated during a time step. The left superscript of each variable is the time step counter.
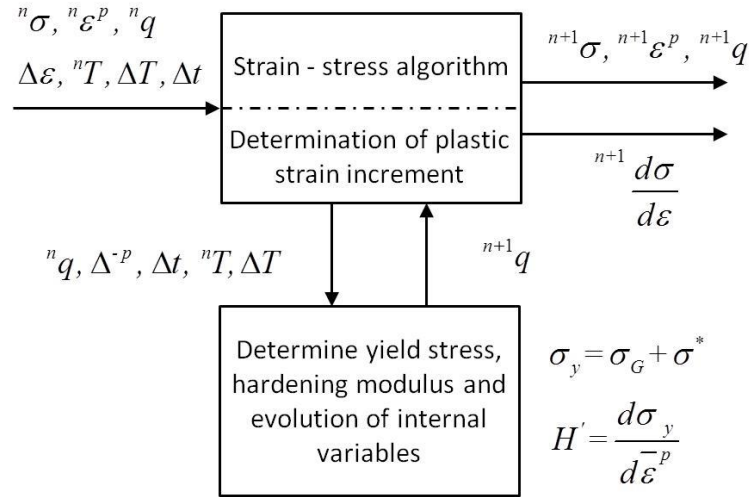
Figure 7-1 The computation of internal variables and flow stress in FEM.

For the stress – strain constitutive law, the plastic strain is an internal variable. It is replaced in the current model by two internal state variables, the immobile dislocation density (ρ_i) and the vacancy concentration (c_V). As a result, the vector q with these variables is introduced as

$$q^T = (\rho_i, c_V) \qquad\qquad \text{Eq. (7-11)}$$

For the stress-update algorithm, it is the solution of determining yield stress (σ_y) and plastic strain ($\bar{\varepsilon}^p$) from these internal state variables. The hardening modulus can be defined as

$$H' = \frac{\mathrm{d}\sigma_y(q)}{\mathrm{d}\bar{\varepsilon}^p}$$

Eq. (7-12)

A more detailed derivation of the flow stress model and its implementation can be found from Lindgren *et al* [222] and Ales *et al* [226].

7.2 CALIBRATION OF THE MODEL

7.2.1 Calibration of Stress – Strain Curves

Tensile test results of AA5083 at several temperatures and strain rates (from room temperature up to 550ºC and strain rates from 10^{-4} up to 10^{-1} s^{-1}) have been adopted in the calibration. In order to make a comparison of the model and experimental results, the parameters used in the present model are summarized in Table 7-1. The tool used in the material model calibration is a MATLAB based program.

Comparisons of experiments and predictions of the flow stress using the parameters in Table 7-1 are plotted in Figures 7-2 and 7-3. The stress – strain curves at a high strain rate of 10^{-1} s^{-1} and slow strain rates of 10^{-4} to 10^{-3} s^{-1} are plotted depending on low-/high- temperature ranges. The measured values have been smoothed out so as to remove serrations or reading errors due to the testing. The dots denote measurements for different temperatures and strain rates, and the lines denote calculations by the dislocation density model. Only selected curves are plotted, and more calibration details based on various temperatures and strain rates have been carried out under the same conditions but not reported here. The overall matching shows good agreement between the computed and measured stress – strain curves.

Table 7-1 Known or assumed parameters for AA5083.

Parameter	Notation	Value	Dimension	Reference
Empirical coefficient	α	0.3	---	[231]
Boltzmann's constant	k	1.38×10^{-23}	J/K	
Melting temperature	T	638	℃	[31]
Taylor factor	m	3.06	---	[181, 182]
Atomic volume	Ω_0	1.66×10^{-29}	m^3	[232]
Burger's vector	b	2.86×10^{-10}	m	[233]
Young's modulus at 400 ℃	E	33	GPa	[234]
Shear modulus at 400 ℃	G	12.7	GPa	
Poisson's ratio	ν	0.33	---	
Activation energy for forming a vacancy	Q_{vf}	1.23×10^{-19}	J	[235]
Energy barrier for vacancy migration	Q_{vm}	1.09×10^{-19}	J	[236]
Self-diffusion activation energy	$Q_v = Q_{vf} + Q_{vm}$	2.32×10^{-19}	J	[235]
Initial vacancy diffusivity	D_{vm0}	1.71×10^{-4}	m^{2}s^{-1}	[237]
Reference strain rate	$\dot{\bar{\varepsilon}}_{ref}$	10^6	s^{-1}	[238]
Change in entropy for vacancy creation	ΔS_{vf}	1.92 k	J/K	[239]
Fraction of mechanical work for vacancy formation	χ	0.1	---	
Formation energy of thermal jogs	Q_{fj}	3.53×10^{-20}	J	[222]
Neutralization effect by vacancy emitting and absorbing jogs	ς	10	---	[186]
Initial immobile dislocation density	ρ_{i0}	10^{12}	m^{-2}	[238]
Equilibrium vacancy concentration	C_V^{eq}	3.04×10^{-5}	---	[240]
Initial grain size	g	13.6×10^{-6}	m	
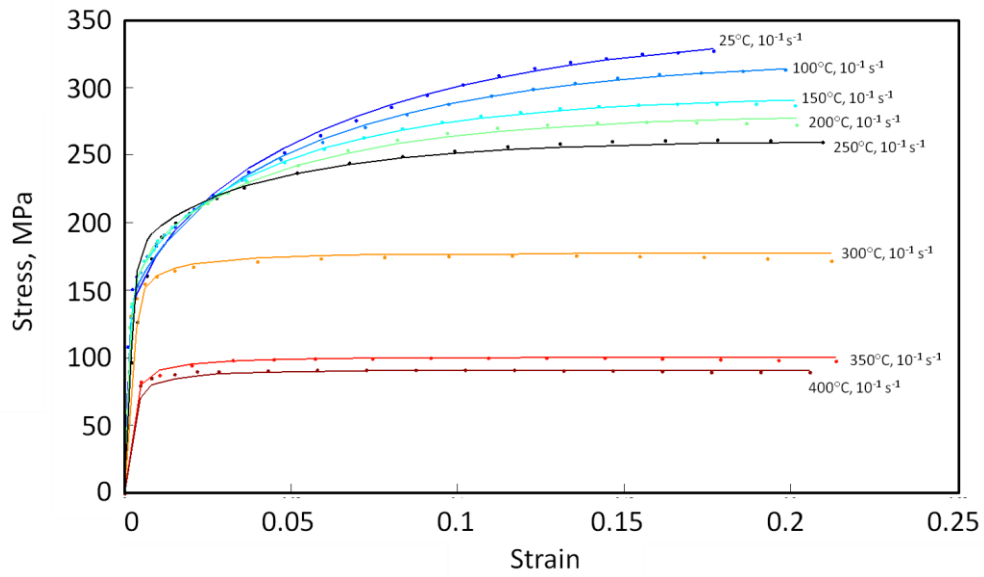
Figure 7-2 Measured and computed stress – strain curves for AA5083 at a strain rate of 10^{-1} s^{-1} from 25 to 400 °C.
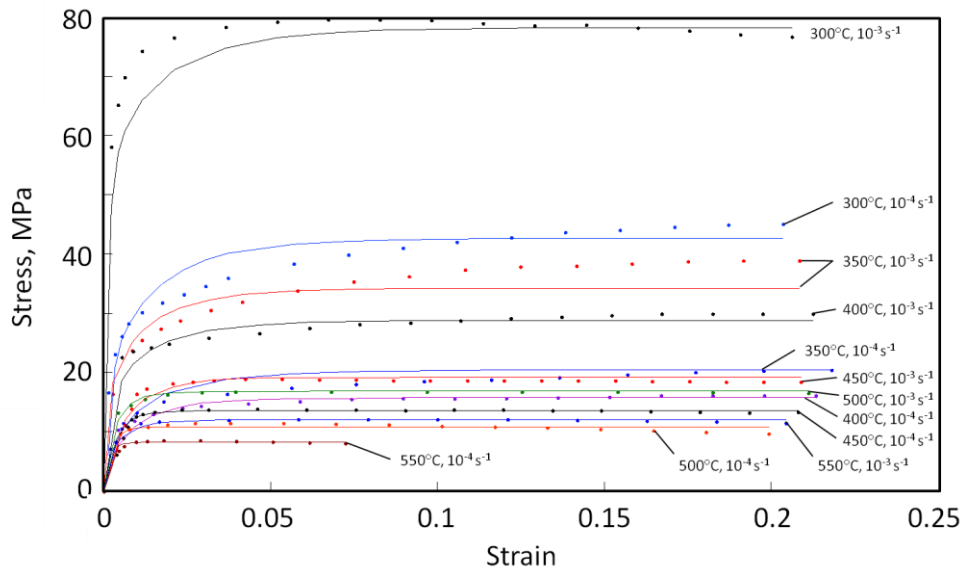
Figure 7-3 Measured and computed stress – strain curves for AA5083 at strain rates of 10^{-4} and 10^{-3} s^{-1} from 300 to 550 °C.

It should be noted that there is some deviation between the measured and calculated data within the initial strain hardening stage ($\varepsilon < 0.02$), as can be seen from Figure 7-3. The deviation might arise from the small hardening effect that is not taken into account in the material model. However, for the material that undergoes large strain deformation during superplastic-like forming, recovery (subgrain-boundary motion) will dominate the microstructural evolution and balance out the effects of strain hardening, leading to a constant flow stress at a given temperature.

The temperature-dependent parameters are provided in Table 7-2. The quantity τ_0, as a short-range component in Eq. (7-3), is the strength that must be exceeded in order to move the dislocation across the barrier in the absence of thermal energy. The parameter Δf_0 is the active energy that overcomes the lattice resistance or obstacles without aid from external stress [52]. The temperature-dependent variations in τ_0 and Δf_0 indicate that the short-range stress σ^* is influenced by temperature changes.

Among these parameters, K_c is an approximate value related to the dislocation sub-cell diameter in short range. Considering the mean free path from equations (7-6) and (7-7), it can be concluded that a higher K_c value indicates larger sub-cell size and mean free path, consequently resulting in less hardening. There is an increase in K_c value when the deformation temperature increases from room temperature to 400ºC. However, because aluminum is a high stacking fault material, dynamic recovery is rapid and extensive at high temperatures [40]. Inasmuch as a larger portion of grains recovers at 450ºC or higher, there is an increase in the amount of subgrains. As a result, the hardening effects are likely to be weak as well. The parameter Ω is a parameter to describe recovery by dislocation glide and annihilation that can depend on temperature and strain rate. Calibration results have revealed that the recovery function increases

with temperature, while the recovery through dislocation climb c_γ is constant in the current model. The parameters p and q are used as constants in Eq. (7-3) for the short-range components.

Table 7-2 Calibrated parameters for AA5083 as temperature dependent.

T (℃)	25	100	150	200	250	300	350	400	450	500	550
τ_o	0.013	0.017	0.02	0.03	0.038	0.055	0.046	0.051	0.06	0.06	0.06
Δf_0	0.3	0.3	0.35	0.37	0.47	0.48	0.56	0.71	0.8	0.78	0.8
K_c	7.0	8.48	9.04	10.05	14.0	17.9	20.0	20.0	6.0	0.2	0.2
Ω	14.35	17.68	23.03	24.05	30.0	94.9	110.0	109.5	126.2	132.1	139.0
c_γ	Constant 0.0001										
p	Constant 0.76										
q	Constant 1.5										

7.2.2   Post Processing

The computed immobile dislocation density at the typical temperatures and strain rates is shown in Figure 7-4. From the modeling predictions, the immobile dislocation densities at the strain rate of 10^{-1} s^{-1} are mainly located between 10^{13} and 10^{14} m^{-2}. No direct measurement of dislocations has been performed experimentally. However, the acceptable forest dislocation value of AA6061 [238] have been determined to be of the order of 10^{14} m^{-2}. Moreover, the immobile (forest) dislocation densities of pure aluminum [241] and Al-Mg-Cu alloy [182] deformed within slow rates and large strains at elevated temperature has been reported to be in the range $10^{12} - 10^{13}$ m^{-2}, which is also corresponding to that of the computation shown in Figure 7-4(b).
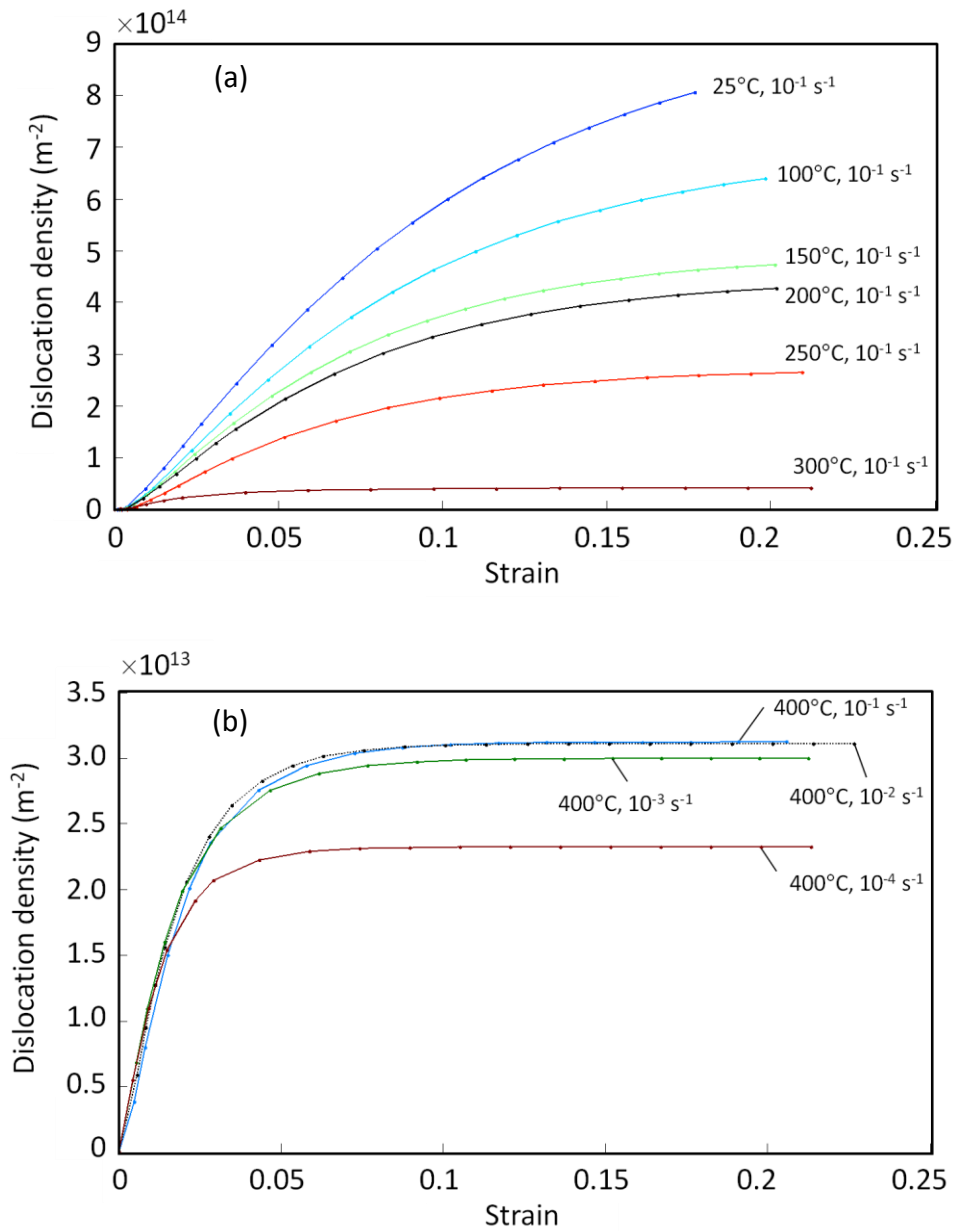
Figure 7-4 Computed dislocation density of AA5083 dependent on (a) temperature and (b) strain rate.

It can be observed that the density of immobile dislocations generated at a strain rate of 10^{-1} s^{-1} decreases with temperature increase (Figure 7-4(a)), while it also decreases with strain rate decrease at the same temperature (Figure 7-4(b)). In addition, the grain growth as a function of temperature and strain rate has been included to account for the

immobile dislocation changes in the predictions. This properly reveals that the grown

grains resulting in less hardening also lead to a lower immobile dislocation density.
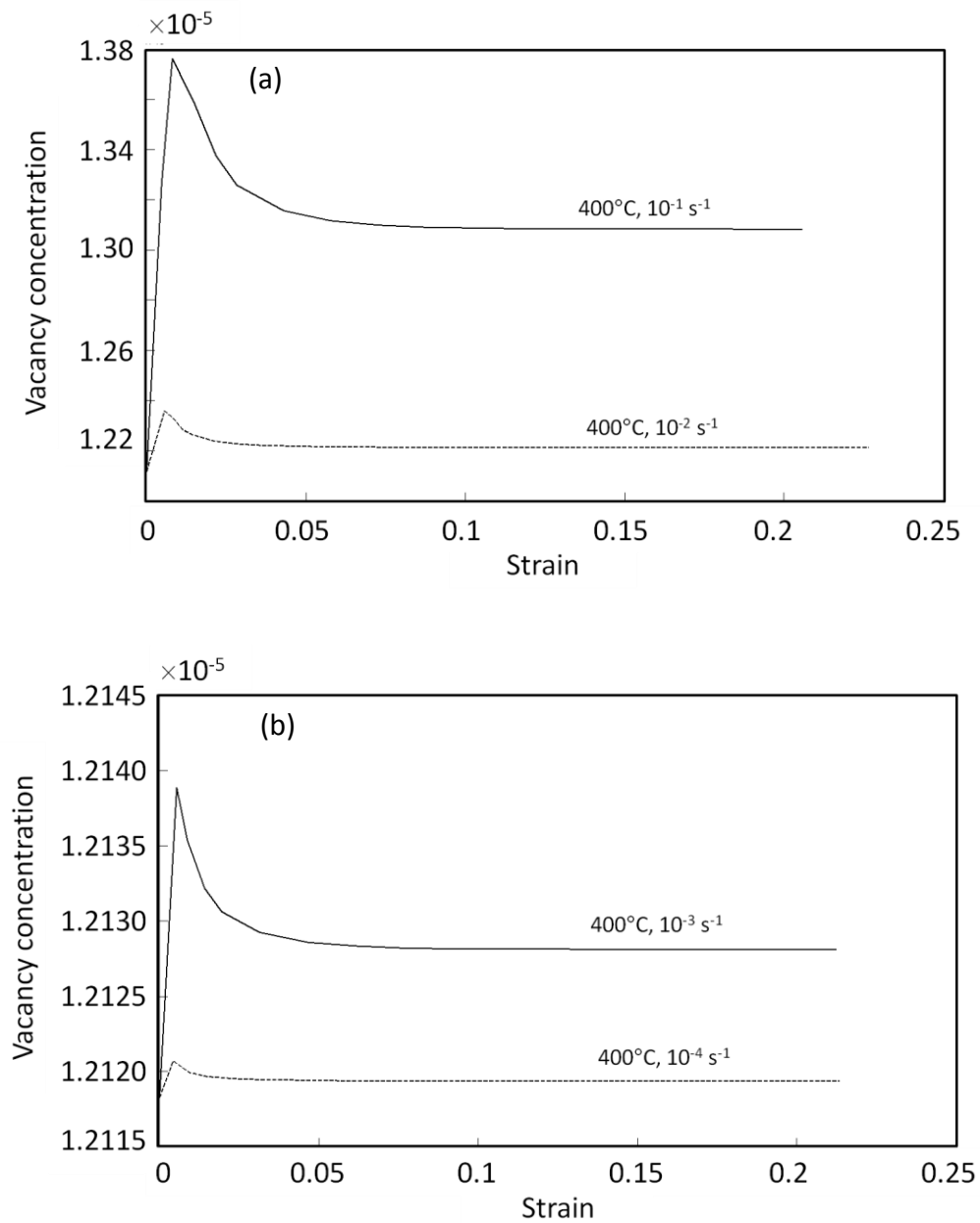
Figure 7-5 Computed vacancy concentration for AA5083 at 400°C.

Because of the comparatively lower diffusivities, excess vacancies are more important in FCC than in BCC materials [186]. A correlation between vacancy concentrations and strain rate under the deformation condition is therefore computed. The vacancy concentration for 400ºC is shown in Figure 7-5. During high-temperature deformation, the vacancy concentration is evidently increasing rapidly with strain rate. In view of a decreasing dislocation density dependent on decreasing strain rate, the annihilation rate also complies with this trend, where a lower annihilation rate at the beginning of straining is present. At the same time, the rate of excess vacancy formation during deformation is predicted to be increasing in a small strain range (within the strain of 0.01). Further observation has revealed that the vacancy concentration attains a maximum before reaching its steady-state value.

7.3   SIMULATION OF SUPERPLASTIC-LIKE FORMING

7.3.1   Element Description

The model used for the simulation is presented in Figure 7-6. It comprises of punch, metal sheet and die sets. A quarter model and symmetry boundaries were used. The tools (i.e. die and punch) were modeled using rigid elements. For the workpiece elements, solid elements were necessary to accommodate for double-sided contact. This significantly increases the computational time, as it is necessary to have several elements in the thickness direction in order to improve bending characteristics. The solid-shell element, an eight-noded fully integrated hexahedral element, is specially formulated to overcome that problem by simulating a shell type element while facilitating double-sided contact [199]. The size of a quarter sheet used as the solid

shell is 100×100 mm^2 with thickness of 3 mm. There are 1600 elements and 3362 nodes defined in the material model.
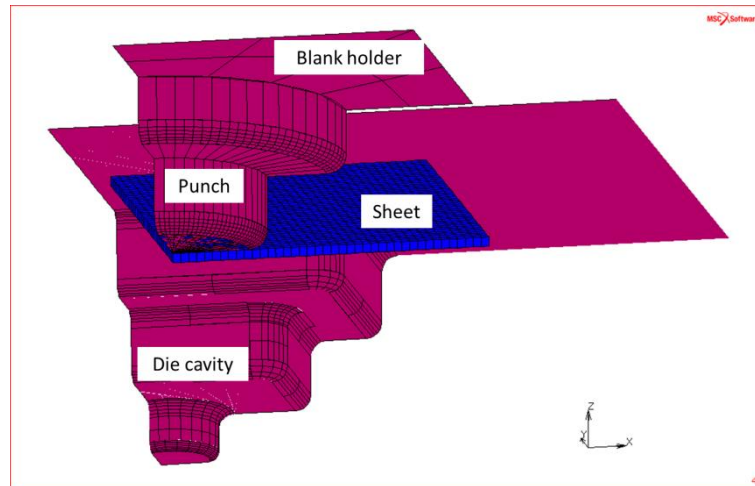
Figure 7-6 Solid shell elements and mesh of the simulation model.

7.3.2   Thickness Distributions and Equivalent Plastic Strain

The computed thickness distributions across the workpiece are shown in Figure 7-7. The contour bands display the different thickness regions. During forming, the sheet gradually contacted the punch radius and stretched as the punch moving down, as shown in Figure 7-7(a). Stretching occurred due to the resistance between the sliding material and punch surface. After applying gas pressure on the sheet surface, the material was locked in the vicinity of die shoulders by the gas pressure and die surface, as shown in Figure 7-7(b). The localized thinning, as indicated in Figure 7-7(b), was therefore found just near these radii, and was assumed to be correlated with geometric inhomogeneity during gas forming. The minimum sheet thicknesses at the end of hot drawing and gas forming were 2.66 mm and 2.05 mm, respectively.
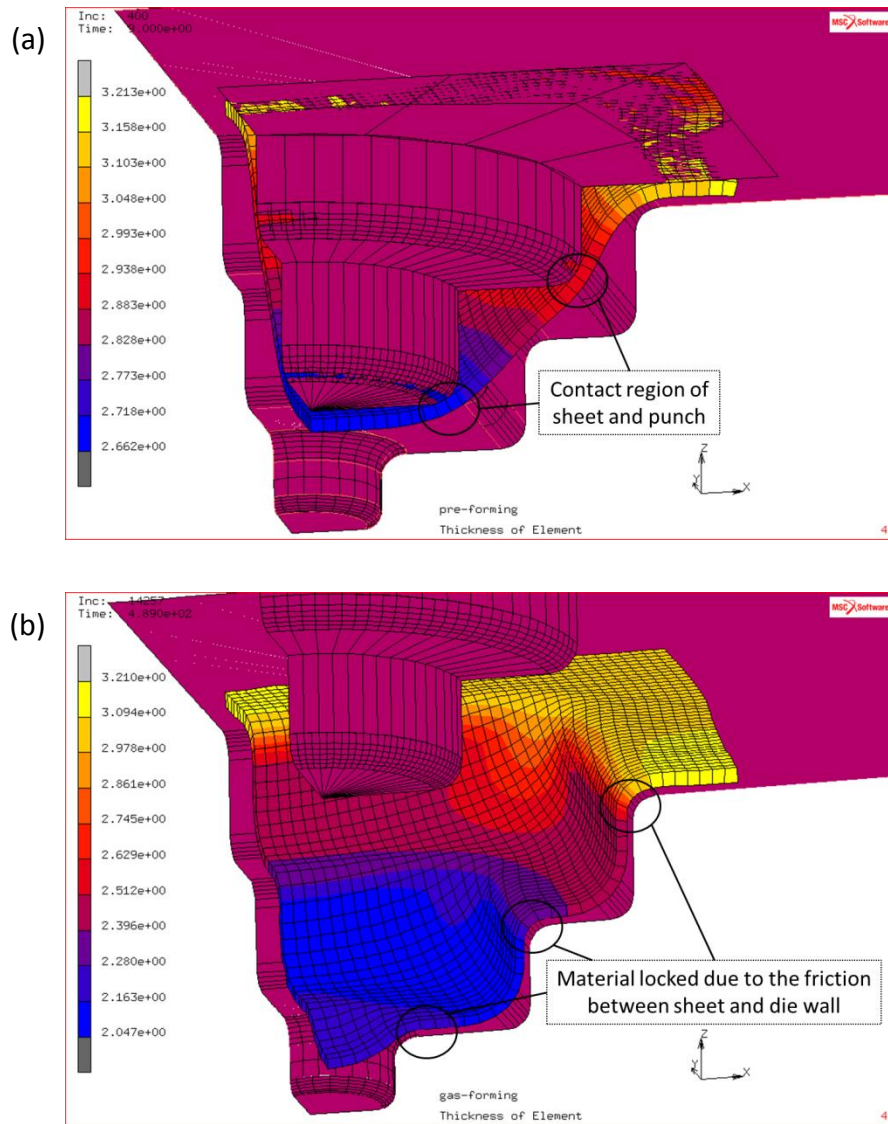
Figure 7-7 The contours of thickness distributions in mm (a) after hot drawing and (b) after gas forming.

Figure 7-8 shows the total equivalent plastic strain corresponding to the thickness distribution (Figure 7-7) of the workpiece at the end of hot drawing and gas forming stages. The high plastic strains are mainly present in the areas where the material is in contact with the punch surface in the hot drawing stage and the die radius in the gas forming stage.
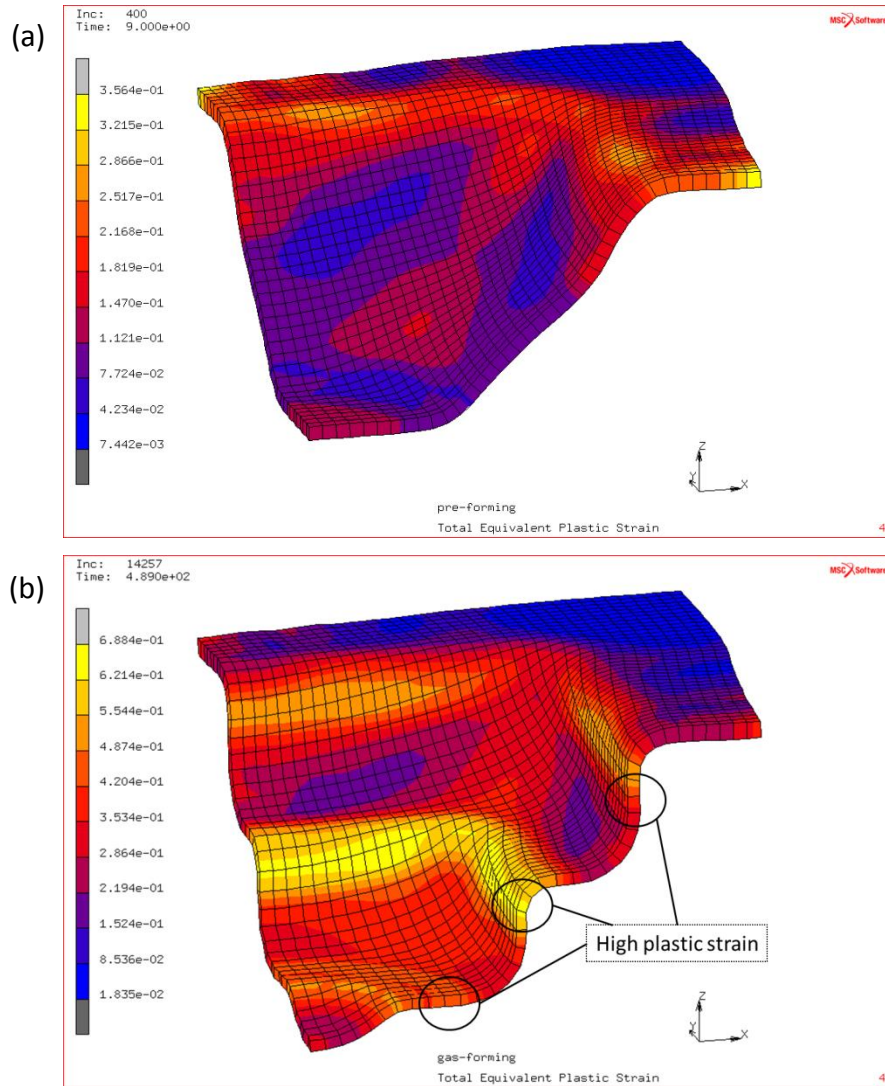
Figure 7-8 The contours of total equivalent plastic strain (a) after hot drawing and (b) after gas forming.

The difference in thickness profiles from sample dome center to flange between the simulations and the experiments is plotted in Figure 7-9. The localized thinning areas from simulation and experiment appear at the same locations. The measured thickness values are smaller than the computed, especially in the vicinity of dome center (arc length < 30 mm). It is mainly during the end of gas forming, i.e. the sheet is filling the

bottom die cavity, that the measured and computed deformations diverge. For the rest of the areas, the computed thicknesses agree well with those measured. Additionally, the plastic strain predicted in the simulation reveals that a maximum plastic strain of 0.65 was achieved. As for comparisons of thickness and plastic strain shown in Figure 7-9, the two critical areas where localized thinning occurred were also found to have larger plastic strains when compared with the other locations.
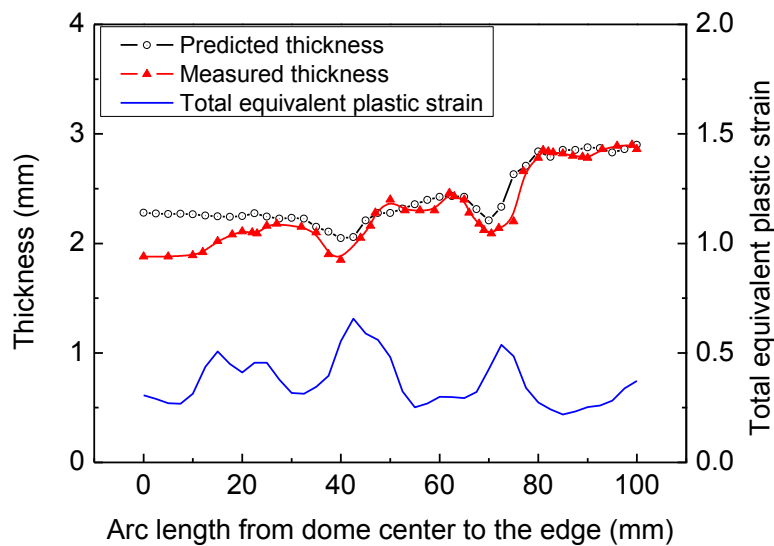
Figure 7-9 Thickness comparisons between simulation and experiment along the cross-section of AA5083 part after superplastic-like forming at 400ºC.

Table 7-3 Comparisons between simulation and experiment results at 400ºC

Parameters	Draw-in length	Bulge height	Minimum thickness
Experiment	14.5 mm in a quarter sheet	57 mm	1.8 mm
Simulation	15.2 mm	55.7 mm	2.05 mm

The calculated maximum bulge heights of the formed part are summarized in Table 7-3, and it figures that there is about a deviation of 3% between the simulation and experiment. In comparison with the material draw-in level, they also show good agreements with each other. The overall match of the predictions corresponding to the experiment at 400ºC is good, except that the over-predicted thickness gradients at low arc length (< 30 mm).

7.3.3   Equivalent Von Mises Stress

Figure 7-10 provides the equivalent Von Mises stress computed for the formed part at three different junctions during gas forming. Zones experiencing high stress are mainly present in the areas where the punch is directly in contact with the forming sheet, see Figure 7-10(a). The higher stress concentration in the part can result in a higher strain rate at the same area. The stress-state difference between the inward and outward part radii in Figure 7-10(b) and (c) is approximately equivalent of the deformation strain rate in Figure 7-11(b) and (c), respectively.

Additionally, simulation results have demonstrated that stress concentration of the areas in contact with the punch and die radii is mainly ascribed to the local geometric inhomogeneity. Therefore, the stress gradient of the sheet caused a more rapid thinning rate at these zones. It is expected that the deformation rate difference will accelerate as forming proceeded, leading to thickness variations and localized thinning in the formed part.
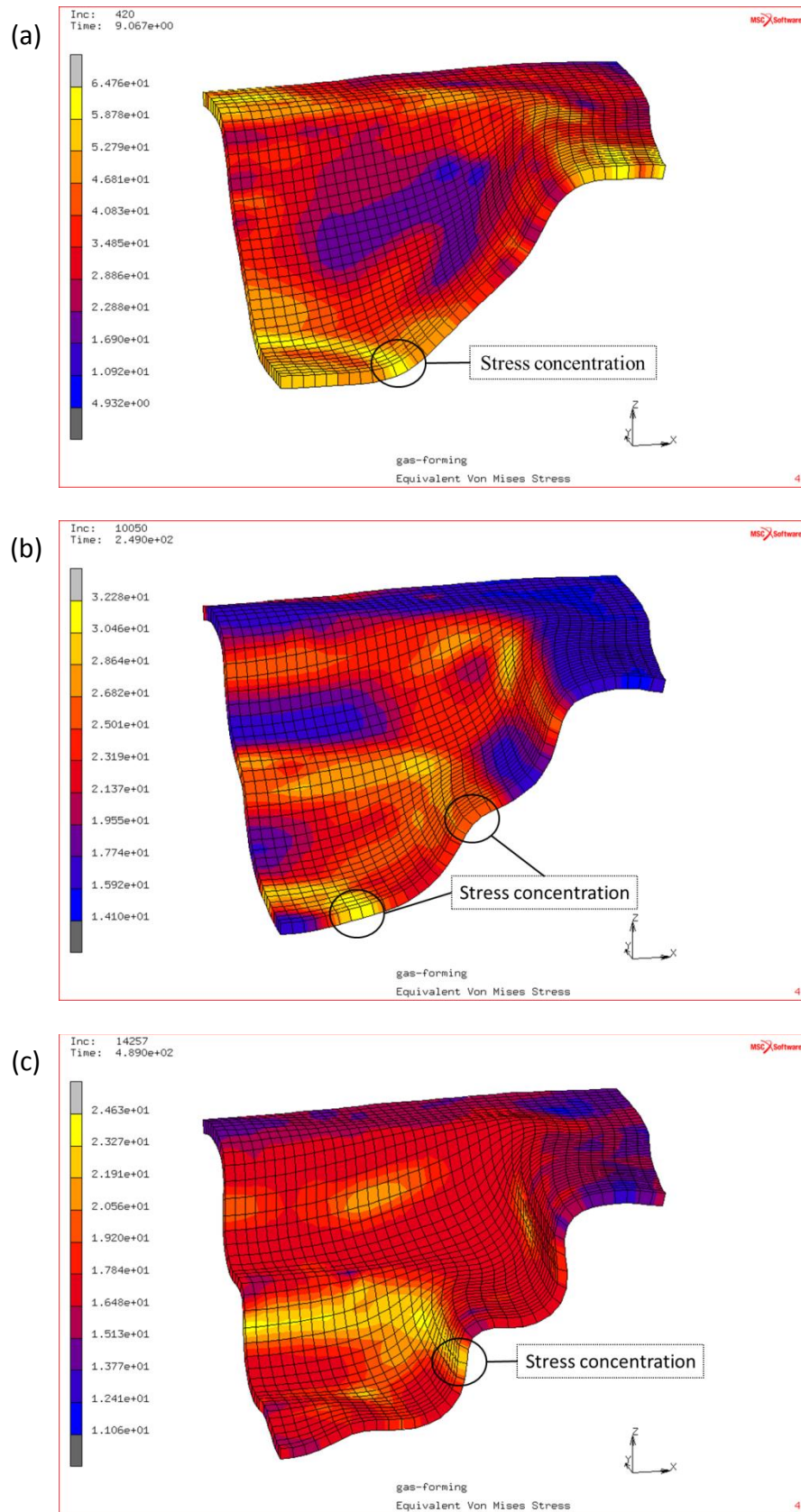
Figure 7-10 The contours of equivalent Von Mises stress in MPa (a) at the beginning of gas forming, (b) in the course of gas forming and (c) at the end of gas forming.

7.3.4   Equivalent Plastic Deformation Strain Rate

Figure 7-11 shows the deformation status of the metal sheet at three different junctions in the course of the entire forming process. The contour bands represent the magnitude of equivalent plastic strain rate. Although the gas pressure was applied according to the cycle presented in presented in Figure 3-9, it can be seen that the equivalent strain rate is not uniformly distributed over the entire sheet. This is due to the die geometry and loading features; it is often not possible to maintain the constant strain rate over the entire component [242].

Prior to gas forming, the material was drawn down by the moving punch in the hot drawing stage. In this stage, there were some initially localized thinning areas where the punch was directly in contact with the sheet. After imposing gas on the sheet, zones of the highest forming strain rate are found in these areas, as shown in Figure 7-11(a). When the material makes contact with the inner shoulders of the die, Figure 7-11(b), the material in that region is locked because of the interactions between the part geometry and the tool. The sheet forming mainly occurs near the area where the material is in contact with the die wall. Consequently, localized thinning is most likely to take place during this stage due to stretching between the locked sheet and flowing material.

The outward corners, as indicated in Figure 7-11(c), are the last part to be filled and the material in these areas remains being formed at low strain rates, even to the end of the process. As a result, the percentage thinning there is smaller, see Figure 7-7(b), as compared to the other deformation areas.
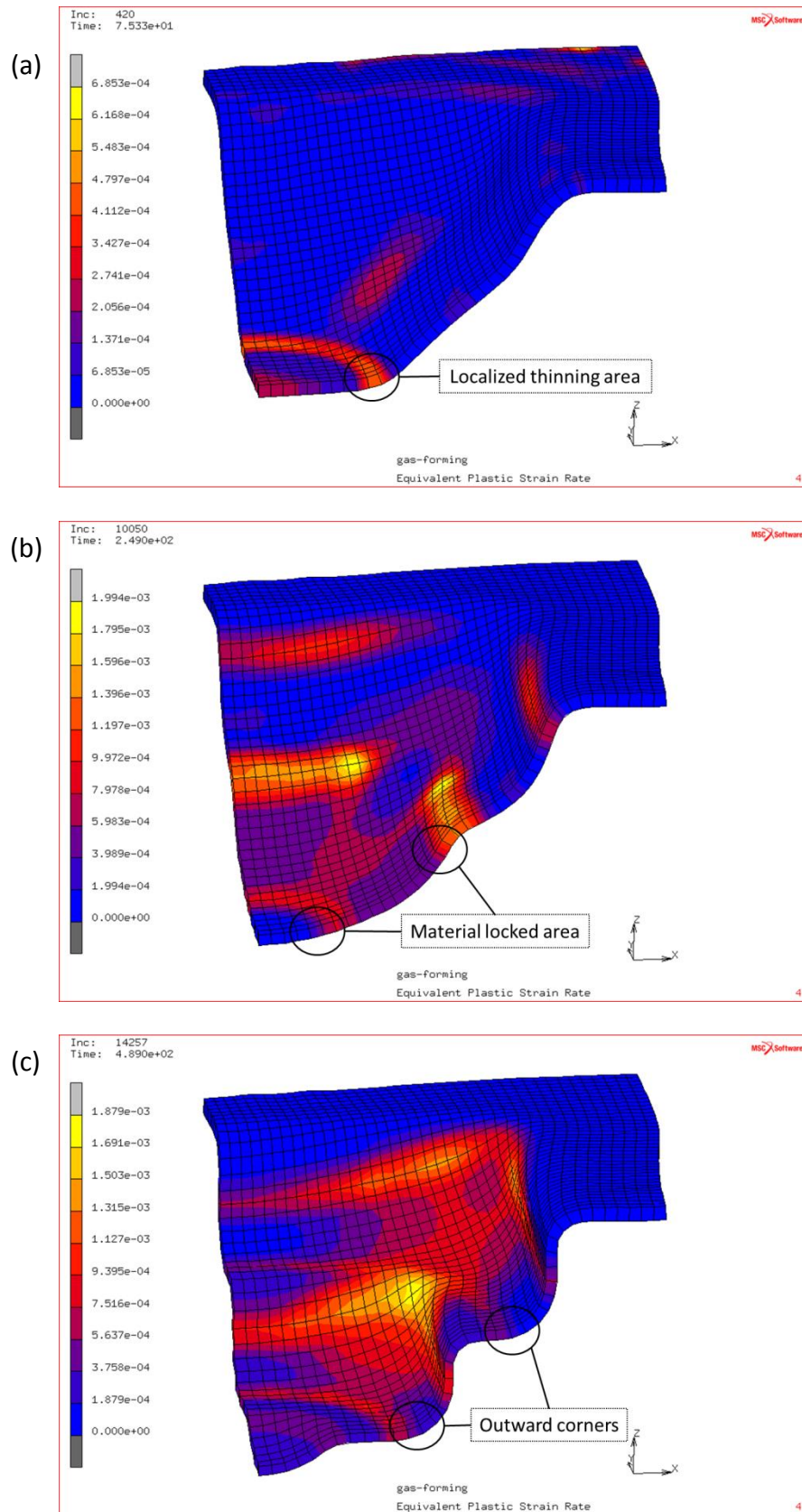
Figure 7-11 The contours of equivalent plastic strain rate (unit: s⁻¹) (a) at the beginning of gas forming, (b) in the course of gas forming and (c) at the end of gas forming.

7.3.5   Validation of the Model at 500ºC

The dislocation density model was further used during the validation simulation at 500ºC. The comparisons of thickness profiles between the simulations and the experiments are plotted in Figure 7-12. There exit two computed thickness reduction locations, in which the minimum thickness in this section is computed to be 2.0 mm.
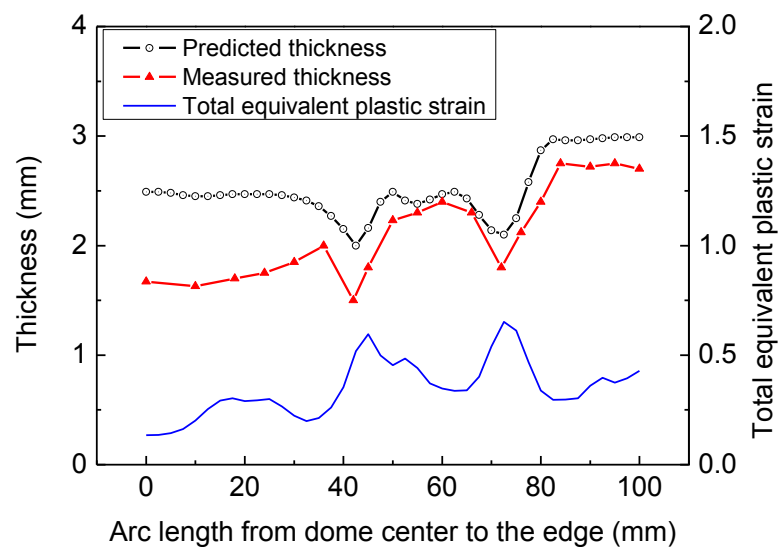
Figure 7-12 Thickness comparisons between simulation and experiment along the cross-section of AA5083 part after superplastic-like forming at 500ºC.

The corresponding location with maximum thinning has a measured thickness of 1.5 mm. As discussed at 400ºC, stretching when the moving punch comes into contact with the workpiece during hot drawing and geometric effects between the sheet and hot die surface during gas forming are two of the main reasons that account for the thickness reduction at the two locations. In addition, aluminum alloys underwent major microstructural changes during hot forming, especially above 500ºC. The

microstructural features of recrystallization, grain growth and cavitation are other reasons that have influenced the high-temperature formability, and therefore, may cause the deviation.

Table 7-4 lists the detailed comparisons between simulation and experiment performed at 500ºC. The variations of material draw-in length and bulging height between the simulation and experiment are within 7%. The simulation did not capture the full extent of boundary conditions. The simulation predicted the entire forming process at 500ºC with fairly good agreement with experiment, especially to illustrate the localized thinning locations.

Table 7-4 Comparisons between simulation and experiment results at 500ºC.

Parameters	Draw-in length	Bulge height	Minimum thickness
Experiment	14.5 mm	58 mm	1.5 mm
Simulation	15.8 mm	55 mm	2.0 mm

7.4 DISCUSSION

7.4.1 Microstructure Features

In this study, the material model assumes a dislocation glide mechanism with hardening and recovery contributions. This may not always be valid, especially at extreme temperatures, where dynamic recrystallization may occur during hot

deformation. On the basis of microstructure evolution (*Section* 6.2.3) and hardness discussion (*Section* 6.4.2), the occurrence of a limited amount of recrystallization was evidenced. Because of grain growth after deformation, the grown grains with high aspect ratios are responsible to the decrease of hardness as well.

Dynamic recrystallization as well as grain growth was neglected, and the model is aimed at expressing the material deformation from room temperature up to high temperatures for aluminum alloys. In particular, the superplastic-like forming process is looking at ways of expanding the use of sheet forming for faster forming times and lower temperatures (e.g. warm working condition is preferable). In spite of the limitations above, application of the model to various conditions with a set of intrinsic parameters is suitable to account for low-temperature as well as high-temperature plasticity against various strain rates.

7.4.2   Boundary Conditions

The actual differences in set-up and boundary conditions explain the deviation in thickness gradients between experiments and simulations in the sheet center region (arc length < 30 mm). Figure 7-13(a) shows the cross-sectional illustration at the end of hot drawing. It also represents the beginning of gas forming, during which the argon gas is introduced via the gas inlet onto the sheet surface.

According to the experimental route, the assembly temperature, i.e. punch and die temperature, is preset at 400 or 500ºC depending on the forming condition. In reality, the die is in contact with the sheet at the edge rather than the center leading to temperature variations across the plate in the pre-heating stage. During hot drawing, the sheet center region is heated due to the heat conduction from the hot punch nose to

the sheet, gradually leading to a higher temperature at the punch contact region, as indicated in Figure 7-13(a). The punch contact region corresponds to the sheet center region, which is within the arc length of 30 mm. The temperature gradients would cause strength inhomogeneity in the forming sheet.
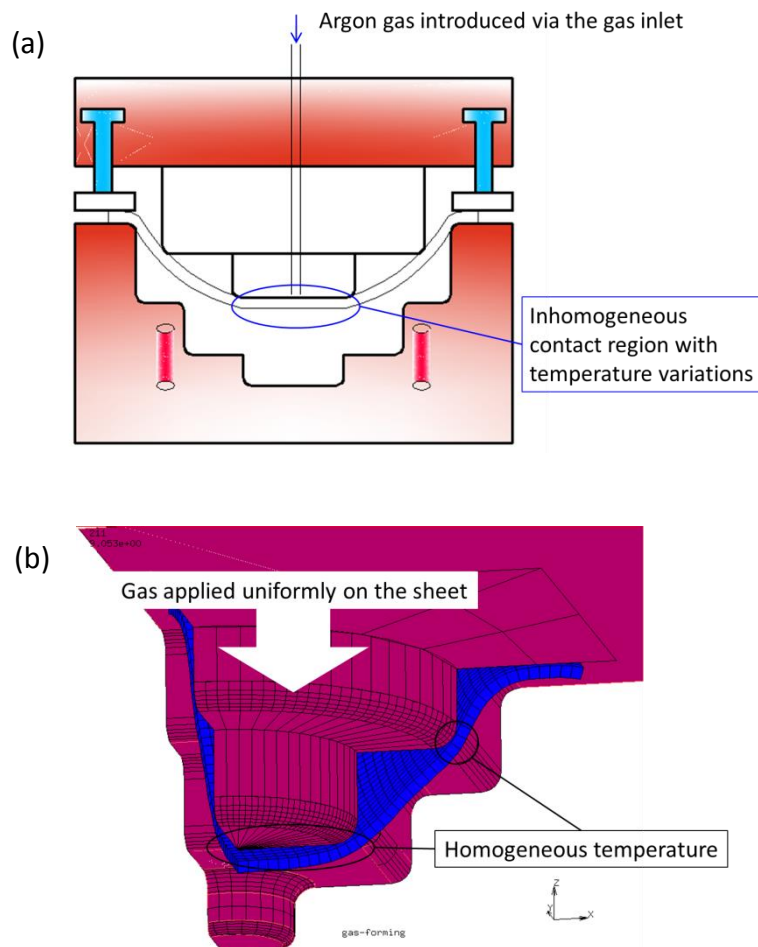
Figure 7-13 Schematic of temperature and pressure homogeneity at the end of hot drawing: (a) experiment and (b) simulation.

Additionally, the gas pressure was initially imposed via the gas inlet only on the punch contact region with high temperature, which would result in a rapid strain (thinning)

rate at the sheet center. Therefore, the inhomogeneity of the temperature (non-isothermal heating) and pressure developed directly into thickness gradients. However, this is not reflected in the simulations as can be seen through the thickness predictions which start to deviate from the dome center to the arc length of approximately 30 mm in Figures 7-9 and 7-12.

Another important cause for the deviation is the finite element discretization. At the center of the model, where the die has a sharp curvature, more elements are really needed to describe the geometry correctly. However, the thick shell element formulation used requires a certain aspect ratio between the thickness of the element and the sides of the element to work well. Increasing the number of elements has the side effect of making this aspect ratio worse. An option could be to use solid elements instead of solid shell elements. But then it would be necessary to use four or more elements over the thickness of the plate to describe the bending accurately. Considering that the aspect ratio of solid elements should not be too large, it would make the model too large to handle on the available computing resources. Therefore, it was not investigated.

As a convenient and efficiency method, FEM is usually adopted to facilitate the industry applications. The present theoretical approach is able to represent deformation behavior at various strain rates simultaneously under the same temperature. This is useful and often necessary in forming of complex-shaped parts, since there exist strain rate variations ascribed to geometric inhomogeneity. The results in this study for predicting the localized necking areas are consistent with experimental measurements, illustrating that critical attention should be paid to these areas with respect to the process/die design.

7.5 SUMMARY

The physical material model based on the evolution of immobile dislocation density and excess vacancy concentration was constructed in the description of AA5083 deformation behavior from ambient temperature up to 550ºC and strain rates from 10^{-4} up to 10^{-1} s^{-1}. Simulations of the superplastic-like forming process are promising, and match the experimental measurements when integrating the dislocation density model. The conclusions are summarized below.

1. The flow stress model based on the concept of dislocation density has been used for the first time in sheet forming of AA5083 sheets at different temperatures. It was validated to account for the high-temperature plastic behavior in multi-scale computations.

2. The main operating mechanisms, i.e. dislocation creep with hardening and recovery contributions, required the use of temperature and strain-rate dependent coefficients in the short-range term of the used model.

3. When the sheet was initially in contact with the punch, the material was stretched by the moving punch, resulting in some thickness reduction. Simulations show the large plastic strain areas with corresponding thickness variations obtained in the formed part.

4. The differences in stress distribution between the inward and outward corners of the sheet are ascribed to the local geometric inhomogeneity, and therefore, lead to variations in sheet strain rate. The strain rate variations during gas forming developed gradually into thickness gradients.

CHAPTER 8 SUPERPLASTIC-LIKE FORMING OF

Ti-6Al-4V ALLOY

Titanium alloys are sensitive to oxidation during high-temperature deformation. Therefore, lowering the forming temperature and increasing the forming rate are significant to accelerate productivity and make the superplastic-like forming process viable for higher production efficiency and better post-forming properties. This chapter sought to expand the advantages of the technology to the forming of Ti-6Al-4V alloy. The experimental measurements, such as (i) pressure cycle, (ii) material draw-in, (iii) bulge height, (iv) thickness reduction and (v) oxidation behavior were evaluated to justify the quality of the formed Ti-6Al-4V part.

8.1 MATERIAL PROPERTIES

Since material is introduced into the deformation area during forming, a thinner gauge of the sheet can be used. As a result, the part will be lighter with minimum material weight and more material can be saved.

In this case, Ti-6Al-4V alloy sheets with thickness of 1.6 mm were used. The forming temperature needs to be determined so that the sheet material is formed properly by the limited gas pressure. Uniaxial tensile tests were carried out at the temperatures ranging from 750ºC to 850ºC to investigate the high-temperature properties with the initial strain rates ranging from 10^{-3} to 10^{-1} s^{-1}.
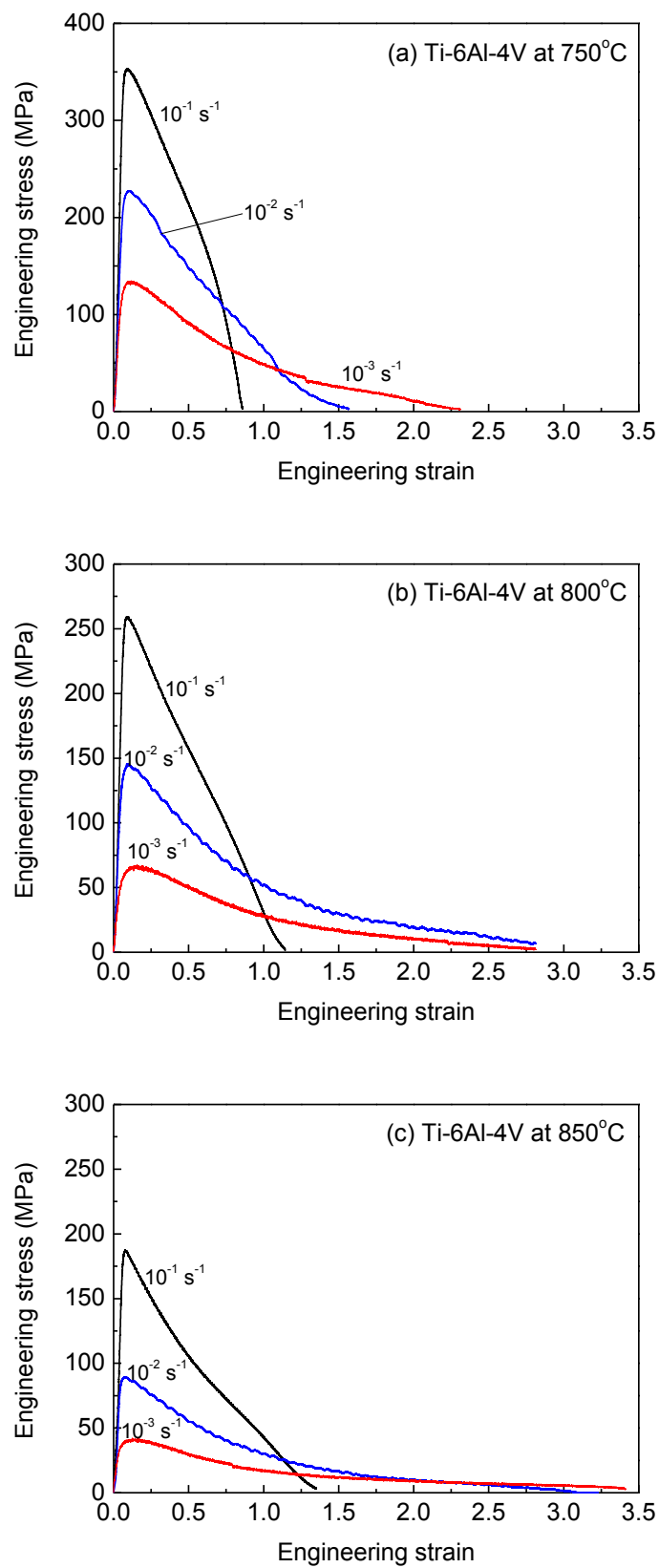
Figure 8-1 Engineering stress – engineering strain curves for Ti-6Al-4V alloy at (a) 750 ℃, (b) 800 ℃ and (c) 850 ℃.

It is revealed that the alloy has a reasonable flow stress of 65 MPa during tensile testing at 800ºC and a strain rate of 10^{-3} s^{-1}, as shown in Figure 8-1(b). Therefore, the forming of this alloy can be carried out under this condition. Although, it has a lower flow stress at a higher temperature, such as 40 MPa at 850ºC, another goal of the process is to minimize the forming temperature but to meet a good material integrity as well. In addition to flow stress, the tensile elongation is another criterion that is used to determine the optimal forming condition. As shown in Figure 8-2, Ti-6Al-4V alloy has percent elongation-to-failure of 300% at 800ºC when tested at a strain rate of 10^{-3} s^{-1}.
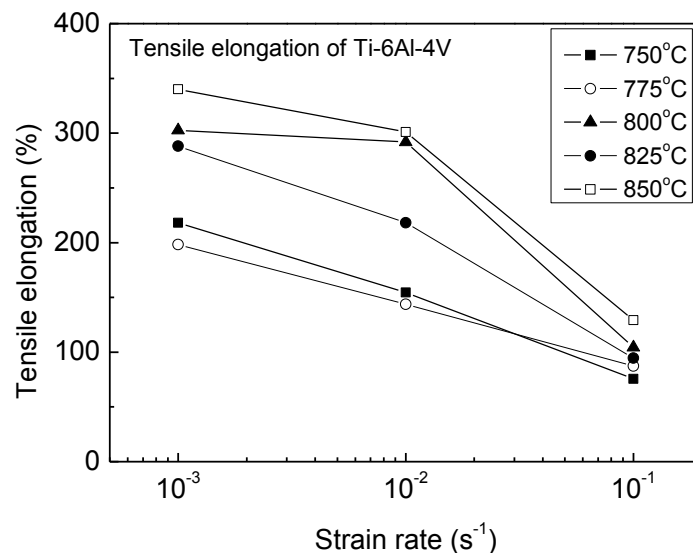
Figure 8-2 Tensile percent elongation-to-failure as a function of strain rate for Ti-6Al-4V alloy.

8.2   HOT DRAWING OF Ti-6Al-4V ALLOY

During hot drawing, the amount of material draw-in is associated with the drawing temperature and the initial sheet size. Table 8-1 lists the material draw-in length dependent on the initial sheet size.

153

Table 8-1 Material draw-in length of Ti-6Al-4V alloy dependent on the initial sheet size.

Drawing temperature (ºC)	Sheet size (mm^2)	Draw-in Length (mm)	Remarks
800	180×180	38	Good
800	190×190	36	Good
800	200×200	35	Good
800	210×210	32	Good
800	220×220	30	Good
800	230×230	nil	Ruptured
800	240×240	nil	Ruptured

The material draw-in as a function of initial sheet width is also plotted in Figure 8-3. The scattered points represent the experimental data obtained at 800ºC, while the straight line is a linear fitting of those data for determining the material draw-in gradients. The drawing limit zone for the hot drawing of Ti-6Al-4V alloy sheet is therefore shown, as indicated in Figure 8-3, where the draw-in amounts associated with the initial sheet size are visible from the predicted lines as well. The linear relationship at 800ºC can be represented by Eq. (8-1).

$$L_D = 75 - 0.2W_o \qquad\qquad \text{Eq. (8-1)}$$

According to the calculation method discussed in *Section* 5.2.1, the minimum sheet width was calculated to be 200 mm. Therefore, based on the existing die set, the initial sheet size with an additional sheet metal allowance for a good sealing condition was determined to be 210×210 mm^2.
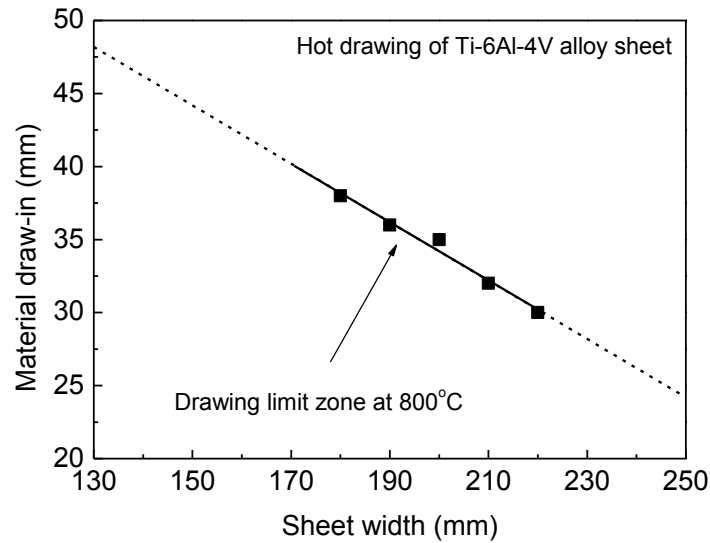
Figure 8-3 Material draw-in as a function of initial sheet width for Ti-6Al-4V alloy. The drawing limit zone for hot drawing at 800 ℃ is also plotted by the solid line.

8.3   GAS FORMING OF Ti-6Al-4V ALLOY

8.3.1   Determination of Pressure Profile

The whole die se was initially heated up to the operating temperature (750, 800 and 825ºC respectively). The non-isothermal heating system made the local temperature at the die radii, as the locations in Figure 3-6(a), to be 770, 820 and 845ºC, respectively.

Based on the tensile stress – strain curves, Ti-6Al-4V alloy has good formability with reasonable flow stress (65 MPa) at 800ºC and a strain rate of 10^{-3} s^{-1}. The pressure – time (in minute) cycle, which was input into the forming press, was predicted from finite element method (similar to Figure 3-9) to maintain the sheet to be formed at a target forming strain rate of 10^{-3} s^{-1}, as plotted in Figure 8-4.
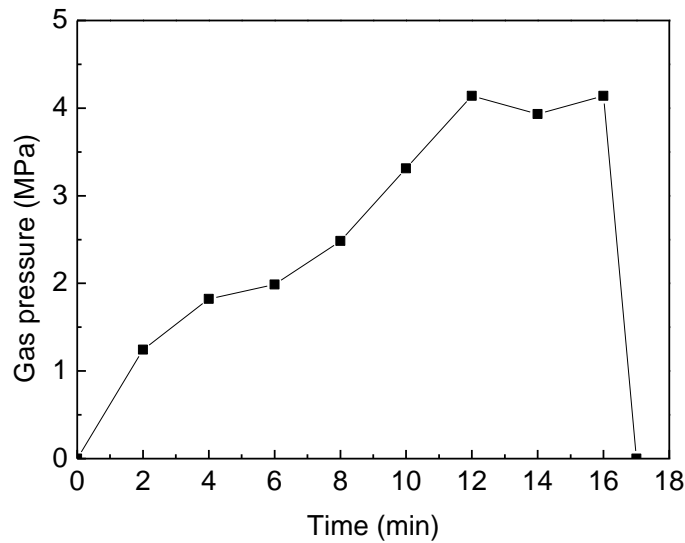
Figure 8-4 Pressure cycle predicted by FEM for gas forming of the pre-formed Ti-6Al-4V sheets at 800 ℃ and a target strain rate of 10^{-3} s^{-1}.

8.3.2   Bulge Height

Figure 8-5 shows the bulge profiles of formed Ti-6Al-4V parts against different forming temperatures. As the operating temperature increases from 750 to 825ºC, the bulge height increases from 50 to 57 mm. it appears that Ti-6Al-4V sheet is partially forming at 750ºC by the maximum applied gas pressure of 4.2 MPa.

750°C   800°C   825°C
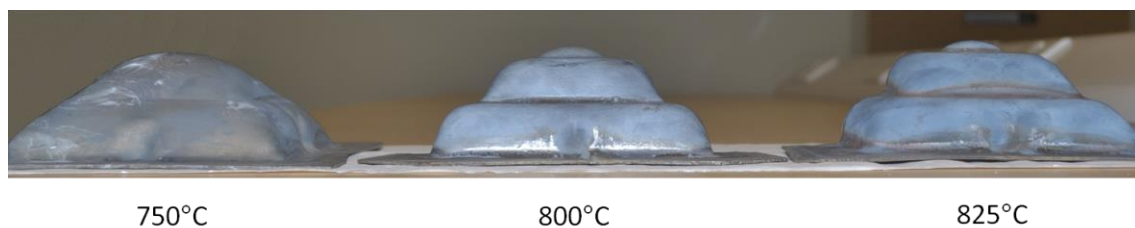
Figure 8-5 Bulge profiles of formed Ti-6Al-4V parts at different forming temperatures.

The isothermal (constant temperature) forming has been carried out to compare with the non-isothermal forming. The final bulge heights show a variation of 1 – 3 mm. The increased bulge heights under non-isothermal conditions may be due to a better flowability arising from the localized higher temperature. For the non-isothermal forming, the higher bulge height means a better formed part with greater completion and results in a small amount of decrease (0.1 – 0.2 mm) in the minimum thickness.

The cross-sections of the formed Ti-6Al-4V parts at 800ºC and different forming junctions were observed to profile the bulge shapes. The profiles of the formed parts at three junctions, i.e. (a) hot drawing, (b) 2.1 MPa pressure forming and (c) completion of gas forming are shown in Figure 8-6.
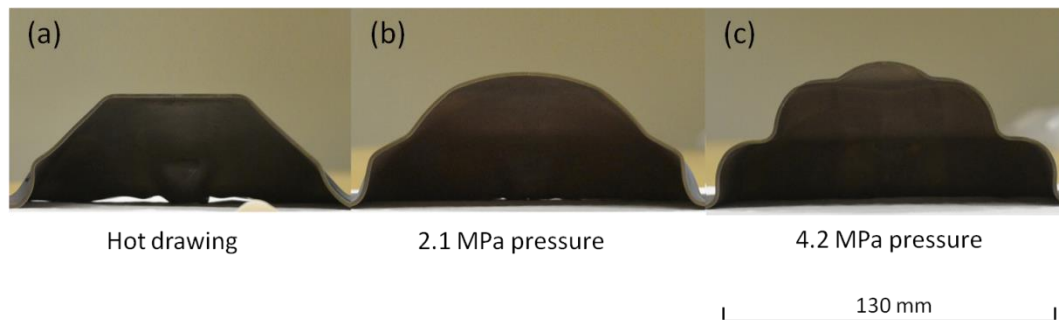
Figure 8-6 Bulge-height profiles of formed Ti-6Al-4V parts with different junctions at 800 ℃: (a) hot drawing, (b) 2.1 MPa pressure and (c) completion of gas forming.

When the gas pressure reaches 2.1 MPa during gas forming, the bulge height was measured to be 49 mm. After completion of gas forming at the maximum pressure of 4.2 MPa, the part is further formed to reach a maximum bulge height of 56 mm in the end. Accordingly, an approximate surface expansion of 130% for the Ti-6Al-4V sheet

is achieved at 800ºC, as compared to that of 137% for AA5083 at 400ºC. The reduced global temperature (from 900ºC for conventional SPF to 800ºC) and the increased local temperature (820ºC) have ensured the sheet being successfully formed with a reasonable completion.

8.3.3 Surface Finish

Figure 8-7 shows the surface finish of formed Ti-6Al-4V parts from 750 to 825ºC. The surface is shining with little oxidation found on the sheet surface at 750º. The surface of the part formed at 800ºC is darker as compared to the one at 750ºC. A little oxidation formed on the bare sheet at 800ºC. When the forming process was carried out at 825ºC, more oxide film appeared on the sheet showing a darker surface finish, as indicated in Figure 8-7.

750°C   800°C   825°C
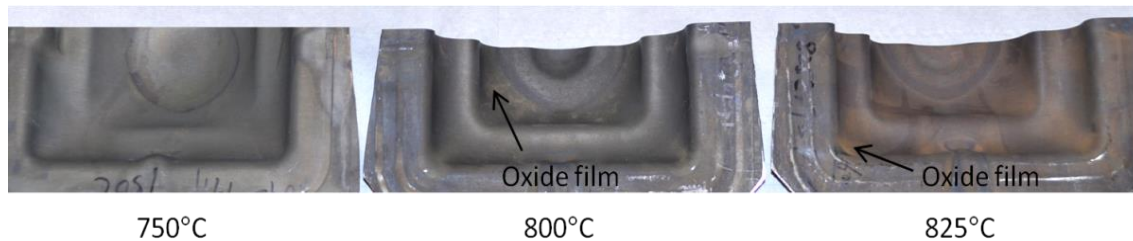
Figure 8-7 Surface finish of superplastic-like formed Ti-6Al-4V parts at different operating temperatures.

As the forming temperature increases, it influences the material integrity due to the occurrence of oxidation or microstructural defects. In order to meet the goal to minimize the temperature during forming at the lowest possible level, the optimal

temperature of forming Ti-6Al-4V is prescribed to be 800ºC after laboratory testing. Meanwhile, the local temperature of 820ºC at the designed corner radii is therefore used to incorporate a non-isothermal heating system.

8.3.4   Thickness Distributions

The sheet was almost fully formed without any macro (or visible) fracture on the surface by hot drawing and subsequent gas forming at 800ºC. Thicknesses were measured from the dome center to the edge along the cross-section. Each measurement (an average of three trials) was named from location #1 to #11, as labeled in Figure 8-8. The thickness profile is plotted in Figure 8-9, showing a localized thickness reduction at location #4. The maximum percentage thinning here is 54%.
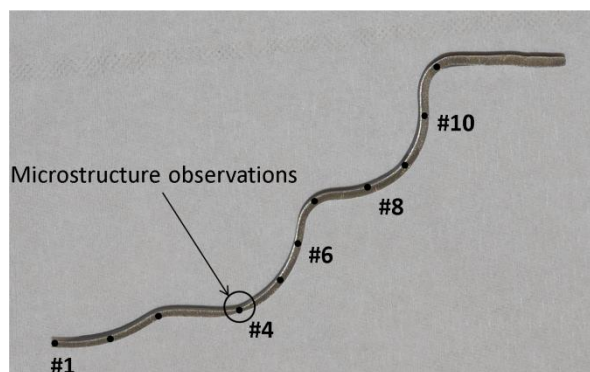
Figure 8-8 Cross-section of Ti-6Al-4V part formed at 800 ℃ for thickness measurements and microstructure observations.

The thickness reduction at location #4 was influenced by the forming process, in which the sheet initially came into contact with the punch nose during hot drawing.

Consequently, material adjacent to this area was then locked against the die surface by friction and gas pressure. The geometric inhomogeneity led to strain rate gradients during gas forming and developed gradually into thickness variations. As a result, localized necking occurred near the outward radius (location #4).
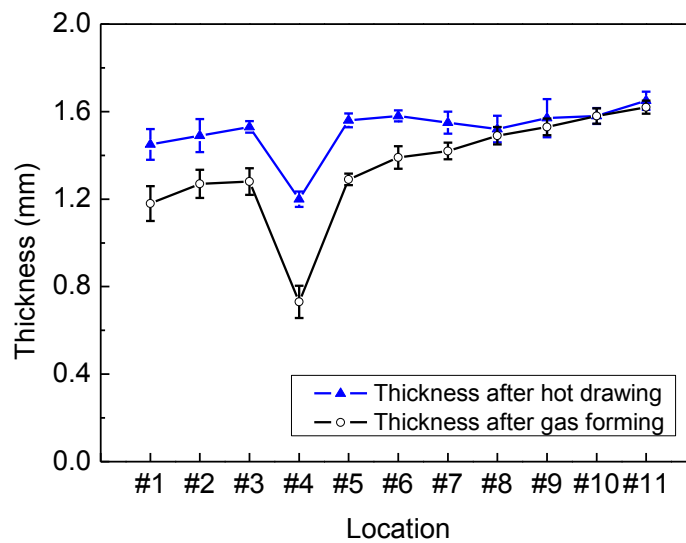
Figure 8-9 Thickness distributions for Ti-6Al-4V formed at 800 ℃ after two forming stages.

8.4   MICROSTRUCTURE OF Ti-6Al-4V ALLOY

8.4.1   Microstructural Defects

The microstructural defects in the as-received and deformed samples were examined by optical microscopy. The microstructure of the as-received Ti-6Al-4V sheet cross-section is shown in Figure 3-1(b). In the micrograph, the grain structure is not homogeneous showing various grain shapes. No obvious microstructural defect can be found on the alloy surface.

The deformed specimens after hot drawing and gas forming were sectioned from the localized thinning area (location #4 in Figure 8-8). After hot drawing, there were some micro-cracks found on the alloy surface. Figure 8-10 is the hot-drawn specimen showing that the cracks have penetrated about 5 μm into the thickness. The stretching stress induced when the moving punch made contact with the sheet during hot drawing would explain why cracks occurred on the sheet surface. No oxide layer is clearly visible on the formed sheet surface.
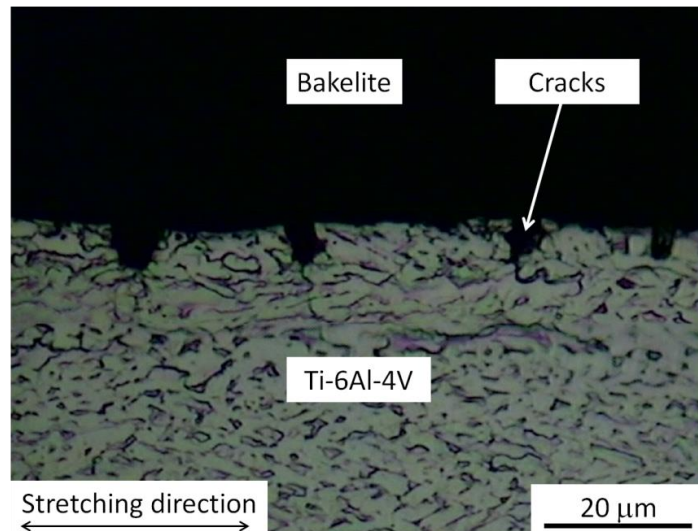
Figure 8-10 Optical micrograph of pre-formed Ti-6Al-4V sheet cross-section during hot drawing at 800 ℃.

Gas blow forming follows the hot drawing operation to complete the superplastic-like forming of Ti-6Al-4V alloy. Figure 8-11 shows the cross-section of the deformed sheet with a layer of oxide film on the specimen surface. The average thickness of oxide film was measured to be 5 μm after forming at 800 ℃.
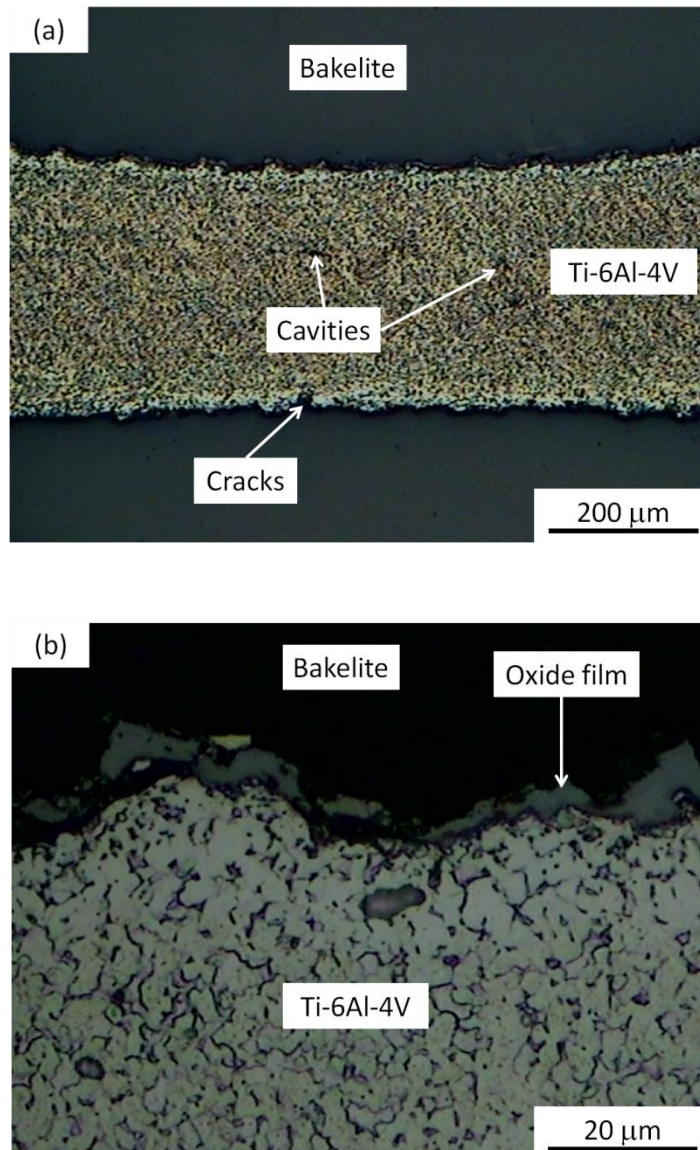
Figure 8-11 Optical micrographs of formed Ti-6Al-4V sheet cross-section at location #4 after completion of superplastic-like forming at 800 ℃: (a) low magnification and (b) high magnification.

Cracks which formed during hot drawing retained on the part surface with a layer of oxide film overlaid. The cracks could extend during gas forming as local tensile stress was present along the horizontal direction (Figure 8-11). The penetration of the cracks introduced oxidation into the thickness which would accelerate thickness reduction at

this location. It is also clear that there are few cavities (micro-voids) found in the formed sample (Figure 8-11(a)), though in limited number. Those cavities may exist in the raw material before fabrication (rolling) in factory. They could coalesce and became visible after deformation.

8.4.2 Oxidation Behavior

It is well known that oxidation happens on the surface of Ti-6Al-4V alloy above 650ºC [117]. It is accepted that the oxidation of Ti-6Al-4V alloy follows a parabolic rate law and that a higher reaction temperature and a longer exposure time in air can lead to more oxidation in terms of weight gain. The weight gain for Ti-6Al-4V alloy oxidized in air at 800ºC for 16 min is about 1.2 mg/cm^2 [117].
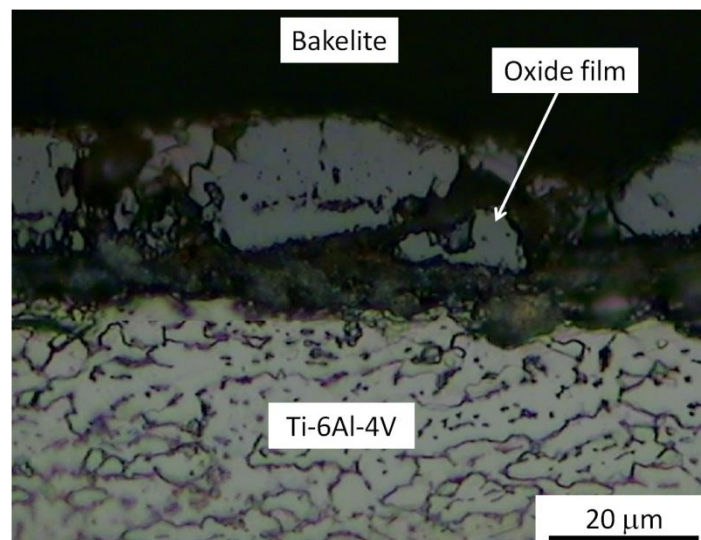
Figure 8-12 Optical micrograph of Ti-6Al-4V sheet cross-section after air oxidation at 900 ℃ for 16 min.

Conventional superplastic forming of Ti-6Al-4V alloy is usually carried out above 900ºC [8, 93, 109, 243]. For comparison with the oxidation behavior between the conventional SPF and superplastic-like forming, Figure 8-12 presents the optical micrograph of the Ti-6Al-4V sheet cross-section after oxidation at 900ºC for 16 min. A greater oxidation behavior with a corresponding weight gain of 2 mg/cm^2 was measured at 900ºC. It is clear that a thick layer of oxide film is found on the sheet surface. The average thickness of the oxide film was measured to be 25 μm, as compared to that of 5 μm at 800ºC in Figure 8-11(b).

Figure 8-13(a) shows the clefts of oxide film formed approximately perpendicular to the stretching direction during superplastic-like forming at 800ºC. The clefts tend to propagate across the sheet surface. As shown in Figure 8-13(b), the cleft penetrates further into the material, and it can result in more oxidation of the parent material as the forming process proceeded. The oxide film formed at elevated temperature is not dense. Inspection at a higher magnification shows that the oxide film comprises many oxide particles. Eventually, the ductility may be reduced due to less supporting cross-section of the material, leading to a structural imperfection (lowering of the overall ductility).

In order to obtain a better understanding of the oxidation in the material, the oxide film that formed at 800ºC was further examined by X-ray diffraction (XRD). Figure 8-14 shows the XRD analysis of the oxide film on the Ti-6Al-4V sheet surface after completion of superplastic-like forming. From the diffraction pattern, the oxide is mostly identified as TiO$_2$.
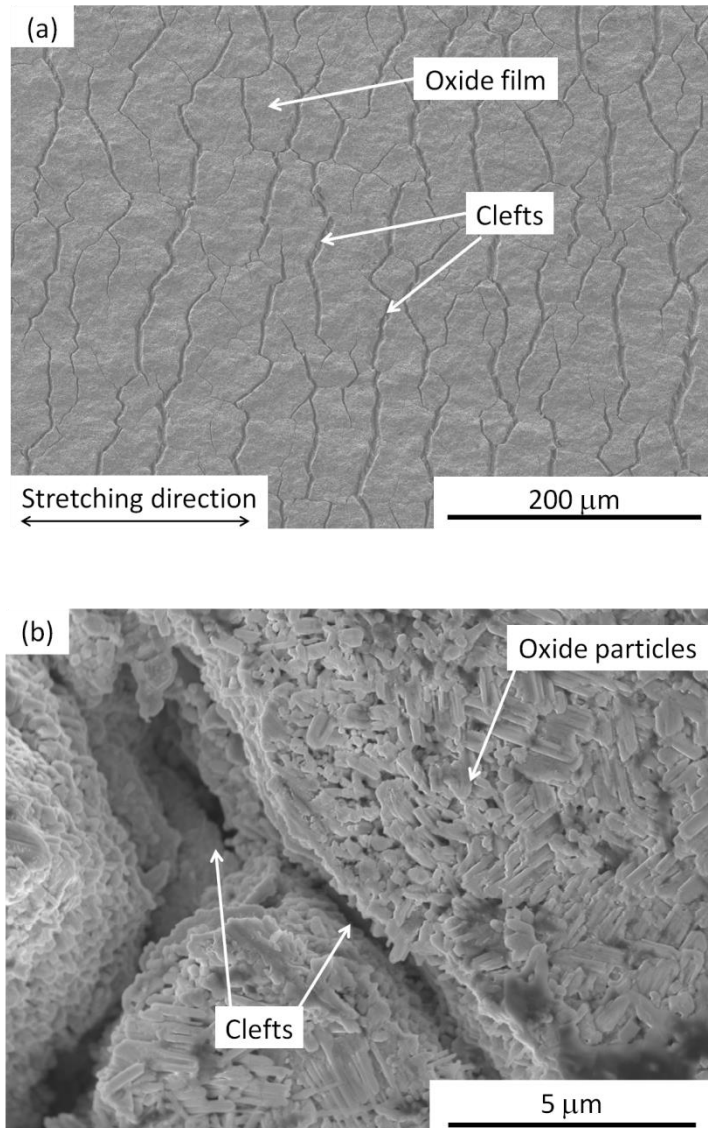
Figure 8-13 Clefts on the surface of the TiO$_2$ oxide film formed at 800 ℃: (a) low magnification and (b) high magnification.

The higher the forming temperature or the longer the forming time, the thicker the oxide film and the weaker material formability [117]. Accordingly, a faster-speed forming that can form the sheet metals, especially for titanium alloys, at a lower temperature, is of great importance. It would weaken the negative influences of long forming time and high heating temperature on material properties during forming. By

165

comparing superplastic-like forming (800 ℃) and conventional SPF (> 900 ℃), the major advantages for superplastic-like forming is the lower forming temperature and shorter forming time that would lead to a lower oxidation rate. In this case, the superplastic-like forming process meets the requirements (e.g. fast forming and less oxidation) of manufacturing complex-shaped components very well.
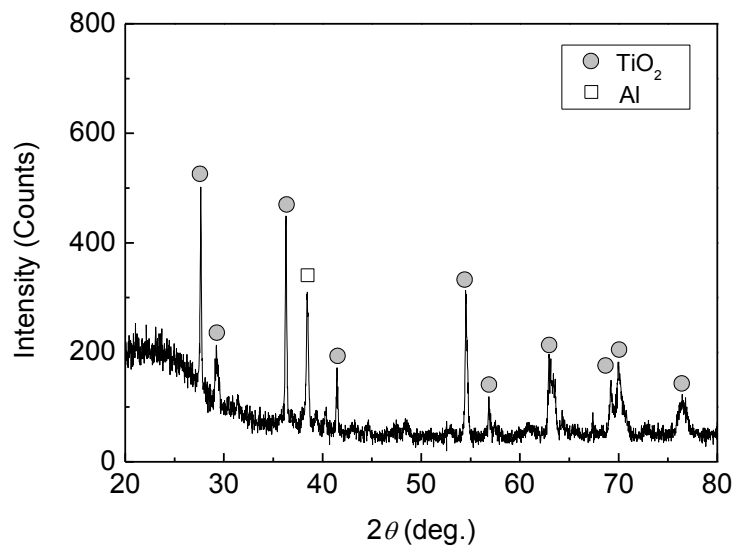
Figure 8-14 XRD pattern of the oxide film on Ti-6Al-4V alloy formed at 800 ℃.

8.4.3 Microstructure Evolution

Microstructure evolution in terms of the grain orientation maps are examined by EBSD. The specimens used for EBSD mapping were cross-sectioned from the parent and formed parts. The maximum sheet thinning after deformation occurred in the vicinity of location #4. The microstructures before and after superplastic-like forming were then observed at this location. The EBSD orientation maps of the grains in different forming stages, i.e. as-received, hot drawing and gas forming are shown in

Figure 8-15(a), (b) and (c), respectively.
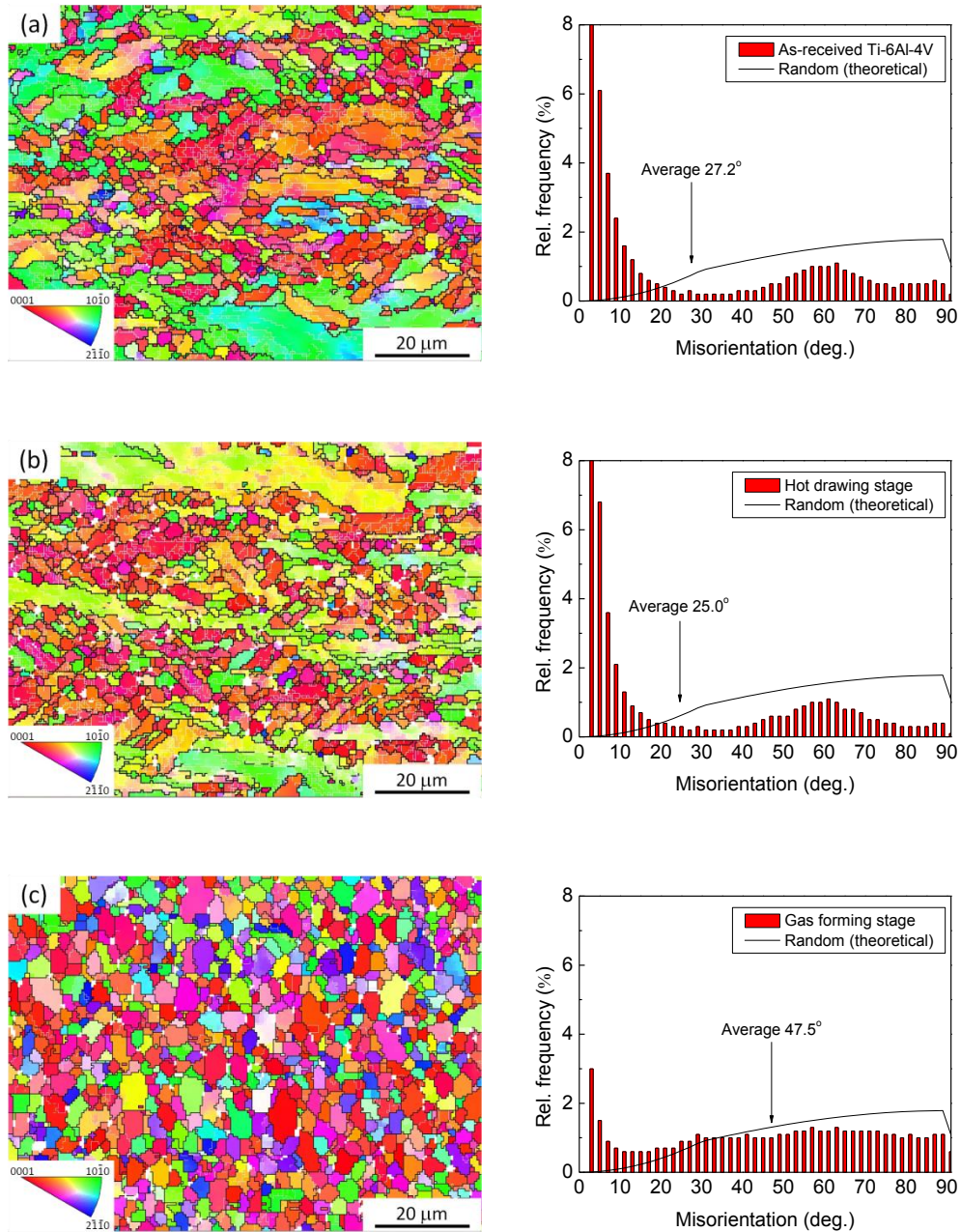
Figure 8-15 EBSD maps of Ti-6Al-4V grains formed at 800ºC and different stages: (a) as-received material, (b) hot drawing stage and (c) after completion of superplastic-like forming. The maps were observed from identical location #4 in the formed parts.

As compared to the grain shape of the parent material (Figure 8-15(a)), some fine equiaxed grains after hot drawing (Figure 8-15(b)) were newly found located near the deformed big grains, possibly as a result of dynamic recrystallization. The recrystallization during hot drawing is not extensive. The misorientation histograms of as-received and hot-drawn specimens show a large number of low angle grain boundaries (LAGBs) with misorientation below 15º. The distribution of the high angle grain boundaries (HAGBs) is not homogeneous over the microstructures, with the HAGBs mostly located in the fine grain regions near the misorientation angle of 60º. The overall boundary angle distributions remained similar before and after hot drawing. This implies that the material incurred little subgrain boundary migration or subgrain rotation during hot drawing.

The grain structure seems more random distributed after completion of superplastic-like forming, as shown in Figure 8-15(c). The average misorientation angle and the fraction of HAGBs were calculated to be 47.5º and 84%, respectively, and close to 60º and 98% for the random misorientation distribution as predicted by Mackenzie [202]. The increased amount of HAGBs is attributed to the newly recrystallized grains. In the gas forming stage, recrystallization extensively dominated and subsequently produced a mass of new grains with HAGB misorientation. This also explains the decreased fraction of LAGBs after gas forming.

Table 8-2 summarizes the grain structures obtained from EBSD analysis. Due to both occurrences of elongated and recrystallized grains during hot drawing, the structural information has not shown much variation from the view of statistics as compared to that in the as-received condition. As gas forming proceeded, the microstructure was characterized by randomly distributed equiaxed grains (average aspect ratio = 1.5) with

a mean grain size of 2.8 μm. Fairly uniform microstructure can be achieved with this

forming technique. The increased HAGBs and reduced aspect ratio have revealed that

the main microstructural mechanism of Ti-6Al-4V alloy during gas forming is

recrystallization.

Table 8-2 Summary of Ti-6Al-4V grain structures obtained from EBSD analysis.

Material	Mean grain size (μm)	Fraction of HAGBs	Average aspect ratio
As-received	3.4	41%	1.9
Hot drawing	3.1	39%	1.8
Gas forming	2.8	84%	1.5

8.5 SUMMARY

As compared to conventional SPF, the optimized superplastic-like forming expands the

advantages of this technology to the forming of Ti-6Al-4V alloy at lower temperatures.

The optimal forming temperature is 800ºC. The non-isothermal heating system is used

to improve the formability at critical areas during forming. The conclusions can be

made as follows:

1. The minimum thickness was found at the areas adjacent to the outward corners;

    and the maximum percentage thinning was 54%. The stress concentration due

    to geometric inhomogeneity at these locations is known to give rise to

    thickness variations in terms of localized thinning.

2. Microstructural defects during blow forming, i.e. cracks and oxide film on the part surfaces, are the other sources responsible for the thickness reduction at location #4.

3. Weaker oxidization behavior with the corresponding oxide film thickness of 5 μm was observed during forming at 800 ℃, as compared to that of 25 μm at 900 ℃.

4. Recrystallization is the main microstructural mechanism that occurred for the entire forming process.

CHAPTER 9   CONCLUSIONS

A novel sheet forming process has been designed by combining hot drawing and gas forming in a single operation to establish a fast forming technology. The hybrid process together with a non-isothermal heating system is defined as superplastic-like forming, which can significantly increase forming rate, improve thickness uniformity and reduce forming temperature for sheet forming. Target materials for this technology are lightweight alloys that are widely used in aerospace and automotive industries. In this study, the process design proved the capability to form non-superplastic grade (commercial) AA5083 and Ti-6Al-4V alloys. The following conclusions can be drawn from the research.

I.   Material Properties

1. The annealed grains of AA5083 are fairly equiaxed, measuring 12.9 μm in grain size. The microstructure of commercial Ti-6Al-4V alloy is not homogeneous, showing various grain shapes with a mean grain size of 3.4 μm.

2. The AA5083 has largest tensile elongations of 80% and 93% at 400 °C and 500 °C, respectively. The Ti-6Al-4V alloy exhibits elongation of 300% at 800 °C and a strain rate of 10^{-3} s^{-1}.

3. Dynamic recrystallization of AA5083 occurred during tensile testing at temperatures greater than 500 °C and strain rates higher than 10^{-1} s^{-1}.

4. Non-superplastic grade AA5083 tensile samples fractured due to internal cavitation at lower strain rates ($< 10^{-2}$ s^{-1}), but the failure mode changed to external necking at higher strain rates ($> 10^{-1}$ s^{-1}).

171

II.   Superplastic-Like Forming of AA5083

1. The material at the sheet flange area was mechanical pre-formed into the deformation area before pressuring. A longer stroke introduced a larger amount of material draw-in, and therefore produced a better formed part with less thickness variations.

2. The maximum bulge height increased with increasing temperature. A higher local temperature under non-isothermal condition ensured the sheet being successfully formed with a greater percentage completion.

3. The optimal forming temperature for AA5083 is 400ºC, at which it is completed within 8 min for the gas forming phase. The forming strain rate during gas forming was maintained at 2×10^{-3} s^{-1} for good material formability.

4. The non-isothermal process produced an almost fully formed part with 92% fractional height and 137% surface expansion. The minimum thicknesses were formed at the outward corners of the final part, showing a maximum percentage thinning of 40%.

5. The main deformation mechanisms during hot drawing are subgrain boundary migration and subgrain rotation. Arrays of elongated grains and formation of new HAGBs containing more textured Brass and S components increased the texture intensity.

6. The gas forming operation could weaken the texture components, mainly because of the relatively slow strain rate (2×10^{-3} s^{-1}) which promoted further subgrain boundary migration and grain growth.

7. The initial fairly equiaxed structure in the annealed AA5083 was replaced by brick-shaped structures and a small amount (4.5%) of recrystallized grains after superplastic-like forming.

8. The yield strength of formed AA5083 part decreased from 193 to 134 MPa due to microstructural evolution, whereas the UTS was not influenced showing identical values before and after superplastic-like forming.

III.   FEM of Superplastic-Like Forming for AA5083

1. The main deformation mechanism, i.e. dislocation creep (subgrain boundary motion) with hardening and recovery contributions, was incorporated to construct the material model for AA5083 from room temperature to 550ºC and strain rates from 10^{-4} to 10^{-1} s^{-1}.

2. The dislocation density model was validated under tensile conditions and used in FEM to account for the plastic behavior of AA5083 during superplastic-like forming.

3. Comparisons of simulations and experimental results indicated large plastic strain areas with corresponding thickness variations obtained in the formed part.

4. Simulations highlighted that when the sheet was initially in contact with the punch, the material was stretched by the moving punch, resulting in some thickness reduction.

5. The stress concentration in the forming sheet, which is due to geometric inhomogeneity between the inward and outward radii, led to strain rate gradients during gas forming. The strain rate gradients gradually developed into thickness variations and localized thinning near the part outward corners.

IV.   Superplastic-Like Forming of Ti-6Al-4V alloy

1. The optimal forming temperature and forming rate of Ti-6Al-4V sheets suitable

for superplastic-like forming were determined to be 800ºC and 10^{-3} s^{-1} after laboratory testing. The lower forming temperature and faster forming rate could lead to less oxidation on the sheet surface.

2. The minimum thickness for the formed Ti-6Al-4V part was found at the areas adjacent to the die entry radii (sheet outward corners), and the maximum percentage thinning was 54%.

3. In addition to the influence of geometric inhomogeneity, microstructural defects, i.e. cracks and oxidation on the part surfaces, were the other source that could account for the thickness reduction.

4. Recrystallization during forming is the dominant microstructural mechanism which mainly contributed to the improved formability of Ti-6Al-4V alloy. The as-received structures were mostly transformed into equiaxed grains with an almost random misorientation distribution after superplastic-like forming.

CHAPTER 10 SUGGESTIONS FOR FUTURE WORK

The recommended work will be mainly on the improvements for the forming process for various applications and development on finite element modeling. Details are listed as follows:

1. **Establishing a full data system that works under a variety of forming conditions**

The drawing limit zones based on the current die assembly has been experimentally determined by hot drawing AA5083 at various temperatures. A more rounded system that can represent drawing limit with additional conditions, such as material selection, initial sheet dimension, die and punch shapes, and drawing speed, is required to determine the material forming potential for all conditions.

2. **Finite element modeling of non-isothermal forming and prediction of damage behavior**

As temperature plays an important role during superplastic-like forming, FEM should include temperature dependent data to simulate the forming process, especially for the gas forming step, under non-isothermal forming conditions. Additionally, FEM at temperatures at or above the recrystallization temperature requires special care due to the thermal softening behavior of the material which is not easily handled by commercial FEM codes. This will be one of the important challenges as far as simulation is concerned.

Simulations are to be used to determine the forming limit conditions. Such studies will help to guide the development of various material modes, which can be used to calculate the accurate thickness distributions, simulate the material damage behavior and assist with the real-time prediction for forming process.

3. Improvements of non-isothermal heating system

The oxidization behavior of Ti-6Al-4V alloy during superplastic-like forming revealed that a decrease of forming temperature from 900ºC to 800ºC significantly reduced the formation rate of oxide film on the sheet surfaces. However, the difference between the global (800ºC) and local (820ºC) temperatures in current system can still be increased to benefit the process. One of the improvements is to maintain the global temperature at the lowest possible level, preferably below the oxidation temperature (650ºC). A faster heating speed will benefit to enlarge the temperature difference due to less time for heat transfer from the die radii (a higher local temperature) to the entire die assembly (a lower global temperature). The selective heating areas need to be determined according to the part geometry so as to attain good thickness uniformity.

4. Optimization of process design

Expanding the capability of forming more complex-shaped workpieces is highly demanded for commercial applications. Geometric inhomogeneity is one of the most important factors leading to localized thinning during superplastic-like forming. Therefore, FEM is needed to design the configurations of the punch and die, especially for the punch geometry and die entry radius.

Friction between the sheet and die locks the material for further flowing during the gas

forming stage. Thus, in order to further improve the process, an optimized lubrication system will need to be developed in parallel with the process itself.

5. Extending forming capability to more materials

The materials (AA5083 and Ti-6Al-4V) used in this study are strain hardenable alloys. Since the forming process requires high temperature conditions ($0.3T_m$ to $0.6T_m$), an important phenomenon to pay attention to will be the material stability. The thermal instability of grain structures, such as grain growth, precipitation, oxidation, cavitation and cracking, are important issues in forming the material when the high temperature is reached. Moreover, problems linked to the inconsistency of the other materials, such as AA6061 which is a precipitation hardenable alloy due to the influence of heat treatment during hot forming. Therefore, study on the relationships between the material properties and process design together with FEM will advance this technology for greater academic and commercial applications.

PUBLICATIONS

1. **J. Liu**, M.J. Tan, Y. Aue-u-lan, M.L. Guo, S. Castagne, B.W. Chua, *Superplastic-like forming of Ti-6Al-4V alloy*, The International Journal of Advanced Manufacturing Technology, in press.

2. **J. Liu**, M.J. Tan, S.C.V. Lim, B.W. Chua, *Process optimization and microstructural development during Superplastic-like forming of AA5083*, The International Journal of Advanced Manufacturing Technology, under review.

3. **J. Liu**, J. Edberg, M.J. Tan, L.E. Lindgren, S. Castagne, A.E.W. Jarfors, *Finite element modelling of superplastic-like forming using a dislocation density based model for AA5083*, Modelling and Simulation in Materials Science and Engineering, 21 (2013) 025006.

4. **J. Liu**, M.J. Tan, Y. Aue-u-lan, A.E.W. Jarfors, K.S. Fong, S. Castagne, *Superplastic-like forming of non-superplastic AA5083 combined with mechanical pre-forming*, The International Journal of Advanced Manufacturing Technology, 52 (2011) 123.

5. **J. Liu**, M.J. Tan, A.E.W. Jarfors, Y. Aue-u-lan, S. Castagne, *Formability in AA5083 and AA6061 alloys for light weight applications,* Materials & Design, 31 (2010) S66.

6. **J. Liu**, M.J. Tan, S. Castagne, S.C.V. Lim, *An Optimized Sheet Metal Forming Process Using Non-Isothermal Heating System*, Advanced Materials Research, 500 (2012) 385.

7. **J. Liu**, M.J. Tan, A.E.W. Jarfors, S.C.V. Lim, K.S. Fong, S. Castagne, *Greener manufacturing: Superplastic-like forming*, Journal of Physics: Conference

Series, 379 (2012) 012034.

8. **J. Liu**, M.J. Tan, S. Castagne, S.C.V. Lim, *EBSD study of microstructural development during superplastic-like forming*, Materials Science Forum, 735 (2012) 37.

9. **J. Liu**, M.J. Tan, S. Castagne, S.C.V. Lim, *Sheet metal forming of light weight materials for aerospace applications*, Proceedings of Singapore Aerospace Technology & Engineering Conference, Singapore (2012).

10. **J. Liu**, M.J. Tan, S. Castagne, Y. Aue-u-lan, A.E.W. Jarfors, K.-S. Fong, E. Bayraktar, *Finite Element Modeling of a Non-Isothermal Superplastic-Like Forming Process*, AIP Conference Proceedings, 1315 (2011) 377.

11. **J. Liu**, M.J. Tan, S. Castagne, Y. Aue-u-lan, K.S. Fong, A.E.W. Jarfors, *Investigation of Process Parameters in Superplastic Forming of Mechanical Pre-Formed Sheet by FEM*, Key Engineering Materials, 447-448 (2010) 437.

12. **J. Liu**, M.J. Tan, S. Castagne, Y. Aue-u-lan, A.E.W. Jarfors, K.S. Fong, *Use of Mechanical Preforming for Superplastic Forming of Non-Superplastic Alloys*, Proceedings of the International Conference on Advances in Materials and Processing Technologies, Kuala Lumpur (2009).

REFERENCES

[1]   A. Tavassoli, S. Razavi, N. Fallah, *Superplastic forming of a commercial aluminum alloy*, Metall Mater Trans A, **6** (1975) 591.

[2]   D. Viswanathan, S. Venkatasamy, K.A. Padmanabhan, *Macro - , micro - and re-entrant shape forming of sheets of alloy Ti-6Al-4V*, J Mater Process Tech, **24** (1990) 213.

[3]   N. Chandra, D. Kannan, *Superplastic sheet metal forming of a generalized cup part i: uniform thinning*, J Mater Eng Perform, **1** (1992) 801.

[4]   N. Chandra, D. Kannan, *Superplastic sheet metal forming of a generalized cup part ii: nonuniform thinning*, J Mater Eng Perform, **1** (1992) 813.

[5]   K. Osada, *Commercial applications of superplastic forming*, J Mater Process Tech, **68** (1997) 241.

[6]   S.N. Patankar, M.J. Tan, *"Superplastic Forming" of Commercial Purity Aluminum*, Scripta Mater, **38** (1997) 145.

[7]   S.N. Patankar, C.T. Lim, M.J. Tan, *Superplastic Forming of Duplex Stainless Steel*, Metall Mater Trans A, **31A** (2000) 2394.

[8]   Y.W. Xun, M.J. Tan, *Applications of Superplastic Forming and Diffusion Bonding to Hollow Engine Blades*, J Mater Process Tech, **99** (2000) 80.

[9]   P.A. Friedman, S.G. Luckey, W.B. Copple, R. Allor, C.E. Miller, C. Young, *Overview of Superplastic Forming Research at Ford Motor Company*, J Mater Eng Perform, **13** (2004) 670.

[10] A.J. Barnes, *Superplastic Forming 40 Years and Still Growing*, J Mater Eng Perform, **16** (2007) 440.

[11] R. Verma, P.A. Friedman, A.K. Ghosh, S. Kim, C. Kim, *Characterization of Superplastic Deformation Behavior of a Fine Grain 5083 Al Alloy Sheet*, Metall Mater Trans A, **27A** (1996) 1889.

[12] C.S. Lee, S.B. Lee, J.S. Kim, Y.W. Chang, *Mechanical and microstructural analysis on the superplastic deformation behavior of Ti-6Al-4V Alloy*, Int J Mech Sci, **42** (2000) 1555.

[13] J. Pilling, N. Ridley, *Effect of hydrostatic pressure on cavitation in superplastic aluminium alloys*, Acta Metall, **34** (1986) 669.

[14] R. Verma, P. Friedman, A. Ghosh, C. Kim, S. Kim, *Superplastic forming characteristics of fine-grained 5083 aluminum*, J Mater Eng Perform, **4** (1995) 543.

[15] J.-K. Chang, E. Taleff, P. Krajewski, *Effect of Microstructure on Cavitation during Hot Deformation of a Fine-Grained Aluminum-Magnesium Alloy as Revealed through Three-Dimensional Characterization*, Metall Mater Trans A, **40** (2009) 3128.

[16] T. Morita, Y. Sakurai, Y. Tanaka, T. Hasegawa, *Relation between local necking and cavitation during high-temperature tensile deformation of polycrystalline pure aluminum*, Mater Sci Eng A, **526** (2009) 118.

[17] P.h. Sun, H.y. Wu, W.s. Lee, S.h. Shis, J.y. Perng, S. Lee, *Cavitation behavior in superplastic 5083 Al alloy during multiaxial gas blow forming with lubrication*, Int J Mach Tool Manu, **49** (2009) 13.

[18] J. Schroth, H. Brueggeman, N. Grewal, *Quick Plastically Formed Aluminum Doors: Design and Performance*, J Mater Eng Perform, **16** (2007) 339.

[19] J.W. Edington, K.N. Melton, C.P. Cutler, *Superplasticity*, Prog Mater Sci, **21** (1976) 61.

[20] E. Kovács-Csetenyi, T. Torma, T. Turmezey, N.Q. Chinh, A. Juhász, I. Kovács, *Superplasticity of AlMgSi alloys*, J Mater Sci, **27** (1992) 6141.

[21] G.A. Edwards, K. Stiller, G.L. Dunlop, M.J. Couper, *The precipitation sequence in Al-Mg-Si alloys*, Acta Mater, **46** (1998) 3893.

[22] S.H. Lee, Y. Saito, T. Sakai, H. Utsunomiya, *Microstructures and mechanical properties of 6061 aluminum alloy processed by accumulative roll-bonding*, Mater Sci Eng A, **325** (2002) 228.

[23] W.J. Kim, Y.K. Sa, H.K. Kim, U.S. Yoon, *Plastic forming of the equal-channel angular pressing processed 6061 aluminum alloy*, Mater Sci Eng A, **487** (2008) 360.

[24] M. Furukawa, Y. Iwahashi, Z. Horita, M. Nemoto, N.K. Tsenev, R.Z. Valiev, T.G. Langdon, *Structural evolution and the Hall-Petch relationship in an Al-Mg-Li-Zr alloy with ultra-fine grain size*, Acta Mater, **45** (1997) 4751.

[25] T.B. Sercombe, G.B. Schaffer, *Rapid Manufacturing of Aluminum Components*, Science, **301** (2003) 1225.

[26] Z.Y. Ma, R.S. Mishra, M.W. Mahoney, *Superplastic deformation behaviour of friction stir processed 7075Al alloy*, Acta Mater, **50** (2002) 4419.

[27] A. Dutta, I. Charit, L.B. Johannes, R.S. Mishra, *Deep cup forming by superplastic punch stretching of friction stir processed 7075 Al alloy*, Mater Sci Eng A, **395** (2005) 173.

[28] K. Chen, H. Liu, Z. Zhang, S. Li, R.I. Todd, *The improvement of constituent dissolution and mechanical properties of 7055 aluminum alloy by stepped heat treatments*, J Mater Process Tech, **142** (2003) 190.

[29] S. Griffiths, D. Whittle, N. Ridley, R.I. Todd, *Superplasticity in Commercial Al 7475*, Mater Sci Forum, **447-448** (2004) 283.

[30] R. Verma, A.K. Ghosh, S. Kim, C. Kim, *Grain refinement and superplasticity in 5083 Al*, Mater Sci Eng A, **191** (1995) 143.

[31] *Aluminum 5083*, ASM International, Materials Park, Ohio, 1978.

[32] X.J. Zhu, *High Temperature Deformation and Superplasticity of Titanium Alloys*, Nanyang Technological University, Singapore, 2006.

[33] A.V. Sergueeva, V.V. Stolyarov, R.Z. Valiev, A.K. Mukherjee, *Enhanced superplasticity in a Ti-6Al-4V alloy processed by severe plastic deformation*, Scripta Mater, **43** (2000) 819.

[34] R. Singh, P.D. Lee, R.J. Dashwood, T.C. Lindley, *Titanium foams for biomedical applications: a review*, Mater Technol: Adv Perform Mater, **25** (2010) 127.

[35] R.Y. Lutfullin, A.A. Kruglov, R.V. Safiullin, M.K. Mukhametrakhimov, O.A. Rudenko, *Processing properties of nano- and submicro-crystalline Ti-6Al-4V titanium alloy*, Mater Sci Eng A, **503** (2009) 52.

[36] B. Huang, Z. Deng, Y. Liu, X. Qu, Y. He, *Superplastic behavior of a TiAl-based alloy*, Intermetallics, **8** (2000) 559.

[37] G.A. Salishchev, R.M. Galeyev, O.R. Valiakhmetov, R.V. Safiullin, R.Y. Lutfullin, O.N. Senkov, F.H. Froes, O.A. Kaibyshev, *Development of Ti-6Al-4V sheet with low temperature superplastic properties*, J Mater Process Tech, **116** (2001) 265.

[38] A.V. Sergueeva, V.V. Stolyarov, R.Z. Valiev, A.K. Mukherjee, *Superplastic behaviour of ultrafine-grained Ti-6Al-4V alloys*, Mater Sci Eng A, **323** (2002) 318.

[39] S.V. Zherebtsov, G.A. Salishchev, R.M. Galeyev, O.R. Valiakhmetov, S.Y. Mironov, S.L. Semiatin, *Production of submicrocrystalline structure in large-scale Ti-6Al-4V billet by warm severe deformation processing*, Scripta Mater, **51** (2004) 1147.

[40] G. Wang, M.W. Fu, *Maximum m superplasticity deformation for Ti-6Al-4V titanium alloy*, J Mater Process Tech, **192-193** (2007) 555.

[41] J. Pilling, N. Ridley, *Superplasticity in Crystalline Solids*, The Institute of Metals, London, 1989.

[42] T.G. Nieh, J. Wadsworth, O.D. Sherby, *Superplasticity in Metals and Ceramics*, Cambridge University Press, Cambridge, 1997.

[43] M.H. Hojjati, M. Zoorabadi, S.J. Hosseinipour, *Optimization of superplastic hydroforming process of Aluminium alloy 5083*, J Mater Process Tech, **205** (2008) 482.

[44] M.A. Nazzal, M.K. Khraisheh, F.K. Abu-Farha, *The effect of strain rate sensitivity evolution on deformation stability during superplastic forming*, J Mater Process Tech, **191** (2007) 189.

[45] Z.P. Chen, P.F. Thomson, *A study of post-form static and fatigue properties of superplastic 7475-SPF and 5083-SPF aluminium alloys*, J Mater Process Tech, **148** (2004) 204.

[46] M.A. Khaleel, K.I. Johnson, C.H. Hamilton, M.T. Smith, *Deformation Modeling of Superplastic AA-5083*, Int J Plasticity, **14** (1998) 1133.

[47] E.M. Taleff, *An Overview of Hot- and Warm-Forming of Al-Mg Alloys*, Key Eng Mater, **433** (2010) 259.

[48] T.R. McNelley, K. Oh-Ishi, A.P. Zhilyaev, S. Swaminathan, P.E. Krajewski, E.M. Taleff, *Characteristics of the Transition from Grain-Boundary Sliding to Solute Drag Creep in Superplastic AA5083*, Metall Mater Trans A, **39** (2008) 50.

[49] P.A. Friedman, W.B. Copple, *Superplastic Response in Al-Mg Sheet Alloys*, J Mater Eng Perform, **13** (2004) 335.

[50] M.A. Kulas, W.P. Green, E.M. Taleff, P.E. Krajewski, T.R. Mcnelley, *Deformation Mechanisms in Superplastic AA5083 Materials*, Metall Mater Trans A, **36A** (2005) 1249.

[51] M.F. Ashby, R.A. Verrall, *Diffusion-accommodated flow and superplasticity*, Acta Metall, **21** (1973) 149.

[52] H.J. Frost, M.F. Ashby, *Deformation-Mechanism Maps*, Pergaman Press, Oxford, 1982.

[53] K. Kannan, J.S. Vetrano, C.H. Hamilton, *Effects of Alloy Modification and Thermomechanical Processing on Recrystallization of Al-Mg-Mn Alloys*, Metall Mater Trans A, **27A** (1996) 2947.

[54] Y. Wu, L.D. Castillo, E.J. Lavernia, *Superplastic Behavior of Spray-Deposited 5083 Al*, Metall Mater Trans A, **28A** (1997) 1059.

[55] D.H. Bae, A.K. Ghosh, *Grain Size and Temperature Dependence of Superplastic Deformation in an Al-Mg Alloy Under Isostructural Condition*, Acta Mater, **48** (2000) 1207.

[56] R.M. Cleveland, A.K. Ghosh, J.R. Bradley, *Comparison of Superplastic Behavior in Two 5083 Aluminum Alloys*, Mater Sci Eng A, **351** (2003) 228.

[57] W.J. Kim, Y.K. Sa, H.K. Kim, U.S. Yoon, *Plastic Forming of the Equal-Channel Angular Pressing Procesed 6061 Aluminum Alloy*, Mater Sci Eng A, **487** (2008) 360.

[58] K.T. Park, D.Y. Hwang, S.Y. Chang, D.H. Shin, *Low-Temperature Superplastic Behavior of a Submicrometer-Grained 5083 Al Alloy Fabricated by Severe Plastic Deformation*, Metall Mater Trans A, **33A** (2002) 2859.

[59] J.S. Vetrano, C.A. Lavender, C.H. Hamilton, M.T. Smith, S.M. Bruemmer, *Superplastic behavior in a commercial 5083 Aluminum Alloy*, Scripta Mater, **30** (1994) 565.

[60] N. Llorca-Isern, C. Luis-Perez, P.A. Gonzalez, L. Laborde, D. Patino, *Analysis of Structure and Mechanical Properties of AA5083 Aluminium Alloys Processed by ECAE*, Rev Adv Mater Sci, **10** (2005) 473.

[61] H.H. Chen, J.Y. Wang, J. Lee, S. Lee, *Superplasticity of AA5083 alloy as processed by equal channel angular extrusion*, J Alloy Compd, **460** (2008) 305.

[62] Z. Horita, M. Furukawa, M. Nemoto, A.J. Barnes, T.G. Langdon, *Superplastic forming at high strain rates after severe plastic deformation*, Acta Mater, **48** (2000) 3633.

[63] L.B. Johannes, I. Charit, R.S. Mishra, R. Verma, *Enhanced superplasticity through friction stir processing in continuous cast AA5083 Aluminum*, Mater Sci Eng A, **464** (2007) 351.

[64] R.S. Mishra, M.W. Mahoney, *Friction stir processing: A new grain refinement technique to achieve high strain rate superplasticity in commercial alloys*, Mater Sci Forum, **357-359** (2001) 507.

[65] S. Katsas, R. Dashwood, M. Jackson, R. Grimes, *Influence of subsequent cold work on the superplastic properties of a friction stir welded (FSW) aluminium alloy*, Mater Sci Eng A, **527** (2010) 1022.

[66] R.Z. Valiev, A.V. Korznikov, R.R. Mulyukov, *Structure and properties of ultrafine-grained materials produced by severe plastic deformation*, Mater Sci Eng A, **168** (1993) 141.

[67] R.R. Mulyukov, A.I. Pshenichnyuk, *Structure and damping of nanocrystalline metals and alloys prepared by high plastic deformation techniques*, J Alloy Compd, **355** (2003) 26.

[68] E. Avtokratova, O. Sitdikov, M. Markushev, R. Mulyukov, *Extraordinary high-strain rate superplasticity of severely deformed Al–Mg–Sc–Zr alloy*, Mater Sci Eng A, **538** (2012) 386.

[69] X.J. Zhu, M.J. Tan, W. Zhou, *Enhanced superplasticity in commercially pure titanium alloy*, Scripta Mater, **52** (2005) 651.

[70] H. Yoshimura, J. Nakahigashi, *Ultra-fine-grain refinement and superplasticity of titanium alloys obtained through protium treatment*, Int J Hydrogen Energ, **27** (2002) 769.

[71] D. Lin, F. Sun, *Superplasticity in a large-grained TiAl alloy*, Intermetallics, **12** (2004) 875.

[72] B.P. Bewlay, M.F.X. Gigliotti, F.Z. Utyashev, O.A. Kaibyshev, *Superplastic roll forming of Ti alloys*, Mater Design, **21** (2000) 287.

[73] G. Wang, K.F. Zhang, D.Z. Wu, J.Z. Wang, Y.D. Yu, *Superplastic forming of bellows expansion joints made of titanium alloys*, J Mater Process Tech, **178** (2006) 24.

[74] E.N. Chumachenko, V.K. Portnoi, L. Paris, T. Billaudeau, *Analysis of the SPF of a titanium alloy at lower temperatures*, J Mater Process Tech, **170** (2005) 448.

[75] V.V. Stolyarov, Y.T. Zhu, I.V. Alexandrov, T.C. Lowe, R.Z. Valiev, *Grain refinement and properties of pure Ti processed by warm ECAP and cold rolling*, Mater Sci Eng A, **343** (2003) 43.

[76] V.A. Goltsov, *Hydrogen treatment (processing) of materials: current status and prospects*, J Alloy Compd, **293–295** (1999) 844.

[77] K. Lange, *Handbook of Metal Forming*, Society of Manufacturing Engineers, New York, 1985.

[78] G.E. Dieter, *Mechanical Metallurgy*, McGraw-Hill, New York, 1986.

[79] R. Hawkins, J.A. Belk, *Deep Drawing of Superplastic Material*, Met Technol, **3** (1976) 516.

[80] D.N. Lee, *Relation between limiting drawing ratio and plastic strain ratio*, J Mater Sci Lett, **3** (1984) 677.

[81] Y.M. Huang, C.L. Li, *Limiting drawing ratio of the cup-drawing process with stabilization matrices approach*, J Mater Process Tech, **83** (1998) 26.

[82] D.K. Leu, J.Y. Wu, *A Simplified Approach to Estimate Limiting Drawing Ratio and Maximum Drawing Load in Cup Drawing*, J Eng Mater Tech, **126** (2004) 116.

[83] L.F. Menezes, C. Teodosiu, *Three-dimensional numerical simulation of the deep-drawing process using solid finite elements*, J Mater Process Tech, **97** (2000) 100.

[84] S.B. Park, Y. Choi, B.M. Kim, J.C. Choi, *A CAD/CAM system for deep drawing dies in a simple-action press*, J Mater Process Tech, **87** (1999) 258.

[85] S.H. Zhang, J. Danckert, *Development of hydro-mechanical deep drawing*, J Mater Process Tech, **83** (1998) 14.

[86] J. Lin, S.D. Zhao, Z.Y. Zhang, Z.W. Wang, *Deep drawing using a novel hydromechanical tooling*, Int J Mach Tool Manu, **49** (2009) 73.

[87] M.A. Hassan, R. Suenaga, N. Takakura, K. Yamaguchi, *A novel process on friction aided deep drawing using tapered blank holder divided into four segments*, J Mater Process Tech, **159** (2005) 418.

[88] S. Yoshihara, H. Nishimura, H. Yamamoto, K.I. Manabe, *Formability enhancement in magnesium alloy stamping using a local heating and cooling technique: circular cup deep drawing process*, J Mater Process Tech, **142** (2003) 609.

[89] G.C. Cornfield, R.H. Johnson, *The forming of superplastic sheet metal*, Int J Mech Sci, **12** (1970) 479.

[90] E. Taleff, D. Lesuer, J. Wadsworth, *Enhanced ductility in coarse-grained Al-Mg alloys*, Metall Mater Trans A, **27** (1996) 343.

[91] E. Taleff, G. Henshall, T. Nieh, D. Lesuer, J. Wadsworth, *Warm-temperature tensile ductility in Al−Mg alloys*, Metall Mater Trans A, **29** (1998) 1081.

[92] E. Taleff, P. Nevland, P. Krajewski, *Tensile ductility of several commercial aluminum alloys at elevated temperatures*, Metall Mater Trans A, **32** (2001) 1119.

[93] K.S.K. Chockalingam, M. Neelakantan, S. Devaraj, K.A. Padmanabhan, *On the pressure forming of two superplastic alloys*, J Mater Sci, **20** (1985) 1310.

[94] R.J. Talling, R.J. Dashwood, M. Jackson, D. Dye, *On the mechanism of superelasticity in Gum metal*, Acta Mater, **57** (2009) 1188.

[95] R. Dashwood, D. Klaumunzer, M. Jackson, Z.Y. Fan, R. Grimes, *The Development of Superplastic Magnesium Alloy Sheet*, Key Eng Mater, **433** (2010) 273.

[96] W.J. Kim, S.W. Chung, C.S. Chung, D. Kum, *Superplasticity in thin magnesium alloy sheets and deformation mechanism maps for magnesium alloys at elevated temperatures*, Acta Mater, **49** (2001) 3337.

[97] S.W. Chung, K. Higashi, W.J. Kim, *Superplastic gas pressure forming of fine-grained AZ61 magnesium alloy sheet*, Mater Sci Eng A, **372** (2004) 15.

[98] W.J. Kim, J.D. Park, U.S. Yoon, *Superplasticity and Superplastic Forming of Mg-Al-Zn Alloy Sheets Fabricated by Strip Casting Method*, J Alloy Compd, **464** (2008) 197.

[99] R.B. Figueiredo, T.G. Langdon, *Principles of grain refinement and superplastic flow in magnesium alloys processed by ECAP*, Mater Sci Eng A, **501** (2009) 105.

[100] J. Wittenauer, T.G. Nieh, J. Wadsworth, *A first report on superplastic gas-pressure forming of ceramic sheet*, Scripta Mater, **26** (1992) 551.

[101] T.G. Nieh, C.M. McNally, J. Wadsworth, *Superplastic properties of a fine-grained yttria-stabilized tetragonal polycrystal of zirconia*, Scripta Metall, **22** (1988) 1297.

[102] T.G. Nieh, C.M. McNally, J. Wadsworth, *Superplastic behavior of a 20% Al2O3/YTZ ceramic composite*, Scripta Metall, **23** (1989) 457.

[103] T.G. Nieh, J. Wadsworth, *Superelastic behaviour of a fine-grained, yttria-stabilized, tetragonal zirconia polycrystal (Y-TZP)*, Acta Metall Mater, **38** (1990) 1121.

[104] T.G. Nieh, J. Wadsworth, *Superplasticity in fine-grained 20% Al2O3/YTZ composite*, Acta Metall Mater, **39** (1991) 3037.

[105] G. Giuliano, *Constitutive equation for superplastic Ti-6Al-4V alloy*, Mater Design, **29** (2008) 1330.

[106] Y. Luo, C. Miller, G. Luckey, P. Friedman, Y. Peng, *On Practical Forming Limits in Superplastic Forming of Aluminum Sheet*, J Mater Eng Perform, **16** (2007) 274.

[107] S. Thiruvarudchelvan, M.J. Tan, *Two Novel Techniques for Forming Regularly Spaced Deep Recesses on Aluminium Sheet Panels*, Mater Sci Forum, **437-438** (2003) 253.

[108] L. Hefti, *Commercial Airplane Applications of Superplastically Formed AA5083 Aluminum Sheet*, J Mater Eng Perform, **16** (2007) 136.

[109] W. Han, K. Zhang, G. Wang, *Superplastic forming and diffusion bonding for honeycomb structure of Ti-6Al-4V alloy*, J Mater Process Tech, **183** (2007) 450.

[110] D.G. Sanders, M. Ramulu, P.D. Edwards, *Superplastic forming of friction stir welds in Titanium alloy 6Al-4V: preliminary results*, Materialwiss Werkst, **39** (2008) 353.

[111] http://www.cyrilbath.com

[112] http://www.superform-aluminium.com

[113] P. Comley, *Multi-rate Superplastic Forming of Fine Grain Ti-6Al-4V Titanium Alloy*, J Mater Eng Perform, **16** (2007) 150.

[114] L.P. Troeger, E.A. Starke, *Microstructural and mechanical characterization of a superplastic 6xxx aluminum alloy*, Mater Sci Eng A, **277** (2000) 102.

[115] A.J. Barnes, *Industrial Applications of Superplastic Forming: Trends and Prospects*, Mater Sci Forum, **357-359** (2001) 3.

[116] R.L. Hecht, A.M. Sherman, S.A. Arnold, *The Economic Feasibility of Using Superplastic Forming of Aluminum for Automotive Applications*, Ford Technical Report, 1994.

[117] H.L. Du, P.K. Datta, D.B. Lewis, J.S. Burnell-Gray, *Air oxidation behaviour of Ti-6Al-4V alloy between 650 and 850 °C*, Corros Sci, **36** (1994) 631.

[118] S.N. Patankar, Y.T. Kwang, M.J. Tan, *Alpha casing and superplastic behavior of Ti–6Al–4V*, J Mater Process Tech, **112** (2001) 24.

[119] S. Rhaipu, M.L.H. Wise, P.S. Bate, *Microstructural gradients in the superplastic forming of Ti-6Al-4V*, Metall Mater Trans A, **33** (2002) 93.

[120] US Patent 3340101, *Thermoforming of metals*, 1967.

[121] M. Mahoney, A.J. Barnes, W.H. Bingel, C. Fuller, *Superplastic forming of 7475 Al sheet after friction stir processing (FSP)*, Mater Sci Forum, **447-448** (2004) 505.

[122] P. Krajewski, A. Morales, *Tribological issues during quick plastic forming*, J Mater Eng Perform, **13** (2004) 700.

[123] S.G. Luckey, S. Subramanian, C. Young, P.A. Friedman, *Technical and Cost Study of Superplastic Forming of a Lightweight Aluminum Door Structure*, J Mater Eng Perform, **16** (2007) 266.

[124] P.K.D.V. Yarlagadda, P. Gudimetla, C. Adam, *Finite element analysis of high strain rate superplastic forming (SPF) of Al-Ti alloys*, J Mater Process Tech, **130-131** (2002) 469.

[125] M.H. Chen, Y.H. Xue, Y.L. Rui, J.H. Zhou, M. Wang, *Numerical simulation and experimental investigation of high strain rate Superplastic Forming (SPF) of Al-6Mg-0.2Sc alloy*, Mater Sci Forum, **551-552** (2007) 287.

[126] US Patent 6253588, *Quick plastic forming of aluminum alloy sheet metal*, 2001.

[127] US Patent 6799449, *Apparatus for superplastic forming*, 2004.

[128] US Patent 6880377, *Method for double action gas pressure forming sheet material*, 2005.

[129] US Patent 6886383, *Method for stretch forming sheet metal by pressing and the application of gas pressure*, 2005.

[130] US Patent 7028519, *High throughput quick-plastic-forming*, 2006.

[131] US Patent 7284402, *System and process for superplastic forming*, 2007.

[132] US Patent 7431196, *Method and apparatus for forming complex contour structural assemblies*, 2008.

[133] US Patent 7389655, *Sheet metal forming process*, 2008.

[134] US Patent 7827840, *Multistage superplastic forming apparatus and method*, 2010.

[135] US Patent 7832245, *Method and apparatus for hot forming of sheet metal in titanium-base alloys*, 2010.

[136] US Patent 7655535, *Preform for forming complex contour structural assemblies*, 2011.

[137] C.H. Hamilton, A.K. Ghosh, *"Superplastic Sheet Forming" in Metals Handbook*, ASM International, Materials Park, Ohio, 1988.

[138] Y. Luo, S.G. Luckey, P.A. Friedman, Y. Peng, *Development of an advanced superplastic forming process utilizing a mechanical pre-forming operation*, Int J Mach Tool Manu, **48** (2008) 1509.

[139] P.J. Hurley, F.J. Humphreys, *The application of EBSD to the study of substructural development in a cold rolled single-phase aluminium alloy*, Acta Mater, **51** (2003) 1087.

[140] S. Agarwal, P.E. Krajewski, C.L. Briant, *Dynamic Recrystallization of AA5083 at 450 °C: the Effects of Strain Rate and Particle Size*, Metall Mater Trans A, **39** (2008) 1277.

[141] H. Jazaeri, F.J. Humphreys, *The transition from discontinuous to continuous recrystallization in some aluminium alloys: I – the deformed state*, Acta Mater, **52** (2004) 3239.

[142] H. Jazaeri, F.J. Humphreys, *The transition from discontinuous to continuous recrystallization in some aluminium alloys: II – annealing behaviour*, Acta Mater, **52** (2004) 3251.

[143] M.T. Pérez-Prado, G. González-Doncel, O.A. Ruano, T.R. McNelley, *Texture analysis of the transition from slip to grain boundary sliding in a discontinuously recrystallized superplastic aluminum alloy*, Acta Mater, **49** (2001) 2259.

[144] R.S. Mishra, T.R. Bieler, A.K. Mukherjee, *Superplasticity in powder metallurgy aluminum alloys and composites*, Acta Metall Mater, **43** (1995) 877.

[145] F.J. Humphreys, *Review Grain and subgrain characterisation by electron backscatter diffraction*, J Mater Sci, **36** (2001) 3833.

[146] F.C. Liu, P. Xue, Z.Y. Ma, *Microstructural evolution in recrystallized and unrecrystallized Al–Mg–Sc alloys during superplastic deformation*, Mater Sci Eng A, **547** (2012) 55.

[147] K. Oh-ishi, J. Boydon, T. McNelley, *Processing, deformation, and failure in superplastic aluminum alloys: Applications of orientation-imaging microscopy*, J Mater Eng Perform, **13** (2004) 710.

[148] F.J. Humphreys, *Characterisation of fine-scale microstructures by electron backscatter diffraction (EBSD)*, Scripta Mater, **51** (2004) 771.

[149] J. Hu, T. Ishikawa, K. Ikeda, *Analysis on earing behavior of textured pure aluminum and A5083 alloy sheets*, J Mater Process Tech, **83** (1998) 200.

[150] F.J. Humphreys, M. Hatherly, *Recrystallization and Related Annealing Phenomena*, Elsevier, Oxford, 2004.

[151] V. Randle, O. Engler, *Introduction to texture analysis: macrotexture, microtexture and orientation mapping*, CRC Press, Boca Raton, 2000.

[152] J. Hirsch, K. Lücke, *Overview no. 76: Mechanism of deformation and development of rolling textures in polycrystalline f.c.c. metals—I. Description of rolling texture development in homogeneous CuZn alloys*, Acta Metall, **36** (1988) 2863.

[153] N. Chandra, *Constitutive behavior of superplastic materials*, Int J Nonlinear Mech, **37** (2002) 461.

[154] P. Friedman, A. Ghosh, *Control of superplastic deformation rate during uniaxial tensile tests*, Metall Mater Trans A, **27** (1996) 3030.

[155] H. Raman, G. Luckey, G. Kridli, P. Friedman, *Development of Accurate Constitutive Models for Simulation of Superplastic Forming*, J Mater Eng Perform, **16** (2007) 284.

[156] L. Carrino, G. Giuliano, C. Palmieri, *On the optimisation of superplastic forming processes by the finite-element method*, J Mater Process Tech, **143-144** (2003) 373.

[157] L. Carrino, G. Giuliano, G. Napolitano, *A posteriori optimisation of the forming pressure in superplastic forming processes by the finite element method*, Finite Elem Anal Des, **39** (2003) 1083.

[158] M.A. Khaleel, H.M. Zbib, E.A. Nyberg, *Constitutive modeling of deformation and damage in superplastic materials*, Int J Plasticity, **17** (2001) 277.

[159] M. Nazzal, M. Khraisheh, B. Darras, *Finite element modeling and optimization of superplastic forming using variable strain rate approach*, J Mater Eng Perform, **13** (2004) 691.

[160] A. Alankar, I.N. Mastorakos, D.P. Field, *A dislocation-density-based 3D crystal plasticity model for pure aluminum*, Acta Mater, **57** (2009) 5936.

[161] R.J. Asaro, J.R. Rice, *Strain localization in ductile single crystals*, J Mech Phys Solids, **25** (1977) 309.

[162] U.F. Kocks, H. Mecking, *Physics and phenomenology of strain hardening: the FCC case*, Prog Mater Sci, **48** (2003) 171.

[163] A. Ma, F. Roters, *A constitutive model for fcc single crystals based on dislocation densities and its application to uniaxial compression of aluminium single crystals*, Acta Mater, **52** (2004) 3603.

[164] Y.M. Hwang, H.S. Lay, *Study on superplastic blow-forming in a rectangular closed-die*, J Mater Process Tech, **140** (2003) 426.

[165] R.A. Vasin, F.U. Enikeev, M. Tokuda, R.V. Safiullin, *Mathematical modelling of the superplastic forming of a long rectangular sheet*, Int J Nonlinear Mech, **38** (2003) 799.

[166] X.D. Ding, H.M. Zbib, C.H. Hamilton, A.E. Bayoumi, *On the optimization of superplastic blow-forming processes*, J Mater Eng Perform, **4** (1995) 474.

[167] L. Adam, J.-P. Ponthot, *A coupled thermo-viscoplastic formulation at finite strains for the numerical simulation of superplastic forming*, J Mater Process Tech, **139** (2003) 514.

[168] G.Y. Li, M.J. Tan, K.M. Liew, *Three-dimensional modeling and simulation of superplastic forming*, J Mater Process Tech, **150** (2004) 76.

[169] Y. Bergström, *A dislocation model for the stress-strain behaviour of polycrystalline α-Fe with special emphasis on the variation of the densities of mobile and immobile dislocations*, Mater Sci Eng, **5** (1970) 193.

[170] Y. Estrin, K. Rhee, R. Lapovok, P.F. Thomson, *Mechanical Behavior of Alloy AA6111 Processed by Severe Plastic Deformation: Modeling and Experiment*, J Eng Mater Tech, **129** (2007) 380.

[171] S.C. Baik, Y. Estrin, H.S. Kim, R.J. Hellmig, *Dislocation density-based modeling of deformation behavior of aluminium under equal channel angular pressing*, Mater Sci Eng A, **351** (2003) 86.

[172] J. May, M. Dinkel, D. Amberger, H.W. Höppel, M. Göken, *Mechanical Properties, Dislocation Density and Grain Structure of Ultrafine-Grained Aluminum and Aluminum-Magnesium Alloys*, Metall Mater Trans A, **38** (2007) 1941.

[173] Y. Estrin, L.S. Tóth, A. Molinari, Y. Bréchet, *A dislocation-based model for all hardening stages in large strain deformation*, Acta Mater, **46** (1998) 5509.

[174] L.S. Tóth, A. Molinari, Y. Estrin, *Strain hardening at large strains as predicted by dislocation based polycrystal plasticity model*, J Eng Mater Tech, Trans ASME, **124** (2002) 71.

[175] G. Ananthakrishna, *Current theoretical approaches to collective behavior of dislocations*, Phys Rep, **440** (2007) 113.

[176] L.P. Kubin, Y. Estrin, *Evolution of dislocation densities and the critical conditions for the Portevin-Le Châtelier effect*, Acta Metall Mater, **38** (1990) 697.

[177] D.L. Holt, *Dislocation cell formation in metals*, J Appl Phys, **41** (1970) 3197.

[178] G. Meyrick, *On the dislocation density in aluminum during Harper-Dorn creep*, Scripta Metall, **23** (1989) 2025.

[179] D. Kuhlmann-Wilsdorf, N.R. Comins, *Dislocation cell formation and work hardening in the unidirectional glide of f.c.c. metals I: Basic theoretical analysis*

of cell walls parallel to the primary glide plane in early stage II, Mater Sci Eng, **60** (1983) 7.

[180] A. Arsenlis, D.M. Parks, *Modeling the evolution of crystallographic dislocation density in crystal plasticity*, J Mech Phys Solids, **50** (2002) 1979.

[181] F. Zhang, W.A. Curtin, *Atomistically informed solute drag in Al-Mg*, Modell Simul Mater Sci Eng, **16** (2008) 055006.

[182] F. Roters, D. Raabe, G. Gottstein, *Work hardening in heterogeneous alloys - a microstructural approach based on three internal state variables*, Acta Mater, **48** (2000) 4181.

[183] W. Blum, P. Eisenlohr, F. Breutinger, *Understanding creep—a review*, Metall Mater Trans A, **33** (2002) 291.

[184] C. Woodward, D.R. Trinkle, L.G. Hector, Jr., D.L. Olmsted, *Prediction of Dislocation Cores in Aluminum from Density Functional Theory*, Phys Rev Lett, **100** (2008) 045507.

[185] J.P. Poirier, *Creep of crystals : high-temperature deformation processes in metals, ceramics, and minerals*, Cambridge University Press, Cambridge, 1985.

[186] M. Militzer, W.P. Sun, J.J. Jonas, *Modelling the effect of deformation-induced vacancies on segregation and precipitation*, Acta Metall Mater, **42** (1994) 133.

[187] R.D. Wood, J. Bonet, *A review of the numerical analysis of superplastic forming*, J Mater Process Tech, **60** (1996) 45.

[188] G. Luckey Jr, P. Friedman, K. Weinmann, *Design and experimental validation of a two-stage superplastic forming die*, J Mater Process Tech, **209** (2009) 2152.

[189] L. Carrino, G. Giuliano, *Finite Element Modelling and the Experimental Verification of Superplastic Forming*, Adv Perform Mater, **6** (1999) 149.

[190] Y.H. Kim, S.S. Hong, J.S. Lee, R.H. Wagoner, *Analysis of superplastic forming processes using a finite-element method*, J Mater Process Tech, **62** (1996) 90.

[191] R. Hambli, A. Potiron, *Comparison between 2D and 3D numerical modeling of superplastic forming processes*, Comput Method Appl M, **190** (2001) 4871.

[192] J.H. Yoon, H.S. Lee, Y.M. Yi, *Finite element simulation on superplastic blow forming of diffusion bonded 4 sheets*, J Mater Process Tech, **201** (2008) 68.

[193] F.J. Humphreys, Y. Huang, I. Brough, C. Harris, *Electron backscatter diffraction of grain and subgrain structures — resolution considerations*, Journal of Microscopy, **195** (1999) 212.

[194] HKL, *Channel 5*, Oxford Instruments, Oxford, 2010.

[195] ASTM, *Standard Guide for Electrolytic Polishing of Metallographic Specimens*, ASTM International, West Conshohocken, PA, 2009.

[196] G. Wu, D. Juul Jensen, *Automatic determination of recrystallization parameters based on EBSD mapping*, Mater Charact, **59** (2008) 794.

[197] P.S. Bate, D.C. Price, D.J. Barrett, W.T. Roberts, *The simulation, control and optimisation of the gas-pressure forming of aluminium alloy sheet at elevated temperature*, J Mater Process Tech, **38** (1993) 589.

[198] Z. Chen, P.F. Thomson, *Friction against superplastic aluminium alloys*, Wear, **201** (1996) 227.

[199] *Marc User's Guide*, MSC. Software Corporation, Santa Ana, 2010.

[200] K.I. Johnson, M.A. Khaleel, M.T. Smith, *Process Simulation for Optimizing Superplastic Forming of Sheet Metal*, Technical support document for the proposed Federal Commercial Building energy code, (1995) 75.

[201] M.E. Kassner, *Recrystallization in "Fundamentals of Creep in Metals and Alloys (Second edition)"*, Elsevier, Amsterdam, 2008.

[202] J.K. Mackenzie, *Second Paper on Statistics Associated with the Random Disorientation of Cubes*, Biometrika, **45** (1958) 229.

[203] S.F. Exell, D.H. Warrington, *Sub-grain boundary migration in aluminium*, Philos Mag, **26** (1972) 1121.

[204] W. Blum, Q. Zhu, R. Merkel, H.J. McQueen, *Geometric dynamic recrystallization in hot torsion of Al-5Mg-0.6Mn (AA5083)*, Mater Sci Eng A, **205** (1996) 23.

[205] H.J. McQueen, M.E. Kassner, *Comments on 'a model of continuous dynamic recrystallization' proposed for aluminum*, Scripta Mater, **51** (2004) 461.

[206] M.H. Alvi, S.W. Cheong, J.P. Suni, H. Weiland, A.D. Rollett, *Cube texture in hot-rolled aluminum alloy 1050 (AA1050)—nucleation and growth behavior*, Acta Mater, **56** (2008) 3098.

[207] P. Bate, A. Oscarsson, *Deformation banding and texture in hot rolled Al-1.0Mn-1.2Mg alloy*, Mater Sci Tech, **6** (1990) 520.

[208] J. Edington, *Microstructural aspects of superplasticity*, Metall Mater Trans A, **13** (1982) 703.

[209] J. Hjelen, R. Ørsund, E. Nes, *On the origin of recrystallization textures in aluminium*, Acta Metall Mater, **39** (1991) 1377.

[210] E.O. Hall, *The Deformation and Ageing of Mild Steel: III Discussion of Results*, Proc Phys Soc B, **64** (1951) 747.

[211] N.J. Petch, *The cleavage strength of polycrystals*, J Iron Steel Inst, **174** (1953) 25.

[212] R. Armstrong, *The influence of polycrystal grain size on several mechanical properties of materials*, Metall Mater Trans B, **1** (1970) 1169.

[213] N. Hansen, *Hall–Petch relation and boundary strengthening*, Scripta Mater, **51** (2004) 801.

[214] N. Hansen, *The effect of grain size and strain on the tensile flow stress of aluminium at room temperature*, Acta Metall, **25** (1977) 863.

[215] M.F. Ashby, D.R.H. Jones, *Engineering Materials 1*, Elsevier Butterworth-Heinemann, 1996.

[216] F.R. Castro-Fernandez, C.M. Sellars, J.A. Whiteman, *Changes of flow stress and microstructure during hot deformation of Al-1Mg-1Mn*, Mater Sci Tech, **6** (1990) 453.

[217] S.V. Raj, G.M. Pharr, *A compilation and analysis of data for the stress dependence of the subgrain size*, Mater Sci Eng, **81** (1986) 217.

[218] F.R. Castro-Fernándeza, C.M. Sellarsb, *Relationship between room-temperature proof stress, dislocation density and subgrain size*, Philos Mag A, **60** (1989) 487.

[219] E.O. Hall, *Variation of Hardness of Metals with Grain Size*, Nature, **173** (1954) 948.

[220] U.F. Kocks, *Laws for Work-Hardening and Low-Temperature Creep*, J Eng Mater Tech, Trans ASME, **98** (1976) 76.

[221] H. Mecking, U.F. Kocks, *Kinetics of flow and strain-hardening*, Acta Metall, **29** (1981) 1865.

[222] L.E. Lindgren, K. Domkin, S. Hansson, *Dislocations, vacancies and solute diffusion in physical based plasticity model for AISI 316L*, Mech Mater, **40** (2008) 907.

[223] B. Babu, *Physically Based Model for Plasticity and Creep of Ti-6Al-4V*, Luleå University of Technology, Sweden, 2008.

[224] G.Z. Voyiadjis, F.H. Abed, *Effect of dislocation density evolution on the thermomechanical response of metals with different crystal structures at low and high strain rates and temperatures*, Arch Mech, **57** (2005) 299.

[225] J.J. Gracio, J.V. Fernandes, J.H. Schmitt, *Effect of grain size on substructural evolution and plastic behaviour of copper*, Mater Sci Eng A, **118** (1989) 97.

[226] S. Ales, W. Dan, L. Lars-Erik, *Simulation of metal cutting using a physically based plasticity model*, Modell Simul Mater Sci Eng, **18** (2010) 075005.

[227] Y. Bergström, *The plastic deformation of metals - a dislocation model and its applicability*, Rev Power Metall Phys Ceram, **2-3** (1983) 79.

[228] J.C. Simo, R.L. Taylor, *A return mapping algorithm for plane stress elastoplasticity*, Int J Numer Meth Eng, **22** (1986) 649.

[229] J.C. Simo, T.J.R. Hughes, *Computational Inelasticity*, Springer-Verlag, New York, 1997.

[230] T. Belytschko, W.K. Liu, B. Moran, *Nonlinear Finite Elements for Continua and Structures*, John Wiley & Sons, New York, 2000.

[231] M.F. Ashby, *The deformation of plastically non-homogeneous materials*, Philos Mag, **21** (1970) 399.

[232] N. Du, A.F. Bower, P.E. Krajewski, *Numerical simulations of void growth in aluminum alloy AA5083 during elevated temperature deformation*, Mater Sci Eng A, **527** (2010) 4837.

[233] X. Duan, T. Sheppard, *Influence of forming parameters on static recrystallization behaviour during hot rolling aluminium alloy 5083*, Modell Simul Mater Sci Eng, **10** (2002) 363.

[234] J.G. Kaufman, *Properties of Aluminum Alloys*, ASM International, Materials Park: Ohio, 1999.

[235] H.R. Glyde, *Relation of vacancy formation and migration energies to the Debye temperature in solids*, J Phys Chem Solids, **28** (1967) 2061.

[236] A.S. Nandedkar, *DIffusion characteristics of vacancies in aluminum interconnects*, Mater Res Soc P, **291** (1992) 361.

[237] T.S. Lundy, J.F. Murdock, *Diffusion of Al26 and Mn54 in Aluminum*, J Appl Phys, **33** (1962) 1671.

[238] B. Banerjee, A.S. Bhawalkar, *An extended mechanical threshold stress plasticity model: modeling 6061-T6 aluminum alloy*, J Mech Mater Struct, **3** (2008) 391.

[239] J.J. Burton, *Vacancy-Formation Entropy in Cubic Metals*, Phys Rev B, **5** (1972) 2948.

[240] R.W. Cahn, P. Haasen, *Physical Metallurgy*, North-Holland, Amsterdam, 1996.

[241] M. Kassner, M. Wang, M. Perez-Prado, S. Alhajeri, *Large-strain softening of aluminum in shear at elevated temperature*, Metall Mater Trans A, **33** (2002) 3145.

[242] J. Lin, F.P.E. Dunne, *Modelling grain growth evolution and necking in superplastic blow-forming*, Int J Mech Sci, **43** (2001) 595.

[243] X. Li, S. Soo, *Numerical Simulation and Superplastic Forming of Ti-6Al-4V Alloy for a Dental Prosthesis*, J Mater Eng Perform, **20** (2011) 341.

APPENDIX

Table A-1 Thickness measurement data for AA5083 after hot drawing at 400 ℃.

Location	Trial 1	Trial 2	Trial 3	Average	Standard deviation
#1	2.70	2.74	2.78	2.74	0.0400
#2	2.74	2.70	2.78	2.74	0.0400
#3	2.77	2.83	2.83	2.81	0.0346
#4	2.25	2.24	2.34	2.28	0.0551
#5	2.60	2.65	2.70	2.65	0.0500
#6	2.76	2.84	2.83	2.81	0.0436
#7	2.80	2.78	2.85	2.81	0.0361
#8	2.88	2.93	2.94	2.92	0.0321
#9	2.90	2.81	2.86	2.86	0.0451
#10	3.03	3.08	3.00	3.04	0.0404
#11	3.01	3.04	3.09	3.05	0.0404

Unit: mm

Table A-2 Thickness measurement data for AA5083 after gas forming at 400 ℃.

Location	Trial 1	Trial 2	Trial 3	Average	Standard deviation
#1	1.91	1.88	1.84	1.88	0.0351
#2	2.17	2.11	2.04	2.11	0.0651
#3	2.03	2.09	2.08	2.07	0.0321
#4	1.75	1.85	1.78	1.79	0.0513
#5	2.25	2.27	2.40	2.31	0.0814
#6	2.47	2.42	2.46	2.45	0.0265
#7	2.19	2.14	2.09	2.14	0.0500
#8	2.80	2.86	2.84	2.83	0.0306
#9	2.80	2.84	2.78	2.81	0.0306
#10	2.85	2.84	2.90	2.86	0.0321
#11	2.86	2.92	2.88	2.89	0.0306

Unit: mm

Table A-3 Thickness measurement data for Ti-6Al-4V after hot drawing at 800 ℃.

Location	Trial 1	Trial 2	Trial 3	Average	Standard deviation
#1	1.38	1.46	1.52	1.45	0.0702
#2	1.42	1.57	1.48	1.49	0.0755
#3	1.50	1.55	1.54	1.53	0.0265
#4	1.24	1.17	1.20	1.20	0.0351
#5	1.55	1.60	1.54	1.56	0.0321
#6	1.55	1.60	1.58	1.58	0.0252
#7	1.54	1.60	1.50	1.55	0.0503
#8	1.45	1.55	1.56	1.52	0.0608
#9	1.50	1.67	1.55	1.57	0.0874
#10	1.55	1.62	1.57	1.58	0.0361
#11	1.70	1.62	1.64	1.65	0.0416

Unit: mm

Table A-4 Thickness measurement data for Ti-6Al-4V after gas forming at 800 ℃.

Location	Trial 1	Trial 2	Trial 3	Average	Standard deviation
#1	1.12	1.27	1.15	1.18	0.0794
#2	1.24	1.34	1.22	1.27	0.0643
#3	1.29	1.33	1.21	1.28	0.0611
#4	0.76	0.79	0.65	0.73	0.0737
#5	1.27	1.32	1.28	1.29	0.0265
#6	1.35	1.45	1.38	1.39	0.0513
#7	1.40	1.46	1.39	1.42	0.0379
#8	1.48	1.50	1.5	1.49	0.0115
#9	1.5	1.57	1.51	1.53	0.0379
#10	1.56	1.58	1.60	1.58	0.0200
#11	1.61	1.62	1.63	1.62	0.0100

Unit: mm